Heavy Ions in the Solar Wind: Results from SOHO/CELIAS/MTOF

Peter Wurz
Physikalisches Institut, University of Bern
Sidlerstrasse 5, CH-3012 Bern, Switzerland

20 December, 2001

Paper submitted to Philosophisch-naturwissenschaftliche Fakultät, University of Bern, in partial fulfillment of the requirements for obtaining the “venia docendi”.

Contents

1 Introduction

To evaluate the history and the evolution of our planetary system, data on the composition of the planetary bodies and atmospheres, comets, and meteorites are crucial. For interpretation, these data need to be compared to a baseline composition. Since the Sun contains about 99.9% of the matter of the solar system, its surface composition closely reflects that of the protosolar nebula (with the notable exceptions He, D, Li, and Be).

The surface composition of the Sun is measured either by optical means or by measuring the composition of the plasma streaming away from the Sun, the solar wind. After more than three decades of experimental and theoretical research on the solar wind, there are still a number of fundamental questions unanswered:

- What produces the solar corona and how is it heated to temperatures 200–400 times higher than the underlying photosphere?
- Where in the corona do the different types of solar wind originate?
- How is the mass transported from the photosphere through the chromosphere into the corona?
- How is the composition of the plasma affected thereby?
- How are the particles in the corona, basically at rest, accelerated to form the supersonic, superalfvénic solar wind?
- What role do plasma turbulence and waves play in the corona with regard to solar wind formation?

To address these questions, it is necessary to collect of observational data on the solar wind elemental and isotopic abundances of as many elements as possible.

Matter in the solar corona and solar wind originates from the outer convective zone (OCZ) of the Sun. The abundances of some elements of the OCZ are well known from spectroscopic observations of the photosphere, and the abundances of non-volatile elements and their isotopes can be inferred with confidence from meteoritic data. The meteoritic abundance data are based on CI chondrites, which are believed to be the most “primitive” objects in the solar system [1]. Thus we have a set of solar abundances with which we can compare the abundances measured in the solar wind and in solar energetic particles (SEP). The most recent compilation of photospheric and meteoritic abundances was performed by Grevesse and Sauval [2] and is reproduced in Table 1-1. The abundances of elements in the photosphere of the Sun agree reasonably well in most cases with the meteoritic abundances. Table 1-1 lists the currently known elemental abundances for interstream and coronal-hole solar wind as compiled by von Steiger [3] and for the solar corona as derived from SEP events by Breneman and Stone [4]. SEPs are accelerated from the ambient corona and solar wind by a shock wave that is driven by a coronal mass ejection; thus they can be used to infer the coronal composition.

On its way from the photosphere into the corona and the solar wind, the solar material first encounters a temperature minimum of ≈4000 K, low enough for many elements to exist as neutral atoms. Later, in the chromospheric temperature plateau of $\approx 10^4$ K, these atoms are re-ionized, presumably by the solar extreme-ultra-violet (EUV) radiation from the corona. Atoms with a low first ionization potential (FIP) are ionized faster than atoms with a high FIP. According to the current understanding, low-FIP elements are fed preferentially into the corona, leading to an increased abundance (by a factor of about 4 compared to high-FIP elements) in the slow solar wind and the solar energetic particle population [3; 5]. While this preference for low-FIP elements in the composition of the solar wind is well established by observations, the underlying physical processes leading to this fractionation are still the subjects of current investigations. We will turn to this question in Chapter 2. In the lower corona the elements are further ionized to higher charge states by the hot electron gas at a temperature of about 1–2 MK. These ions are further accelerated to become part of the solar wind, which carries these particles out into the interplanetary space, where they can be analyzed *in situ*, for example, at 1 AU as in the case of the SOHO mission (the Solar and Heliospheric Observatory).

The data used in this study were measured with the Mass Time-of-Flight sensor (MTOF) of the Charge, Element, and Isotope Analysis System (CELIAS) instrument [6] on the SOHO spacecraft [7]. The MTOF sensor was designed to study the elemental and isotopic composition of the solar wind in a velocity range from about 300 to 800 km/s (this velocity range depends on the element considered). As Table 1-1 demonstrates, there are still quite a few elemental abundance determinations to be done, in particular for the solar wind but also for the SEPs. Results of measurements of the elemental and isotopic composition of the solar wind performed with the MTOF sensor will be reported later in this work. With MTOF we expect to

Table 1-1: List of elements in the mass range accessible to CELIAS/MTOF and their abundances in the respective solar wind regimes. Photospheric and meteoritic abundances are from a compilation by Grevesse and Sauval [2] and are given as $12+\log(n_X/n_H)$. Solar wind abundances are taken from von Steiger [3] and are given with reference to oxygen. The SEP-derived coronal abundances are taken from Breneman and Stone [4] and are given with reference to silicon. Values in parenthesis are highly uncertain.

Element	Photosphere	Meteorites	Solar Wind: Interstream	Solar Wind: Coronal-hole	SEP-derived Corona
H	≡ 12	–	1900±400	824±80	–
He	10.93±0.004	–	75±20 96±40	48.5±5	–
Li	1.10±0.1	3.31±0.04	–	–	–
Be	1.40±0.09	1.42±0.04	–	–	–
B	2.55±0.30	2.79±0.05	–	–	–
C	8.52±0.06	–	0.72±0.10	0.70±0.1	$2.35^{+0.25}_{-0.23}$
N	7.92±0.06	–	0.129±0.008	0.145±0.011	$0.700^{+0.052}_{-0.049}$
O	8.83±0.06	–	≡ 1	≡ 1	$5.68^{+0.36}_{-0.34}$
F	4.56±0.3	4.48±0.06	–	–	$(0.00028^{+0.00029}_{-0.00028})$
Ne	8.08±0.06	–	0.17±0.02 0.14±0.02 0.10±0.03	0.136±0.011 0.12±0.04	$0.783^{+0.084}_{-0.077}$
Na	6.33±0.03	6.32±0.02	–	–	$0.0670^{+0.0068}_{-0.0062}$
Mg	7.58±0.05	7.58±0.01	0.16±0.03	0.083±0.02	$1.089^{+0.064}_{-0.062}$
Al	6.47±0.07	6.49±0.01	–	–	$0.0837^{+0.0042}_{-0.0040}$
Si	7.55±0.05	7.56±0.01	0.19±0.04 0.18±0.02	0.054±0.009	≡ 1
P	5.45±0.04	5.56±0.06	–	–	$0.00489^{+0.00066}_{-0.00072}$
S	7.33±0.11	7.20±0.06	–	–	$0.242^{+0.010}_{-0.009}$
Cl	5.50±0.3	5.28±0.06	–	–	$0.00238^{+0.00084}_{-0.00080}$
Ar	6.40±0.06	–	0.004±0.001	–	$0.0241^{+0.0042}_{-0.0036}$
K	5.12±0.13	5.13±0.02	–	–	$0.0039^{+0.0021}_{-0.0016}$
Ca	6.36±0.02	6.35±0.01	–	–	$0.082^{+0.014}_{-0.012}$
Sc	3.17±0.1	3.10±0.01	–	–	$(0.00031^{+0.00055}_{-0.00031})$
Ti	5.02±0.06	4.94±0.02	–	–	$0.0049^{+0.0016}_{-0.0013}$
V	4.00±0.02	4.02±0.02	–	–	$(0.00048^{+0.00069}_{-0.00048})$
Cr	5.67±0.03	5.69±0.01	–	–	$0.0183^{+0.0039}_{-0.0033}$
Mn	5.39±0.03	5.53±0.01	–	–	$0.0068^{+0.0039}_{-0.0027}$
Fe	7.5±0.05	7.50±0.01	$0.19^{+0.10}_{-0.07}$ 0.12±0.03	0.057±0.007	$1.270^{+0.170}_{-0.150}$
Co	4.92±0.04	4.91±0.01	–	–	< 18.1
Ni	6.25±0.04	6.25±0.01	–	–	$0.0465^{+0.0081}_{-0.0074}$
Cu	4.21±0.04	4.29±0.04	–	–	$(0.00057^{+0.00087}_{-0.00057})$
Zn	4.60±0.08	4.67±0.04	–	–	$0.00161^{+0.00087}_{-0.00076}$

observe elemental abundances the in the solar wind similar to elemental abundances found in the photosphere and in meteoritic samples, with some modifications by physical processes in the Sun's atmosphere, for example, by the FIP fractionation. Therefore, it is also important to understand the FIP fractionation process well, in order to derive the photospheric abundance from solar wind measurements.

The primary data products obtained from the MTOF sensor are mass spectra. Figure 1-1 shows such a mass spectrum, which was compiled using data of 99 days during 1996, for one step of the 12-step MTOF stepping sequence. Most of the elements, almost all of which are listed in Table 1-1, and their more abundant isotopes can be identified in the MTOF mass spectra. Many of these elements and isotopes are resolved for the first time in the solar wind (compare with the earlier measurements given in Table 1-1). The detection limit of MTOF is around $A_{\text{det}} = 5.0$ (with $A = 12 + \log(n_X / n_H)$, the logarithmic measure of abundances). The detection limit is somewhat element dependent. For elements with photopsheric abundances exceeding this value we expect to be able to derive an abundance value in the solar wind from MTOF data. Elements heavier than Zn all have a photospheric abundance below 4.0, thus there is little hope that these elements will be measured with MTOF.

For the mass spectrum given in Figure 1-1, the vertical axis is in units of raw counts. It is an involved process to derive an absolute density for an element from the raw counts. Figure 1-1 might give the reader the impression that it is deceivingly simple to obtain elemental and isotopic abundances. However, the good mass resolution and high efficiency of the MTOF sensor come at the expense of a considerably more complicated sensor, and thus we have had to develop a more complicated instrument function compared to previous instrumentation for solar wind research. The entrance system efficiently suppresses the solar wind protons and to a large extent alpha particles. The heavy ions will pass through the entrance system more or less with an effective area of about 2 mm^2, with the term "heavy ions" referring to elements other than hydrogen and helium throughout this work. The total detection efficiency of the TOF sections is around a few times 10^{-3}. This allows for many heavy ions to have enough counts after five

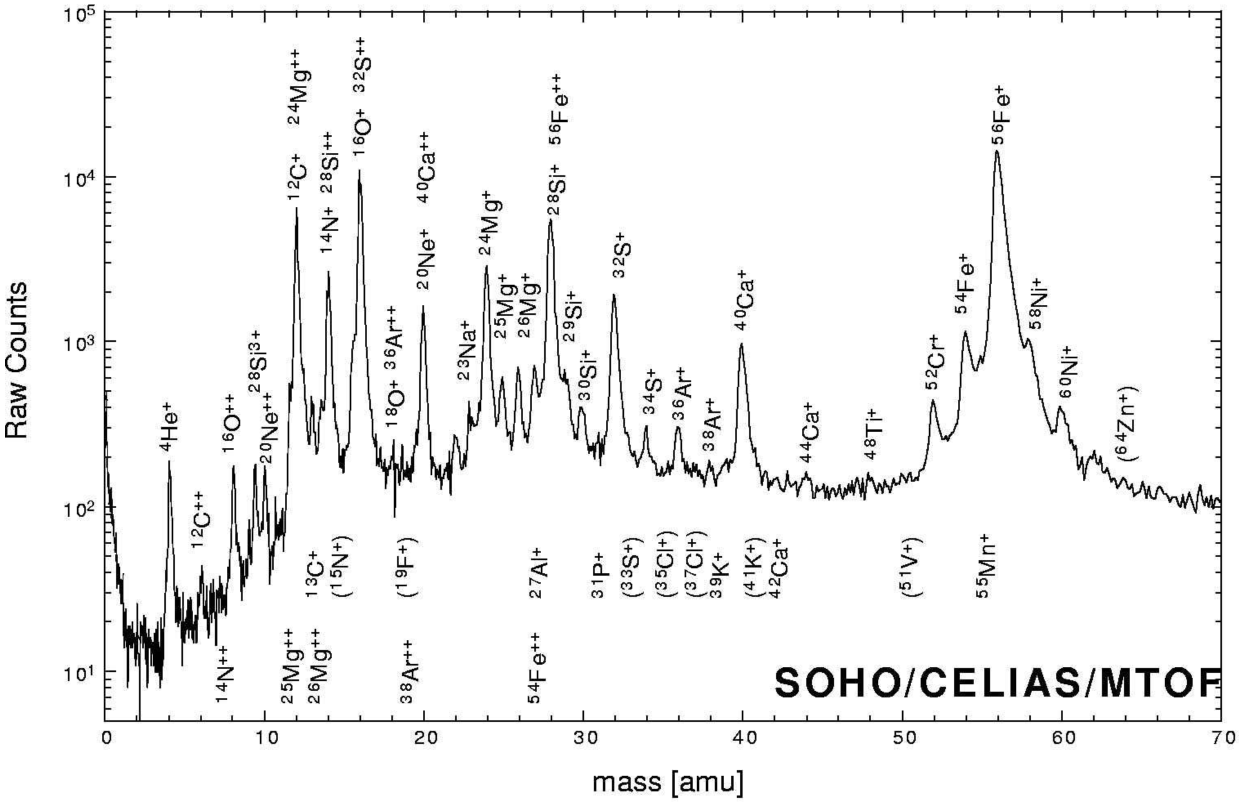

Figure 1-1: Mass spectrum recorded with the MTOF sensor of the CELIAS instrument on the SOHO mission. Displayed are raw counts for one step of the MTOF stepping sequence accumulated from DOY 144 to DOY 242 of 1996. Peaks in the spectrum are labeled by the two main ion contributors to that signal. The charge state given in the labels refers to the charge inside the MTOF sensor and not to the charge state of that ion in the solar wind. Labels in parenthesis indicate that the identification of that ion is highly uncertain.

minutes of accumulation time to obtain an elemental density. For the detailed response of the MTOF sensor for a particular element one needs to know the state of the solar wind, for example, the solar wind velocity, the kinetic temperature, the charge-state distribution, and a few other parameters. This information is given in the second part of this document.

This document is divided in two parts. The first part covers the scientific results obtained in this work (Chapters 2 to 4). In Chapter 2 we report on the abundances of the oxygen, silicon and iron ions in the solar wind, and what we can learn about the FIP effect using these data. In Chapter 3 we report on the elemental abundances of heavy ions before, during, and after the coronal mass ejection of January 6–10, 1997. With a theoretical model we try to explain the strong mass fractionation observed for this event. In Chapter 4 we report on the abundance of calcium in the solar wind. This is the first time the calcium abundance has been studied in detail in the solar wind, and we find that the calcium abundance shows a different behavior than one would expect from low-FIP elements.

The second part gives all the details of the MTOF sensor, the instrument function, and data analysis, with related discussions (Chapters 5 to 8). In Chapter 5 we present the theoretical background of the functioning of the isochronous mass spectrometer. In Chapter 6 we develop the instrument function in all detail, which is necessary since the sensor response of the isochronous mass spectrometer is much more complicated compared to previous instrumentation. In Chapter 7 we report on calibration data, and Chapter 8 gives the details of the data analysis. Chapters 2 to 4, reporting on the scientific results, include many cross-references to the instrumental part of the document, so that the reader can look up a particular instrumental detail without working through the whole document.

2 Oxygen, Silicon and Iron Abundances in the Solar Wind

2.1 Introduction

In the solar wind, elements with low first ionization potential (below about 10 eV) are systematically enriched relative to high-FIP elements with respect to their photospheric abundance. The enrichment amounts to a factor of three to five for slow solar wind, and about two for fast solar wind [3]. Slow solar wind has been associated with plasma originating from the streamer belt [8] and fast solar wind ($v > 500 km/s$) has been associated with plasma originating from coronal-holes [9]. It is generally believed that these relative enrichments are the result of a fractionation process taking place in the upper chromosphere and lower transition zone and are caused by a neutral-ion separation process [5]. In most models the ionization is assumed to be caused by the UV and EUV radiation from the solar corona. The neutral-ion separation process results from a competition between ionization and separation time scales. It was found that the fractionation pattern of the elements might be better described using the first ionization time as the organizing parameter instead of the FIP [10]. Several models have been designed to explain the FIP effect and have been reviewed by von Steiger [3] and more recently by Hénoux [11]. So far none of these models is able to self-consistently explain the FIP effect. Recently, the diffusion model put forward by Marsch and co-workers [12] was extended by Peter [13] by introducing a chromospheric mass flow velocity whose magnitude determines the strength of the FIP fractionation. We will compare our data with predictions derived from this model.

In this chapter we report on the investigation of the oxygen, silicon, and iron densities in the solar wind. Oxygen and silicon often serve as a reference for the less abundant heavy ions. Silicon and iron are low-FIP elements, and their abundance relative to oxygen—a high-FIP element—will allow us to draw conclusions on the FIP fractionation effect for different solar wind regimes.

The data were gathered with the MTOF sensor of the CELIAS instrument [6] on the SOHO mission. The principle of the MTOF sensor is described in detail in Chapter 5. The SOHO spacecraft is located at the Lagrangian point L1 and is a three-axis stabilized spacecraft pointing permanently at the Sun [7]. Because of these unique observation conditions and the large active areas of the individual sensors of the CELIAS instrument, measurements are performed with unprecedented time resolution and, at the same time, good counting statistics. The work presented in this chapter has been published as a shorter version earlier by Wurz *et al.* [14].

2.2 Data Analysis

The CELIAS data processing unit accumulates time-of-flight (TOF) spectra from the ions recorded with the MTOF sensor every five minutes, which then are transmitted to Earth. Mass peaks for the different elements were extracted from each of the transmitted TOF spectra by fitting the signal and the background with a least squares method (see Chapter 8). Subsequently, the overall efficiency of the MTOF sensor was calculated for each element and for each accumulation interval. To obtain particle fluxes for the chosen elements from the measured count rates, the MTOF sensor response comprising the transmission of the entrance system (see Chapter 6.1) and the response of the isochronous TOF mass spectrometer, V-MASS (see Chapter 6.3), were taken into account.

The settings for the MTOF sensor are cycled in a sequence of six steps, including two voltage settings for the entrance system and three values for the potential difference between the entrance system and the TOF mass spectrometer. Actually, the MTOF stepping sequence consists of 12 steps, but the same set of six steps is executed two times. The potential difference between the entrance system and the TOF mass spectrometer can be of negative, zero, or positive value, with the negative value accelerating the ions and the positive value decelerating the ions before they enter the TOF mass spectrometer. For the present analysis only the steps with negative and zero potential difference have been used, since the sensor response for the positive potential difference is not yet known within the required level of confidence. Furthermore, this step suffers from an elevated background level. Omitting one step out of six steps of the sequence from the data analysis does not create a bias in the data analysis, since the solar wind parameter space is still covered well by the remaining five steps (see Figure 6-14).

The actual solar wind plasma parameters, which were measured by the proton monitor (PM), a sub-sensor of the MTOF sensor, are needed as input parameters for the calculation of the MTOF sensor response. Ipavich *et al*. [15] found that the determination of the solar wind plasma parameters with the PM is quite accurate, which is better than required for the determination of densities of heavy ions with the MTOF sensor.

Another input parameter needed for the determination of the MTOF sensor response, and in particular for the determination of the active area of the entrance system, is the charge-state distribution of the solar wind ions for each element and for each accumulation interval. The MTOF sensor determines only the mass of the incoming ions. The charge information of the incoming ions is lost because the ions undergo an efficient charge-exchange process inside the sensor when they pass the carbon foil of the isochronous TOF mass spectrometer [16-19]. Therefore, we used the established anti-correlation between the solar wind velocity and the freeze-in temperature of the ions [20-22] to derive the so-called freeze-in temperature from the measured solar wind velocity. This procedure is detailed in Chapter 8.2.1, where the limitations of this approach (e.g., for CMEs) are also discussed. From the freeze-in temperature we obtained charge-state distributions for each element by assuming an ionization equilibrium in the corona and by applying ionization and recombination rates for collisions with electrons, as

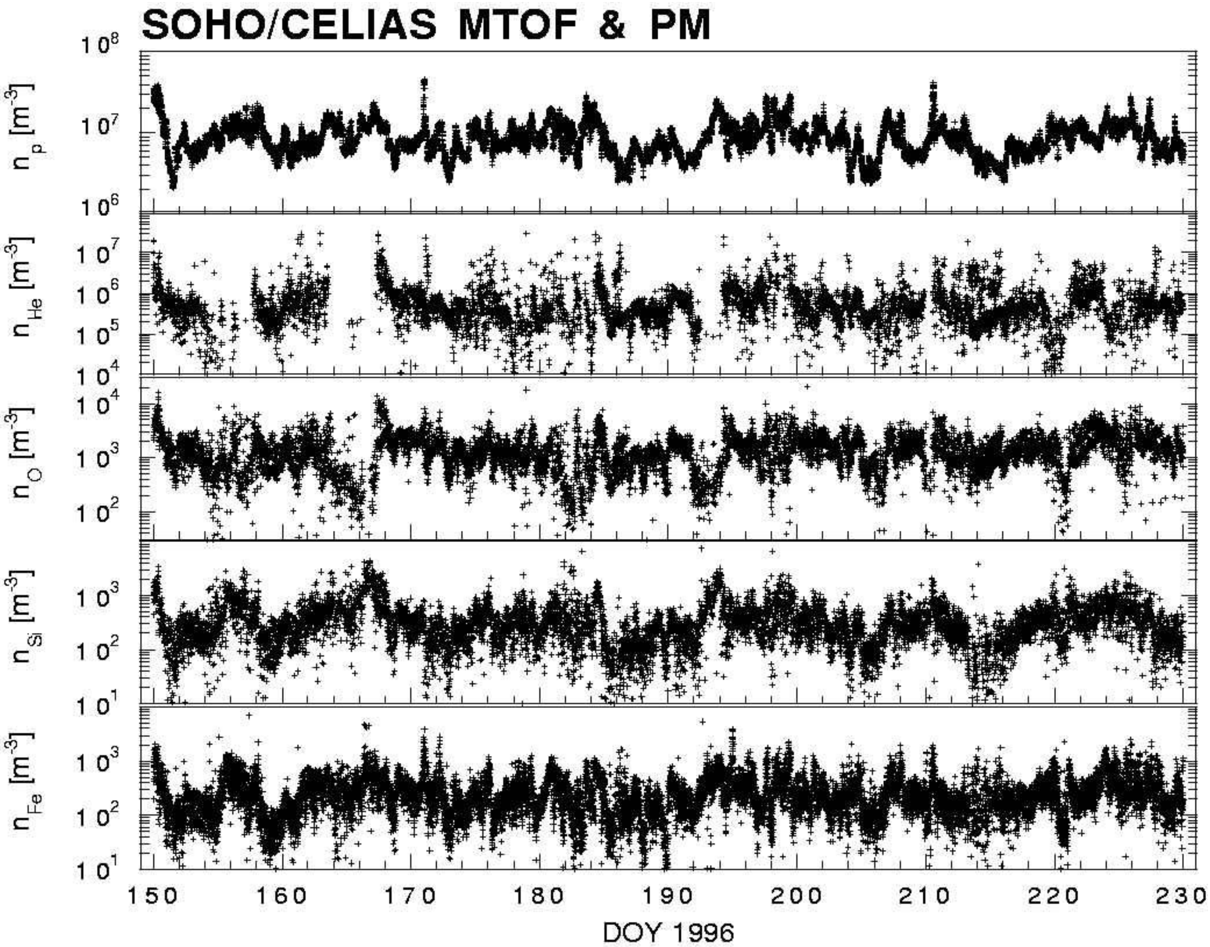

Figure 2-1: The data set derived from the MTOF and PM sensors used for this study. Data are shown with a time resolution of five minutes. No smoothing has been applied to the data.

given by Arnaud and co-workers [23; 24]. The application of the sensor response to the measured data yielded densities for the different elements.

2.3 Results

We evaluated the O, Si, and Fe densities with a time resolution of five minutes, the highest time resolution possible with the MTOF sensor, for the same time interval for which CTOF data are available (DOY 150–229 of 1996). One of the reasons for the choice of this time period is that testing of the MTOF instrument function was done against CTOF data (see Chapter 7.4). Another reason for this selection is that the Sun was going through solar minimum during that time. The selected data period is free of CMEs, flares, and other transient events, which quite often have a significantly different composition than the regular solar wind and therefore might interfere with the determination of composition of the regular solar wind.

The data used in this study are displayed in Figure 2-1, together with the proton density derived from measurements with the Proton Monitor (PM) [15]. Heavy ions (O, Si, and Fe) and the He density generally show a much larger variation in density than the protons. Typically the variability is larger by a factor of ten. This high variability is in good agreement with the high variability of helium with respect to protons in the solar wind as reviewed by Neugebauer [25]. She found that the ratio of protons to alpha particles (n_α / n_p) varies in the range from $8.1 \cdot 10^{-4}$ to $4.17 \cdot 10^{-1}$, a variation of a factor of 500. These short-term variations in the abundance are thought to be caused in the corona and are believed to be of temporal and spatial nature [26]. This high variability averages out when investigating longer time periods and causes hardly any systematic fractionation in the solar wind [26]. Of course, the heavy ion data are more noisy than the proton data because their densities, and consequently their count rates, are much lower, which results in a larger statistical variation. Under unfavorable solar wind flow conditions with respect to the actual MTOF sensor settings, the heavy ions fall below the detection limit of MTOF. The He densities are only shown in Figure 2-1 for completeness in this overview, but are not considered further in this work, because their density values have a large uncertainty. MTOF is designed and operated to suppress most of the incoming He^{++} ions and almost all protons, so that the MTOF sensor will not become saturated by their high fluxes in the solar wind. That is, He is typically suppressed by a factor of 1000 or more by suitable voltage settings of the entrance system. This suppression has to be considered for heavy ions of similar mass-per-charge ratio (*m/q*), for example, the ions O^{8+}, N^{7+}, Si^{12+}, and so on.

We observed strong short-term temporal variations in the density data for the heavy ions, significantly stronger than the temporal variations in the proton density data. These findings are in agreement with earlier results reported for iron densities by Aellig *et al.* [20]. From the derived density values we derived the abundance ratios Fe/O and Si/O, which we analyzed further. Also, the abundance ratios Fe/O and Si/O vary strongly on short time scales on the order of some ten minutes.

Figure 2-2 shows the distribution of Fe/O abundance ratios for the whole investigated time interval, organized by the solar wind velocity. Clearly, at least two regimes can be identified where the Fe/O abundance ratio is constant. For slow solar wind velocities below 380 km/s and for fast solar wind velocities in excess of 480 km/s there is a constant Fe/O abundance ratio. We associate these solar wind velocity regimes with solar wind originating from the streamer-belt regions and the coronal-hole regions on the Sun, respectively. In between these two regimes we observe a continuous transition from a high to a low Fe/O abundance ratio, which we will discuss later in this work.

The averaged Fe/O abundance ratios from our measurements for slow solar wind (< 380 km/s) and fast solar wind (> 480 km/s), together with published data for the Fe/O abundance ratio, are summarized in Table 2-1. We find reasonable agreement of our Fe/O abundance ratios with most of the published data, both for the interstream and coronal-hole types of solar wind flow. Only the Fe/O value derived from the measurement of the He/Fe ratio of Schmid *et al.* [27] and the He/O ratio by Bochsler *et al.* [28] is considerably higher than other published results and our value, but given the quoted uncertainty bar there is no serious discrepancy. Note

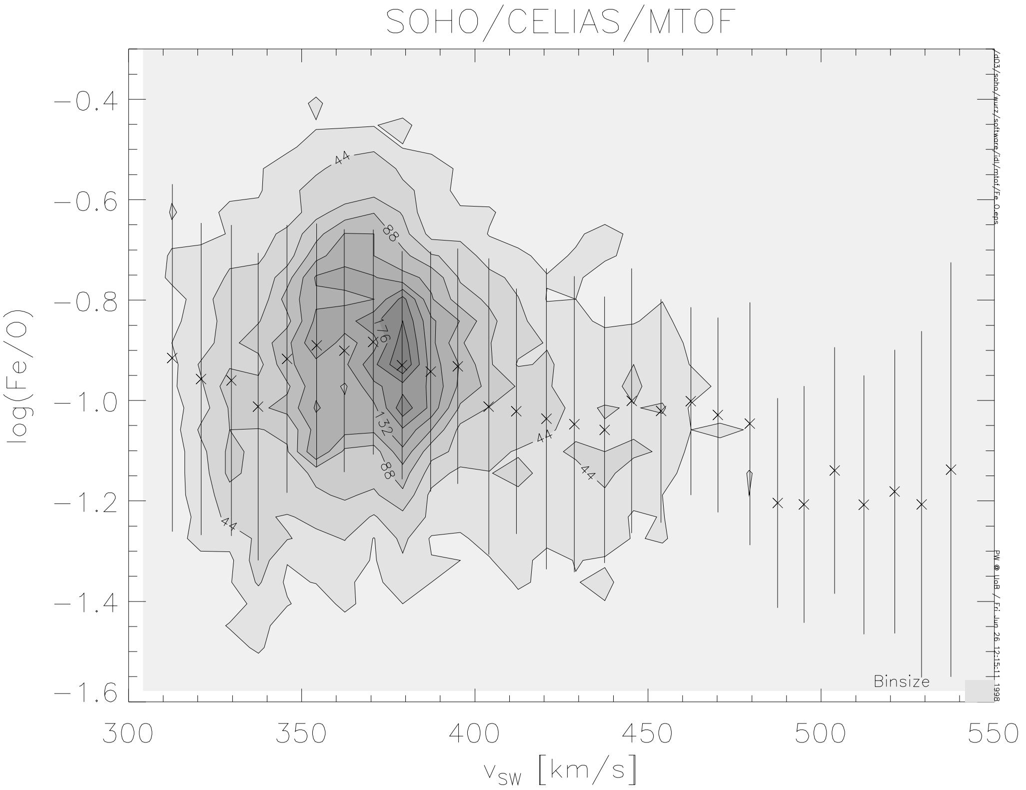

Figure 2-2: Logarithm of the Fe/O density ratio measured with CELIAS/MTOF versus the solar wind velocity. The 10 linearly spaced contour lines give the number of measurements for a particular bin. During that time period there was mostly slow solar wind, which explains the clustering of measurements between 350 and 400 km/s. The overlaid symbols are the means for a particular velocity bin and the error bars give the standard deviation of log(Fe/O) of the sample.

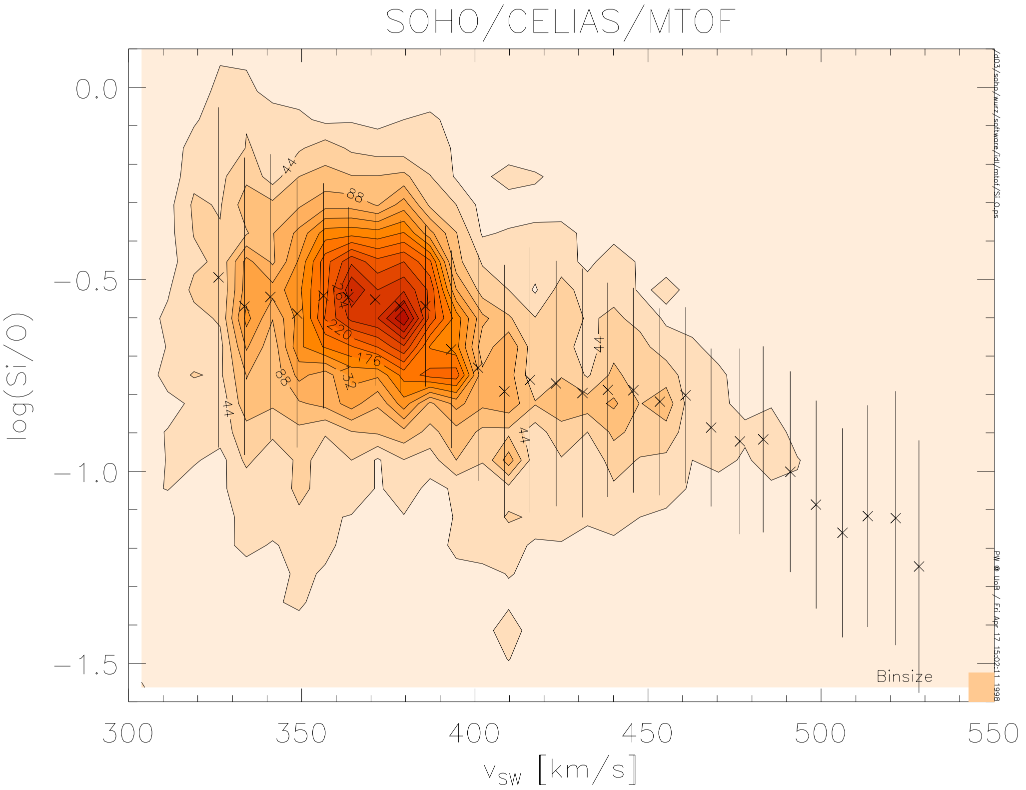

Figure 2-3: Logarithm of the Si/O density ratio measured with CELIAS/MTOF versus the solar wind velocity. The 10 linearly spaced contour lines give the number of measurements for a particular bin. During that time period there was mostly slow solar wind, which explains the clustering of measurements between 350 and 400 km/s. The overlaid symbols are the means for a particular velocity bin and the error bars give the standard deviation of log(Si/O) of the sample.

that the Fe/O ratio is a factor of two higher in the slow solar wind than in the fast solar wind. The Fe/O abundance ratio for the fast solar wind is higher than the photospheric Fe/O value, although this difference became smaller with the new value for the photospheric Fe/O abundance ratio reported recently by Aellig *et al.* [29].

In Figure 2-3 the distribution of the Si/O abundance ratios is shown for the whole time interval, organized by the solar wind velocity. As with the Fe/O abundance ratio, we can again identify two regimes where the Si/O abundance ratio is constant for an extended solar wind velocity interval, for slow solar wind velocities (< 380 km/s) and for fast solar wind velocities (> 480 km/s). These two regimes are again associated with solar wind originating from streamer belt regions and coronal-hole regions on the Sun, respectively. The averaged Si/O abundance ratios for these two flow types, together with published data for the Si/O abundance ratio, are summarized in Table 2-2. We find reasonable agreement of our Si/O abundance ratios with the published data, both for the interstream and coronal-hole types of solar wind flow. Note that the Si/O ratio is a factor of four higher in the slow solar wind than in the fast solar wind, which is a considerably larger variation than we observe for the Fe/O ratio between the two regimes. Furthermore, the Si/O abundance ratio for the fast solar wind has about the same value as in the photosphere, given the quoted uncertainties. Between these two regimes, where the Si/O abundance ratio is constant, we also observe a continuous transition.

Table 2-1: Summary of our value and reported values for the Fe/O abundance ratio in the solar wind (SW).

Measured regime	Fe/O ratio	Reference
Interstream SW	$0.19^{+0.1}_{-0.07}$	Bochsler *et al.* [28], Schmid *et al.* [27] [1)]
Interstream SW	0.12±0.03	Ipavich *et al.* [30]
Interstream SW	0.11±0.03	Aellig *et al.* [20] [2)]
Interstream SW	0.12±0.03	This work
Coronal-hole SW	0.057±0.007	Gloeckler *et al.* [31]
Coronal-hole SW	0.06±0.005	Geiss *et al.* [32]
Coronal-hole SW	0.06	Ipavich *et al.* [33]
Coronal-hole SW	0.063±0.007	This work
Photospheric value	0.0355±0.003	Anders and Grevesse [1], Hannaford *et al.* [34] [3)]
Photospheric value	0.0448±0.009	Aellig *et al.* [29]

[1)] This value is a combination of the He/O abundance ratio of 75 from Bochsler *et al.* [28] and the He/Fe ratio of 400 from Schmid *et al.* [27].

[2)] The value from Aellig *et al.* [20] is a weighted average over all solar wind conditions during the same three-month time period with mostly slow solar wind.

[3)] The photospheric value of the Fe/O ratio is derived from the iron abundance given by Hannaford *et al.* [34] and the oxygen abundance given by Anders and Grevesse [1].

Table 2-2: Summary of our value and reported values for the Si/O abundance ratio in the solar wind.

Measured regime	Si/O ratio	Reference
Interstream SW	0.19±0.04	Bochsler [35]
Interstream SW	0.18±0.02	Galvin *et al.* [36]
Interstream SW	0.20±0.03	This work
Coronal-hole SW	0.054±0.009	Gloeckler *et al.* [31]
Coronal-hole SW	0.052±0.007	This work
Photospheric value	0.0417±0.0051	Anders and Grevesse [1]

2.4 Discussion

The abundance ratios we find for Fe/O and Si/O are consistent with values reported in the literature (see Table 2-1 and Table 2-2) for interstream and coronal-hole type solar wind flow. Although the solar wind velocity rarely exceeded 500 km/s during the investigated time interval, we can associate this solar wind velocity regime with flow from coronal-holes, since the abundance ratio levels off at a low level consistent with abundance ratio values reported for fast solar wind flow of about 800 km/s, which clearly originated from coronal-holes [31; 32]. Whether we are observing flow from a polar coronal-hole extending towards the solar equator or flow from an equatorial coronal-hole cannot be decided on the basis of our data. Optical measurements from SOHO/EIT do not show any sign of a coronal-hole on the solar disc during this time period. There is also a correlation between the size of a coronal-hole and the maximum velocity observed for the associated solar wind, with the smaller coronal-holes having velocities of less than 500 km/s [9].

Recent optical measurements of elemental abundances in coronal streamers have been performed with SOHO/UVCS by Raymond *et al.* [37]. From these results a Fe/O abundance ratio of $0.13^{+0.05}_{-0.03}$ and a Si/O abundance ratio of $0.05^{+0.02}_{-0.01}$ are derived for the leg of an equatorial coronal streamer. The Fe/O value is commensurate with the established abundance ratio for slow solar wind (see Table 2-1), which is assumed to originate from that location. However, the Si/O value of Raymond *et al.* [37] is indicative of coronal-hole solar wind, which is incompatible with the investigated location. It is possible that the iron and silicon measurements were not done at the same location, and the silicon measurement reflects the abundance ratio in the core of that streamer. It has been found that the elemental abundances in the core of the streamer differ quite a bit from photospheric abundances [38]. If the slow solar wind, which is associated with coronal streamers [8], originates from the roots of the streamer along the open field lines at its periphery, then this makes for a small area to probe the source location of the slow solar wind by optical measurements and may explain the difference between the reported Fe/O and Si/O abundance ratios. In general, the authors observed a depletion of high-FIP elements rather than an enrichment of low-FIP elements at the leg and inside the coronal streamer.

Although silicon and iron are both low-FIP elements (the FIPs are $8.15\ \mathrm{eV}$ and $7.87\ \mathrm{eV}$, respectively), we observe some differences in the way their elemental abundance relative to oxygen changes for different solar wind regimes. Also, the ionization times τ for silicon and iron are close ($\tau_{Si} = 1.1 s$ and $\tau_{Fe} = 0.91 s$) and hardly can account for the different behavior.

Iron behaves like the “classical” low-FIP element. Its abundance ratio with respect to oxygen is enriched by a factor of about four for interstream solar wind and by a factor of about two for coronal-hole type solar wind compared to the photospheric values. Although we did not sample really fast solar wind with velocities around 800 km/s, associated with flow directly from polar coronal-holes, we can assume from the leveling off of the Fe/O ratio for solar wind velocities > 480 km/s at the value observed for polar coronal-holes [32] that there will not be any further decrease of the Fe/O abundance ratio for higher solar wind velocities than we observed.

For silicon, on the other hand, the FIP fractionation manifests itself somewhat differently from the “classical” FIP picture. For slow solar wind we again observe an enrichment in the Si/O ratio by about a factor of four compared to the photospheric ratio. However, for fast solar wind the enrichment in almost vanishes, i.e., we observe Si/O abundance ratios only marginally higher than the photospheric values in the fast solar wind.

Since we found a clear correlation between the solar wind bulk velocity at 1 AU and the elemental fractionation, we tried to compare our results with a recent FIP fractionation model by Peter [13], which is the only model using the chromospheric outflow velocities and densities as parameters for the FIP fractionation strength. In this model, which assumes full stationarity of the chromosphere, the FIP fractionation strength is predicted to vary with the chromospheric mass flow velocity U_H according to

$$f_{X/O} = \frac{1+\sqrt{1+4\left(w_X/U_H\right)^2}}{1+\sqrt{1+4\left(w_O/U_H\right)^2}} \qquad \text{Eq. 2-1}$$

where w_X are the ionization-diffusion velocities of the ions under consideration ($w_{Si} = 610 m/s$ and $w_{Fe} = 630 m/s$) and $w_O = 105 m/s$ is the ionization-diffusion velocity of oxygen, with the respective values adapted from Marsch *et al.* [12] for a density of $4 \cdot 10^{16}\ \mathrm{m}^{-3}$. For given conditions in the chromosphere we mapped the chromospheric mass flow velocity U_H to the solar wind bulk velocity v_{SW} (the proton velocity) measured at 1 AU with the PM to account for the observed fractionation factors. As we did in an earlier study [20], we used the relationship

$$\log v_{SW} = a + b \log U_H \qquad \text{Eq. 2-2}$$

and found that the fractionation we observed can be reproduced by the model by mapping the observed solar wind velocity to a chromospheric mass flow velocity. In Figure 2-4 and Figure 2-5 we show the comparison between the Si/O and Fe/O abundance ratio averages for solar wind velocity bins of the data presented above (in Figure 2-2 and Figure 2-3) together with the fractionation predicted by Eq. 2-1 for a density of $4 \cdot 10^{16}$ m^{-3} and a temperature of 10^4 K. These chromospheric parameters were chosen because they are considered typical for the layer in the chromosphere where the FIP fractionation process takes place [10; 12]. We used a velocity mapping with the parameters in Eq. 2-2 being $a = 2.71$ and $b = 0.114$ for the Si/O ratio and $a = 2.78$ and $b = 0.237$ for the Fe/O ratio. The difference in the parameter b reflects the observed difference in the fractionation for Si/O and Fe/O for fast solar wind. In Figure 2-2 and Figure 2-3 the chromospheric mass flow velocity is also indicated, which is necessary to obtain the elemental fractionation.

The range of abundance ratios we observe suggests a range of chromospheric mass flow velocities where FIP fractionation occurs. Apparently, the limits for the chromospheric mass flow velocities are given by the heights in the chromosphere where particles enter and exit the fractionation layer, that is the location where the density, temperature, and EUV flux (to name just the most important) are in the range necessary for the FIP fractionation for a particular element. Why the limits of the chromospheric mass flow velocities should be different for Fe/O and Si/O cannot be explained at present. The mapping of the chromospheric mass flow velocity to the solar wind velocity is a function of the assumed density. Using a lower density results in higher chromospheric mass flow velocities for the same fractionation.

It is generally believed that there is virtually no mass dependence in the FIP effect. The fractionation is mainly governed by the ionization time of the neutral species in the chromosphere and the related diffusion length for the neutrals of the heavy species with the dominant hydrogen atoms [10]. Marsch *et al.* [12] derived from their model the following asymptotic expression for slow solar wind (actually $U_H \to 0$) for the fractionation factor for two species, j and k as

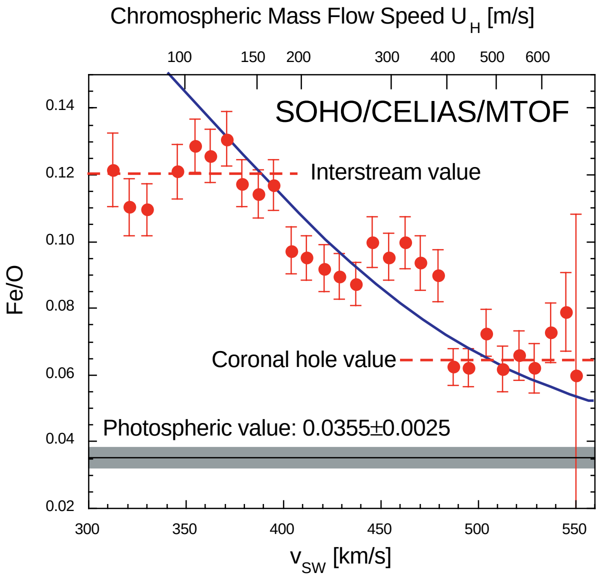

Figure 2-4: Average values of the Fe/O ratio for solar wind velocity bins of about 10 km/s. The error bars are 1 σ errors of the mean plus instrumental uncertainties. The dashed lines indicate the Fe/O ratio reached for slow and fast solar wind, respectively. The solid line is the result of Eq. 2-1 for a density of $4 \cdot 10^{16}$ m^{-3} and a temperature of 10^4 K, with the chromospheric mass flow velocity given on top of the figure.

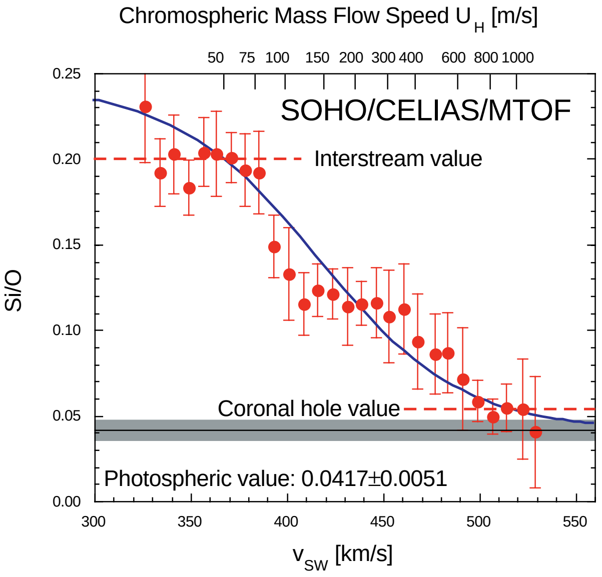

Figure 2-5: Average values of the Si/O ratio for solar wind velocity bins of about 10 km/s. The error bars are 1 σ errors of the mean plus instrumental uncertainties. The dashed lines indicate the Si/O ratio reached for slow and fast solar wind, respectively. The solid line is the result of Eq. 2-1 for a density of $4 \cdot 10^{16}$ m^{-3} and a temperature of 10^4 K, with the chromospheric mass flow velocity given on top of the figure.

$$f_{jk} = \frac{r_{kH}}{r_{jH}} \sqrt{\frac{\tau_k}{\tau_j}} \left(\frac{A_j + 1}{A_j} \cdot \frac{A_k}{A_k + 1} \right)^{1/4} \qquad \text{Eq. 2-3}$$

where f_{jk} is the predicted fractionation factor, r_{iH} is the collisional radius of species *i* with neutral hydrogen, τ_i is the first ionization time of species *i*, and A_i is the atomic mass of species *i*. The atomic mass only plays a role in the mobility of the species in a collision-dominated gas, and therefore appears only in the fourth root of the mass ratio, slightly favoring the lighter species. However, for transient particle ejection phenomena a mass dependence or a mass-per-charge dependence in the fractionation of the elements is often found, as has been observed recently for a CME (for example, see Chapter 3 and Wurz *et al.* [39]).

The stationarity assumed in the model by Peter [13] seems to be a simplification of the actual solar wind flow. As mentioned above, we observe strong short-term fluctuations in the density and the abundance ratio data, which appear to be in conflict with the assumption of stationarity. However, these short-term fluctuations average out over sufficiently long observational periods, and by organizing our abundance ratios by solar wind velocitys we can indeed compare our data with the model predictions.

2.5 The Iron Isotopic Composition in the Solar Wind

To correctly derive the elemental abundance for an element one not only has to evaluate the main isotope of an element but also needs to evaluate all its isotopes. It is not the scope of the present work to investigate the isotopic composition of elements in the solar wind. However, since the data were available from the study above it was worthwhile to check how a data analysis program (see Chapter 8) designed for the derivation of elemental abundances would perform when applied to the analysis of isotope ratios.

For this study we used a time series of ^{54}Fe and ^{56}Fe density data with a time resolution of five minutes. Data from the time period from DOY 150 to 229 of 1996 are used. For the derivation of an isotope ratio one usually collects many individual measurements to obtain mean values for the densities. From the time series of the ^{54}Fe and ^{56}Fe densities we get the average densities

$$\begin{aligned} n\left[{}^{54}Fe\right] &= 21.6 \pm 0.2 m^{-3} \\ n\left[{}^{56}Fe\right] &= 332.9 \pm 2.3 m^{-3} \end{aligned} \qquad \text{Eqs. 2-4}$$

in the solar wind velocity range from 300 km/s to 400 km/s. This is the range where the density remains constant on average. At higher solar wind velocity the average density drops, which might affect the value of the isotope ratio. The uncertainties given in Eq. 2-4 are the error of the mean. The standard deviation of the density is much larger, as has been reported above. No instrumental error has been included in Eq. 2-4. From these average iron densities for ^{54}Fe and ^{56}Fe we get the iron isotopic ratio

$$\frac{n\left[{}^{54}Fe\right]}{n\left[{}^{56}Fe\right]} = 0.0649 \pm 0.0007 \qquad \text{Eq. 2-5}$$

Again, no instrumental error has been included in the error given in Eq. 2-5. The uncertainty of the absolute calibration is expected to cancel out when an isotope ratio of an element is evaluated. However, the MTOF sensor response is not identical for isotopes of the same element, and one cannot expect that the entire isotopic instrument fractionation is corrected by applying the instrument function to the measured data. See Chapter 6.4.3 for an illustration of the isotopic fractionation of the instrument. Thus, an instrumental uncertainty has to be added, which considerably exceeds the statistical uncertainty with the present understanding of the instrument fractionation. We adopt a total uncertainty of the ^{54}Fe to ^{56}Fe isotope ratio of 0.003 in this preliminary analysis.

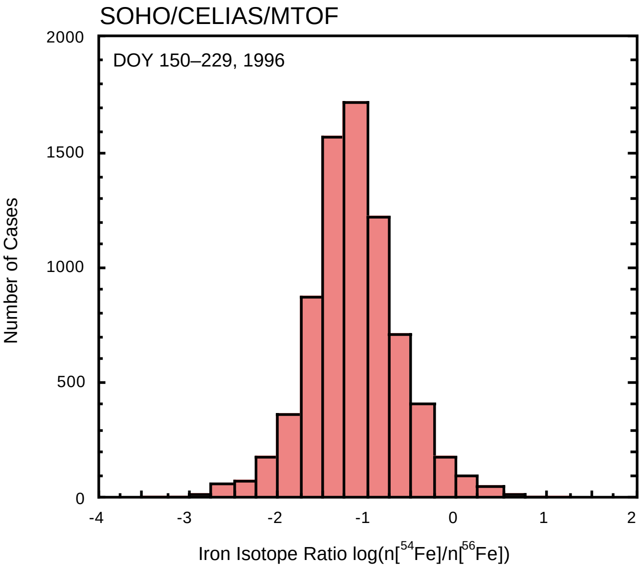

Figure 2-6: Histogram of ^{54}Fe/^{56}Fe isotope ratios for the time period from DOY 150 to 229 of year 1996. Measurements were selected for a solar wind velocity in the range from 300 km/s to 400 km/s.

Having a time series of ^{54}Fe and ^{56}Fe densities we can produce a time series of ^{54}Fe/^{56}Fe isotope ratios with the same temporal resolution of five minutes. A time series of isotope ratios has little value in itself because the scatter of individual measurements is large compared to the accuracy needed to make a meaningful statement on isotopic abundances. However, with this time series we avoid the problem that measurements with high densities dominate the derivation of the isotope ratio, as is the case with the above method. In the event that the isotope ratio is not constant with respect to different solar wind flow types (for example, fractionation processes in the convective zone or the solar atmosphere [21]), this dependence would be somewhat masked by the above analysis method. After all, the iron abundance does have a systematic dependence on the solar wind velocity. From this time series we derive a slightly higher value for the ^{54}Fe/^{56}Fe isotope ratio of 0.066±0.0006, with the error being again the error of the mean. A histogram of all the isotope ratios of this time series is shown in Figure 2-6, illustrating also the scatter of individual determinations.

A compilation of iron isotopic composition measurements is given in Table 2-3. Most of the published isotope ratios for the solar wind agree with the meteoritic value and the terrestrial value. Only the value of $0.085^{+0.005}_{-0.022}$ by Oetliker *et al.* [40] seems to be a little bit high. From studies such as the one of Anders and Grevesse [1] it is known that there is little variation among the abundances of the refractory elements in different materials of the solar system. Consequently, the agreement of solar wind iron isotopic ratios with the meteoritic value and the terrestrial value is no surprise. There are various places where isotopic fractionation can occur, as reviewed recently by Bochsler [21]. Isotopic fractionation can take place in the outer convective zone due to gravitational settling, in the upper chromosphere and lower transition region due to ion-neutral separation process, and in the inner corona due to inefficient coupling of the heavy ions to the protons and alpha particles. The isotopic composition can also be altered in the interplanetary medium by shock acceleration in transient particle events with extended shock fronts [43]. Apparently all these possible isotopic fractionation mechanisms have a minor effect on the iron isotopic composition, since we and others observe the same isotopic composition in different reservoirs of the solar system (see Table 2-3). The homogeneity in the elemental composition in the solar system (c.f. Anders and Grevesse [1] and also Table 1-1) indicates that the early condensates in the inner parts of the solar nebula have not

Table 2-3: Published values for the iron isotopic ratio of the solar wind, meteoritic samples, and terrestrial samples.

Measured regime	$n\left[{}^{54}Fe\right]/n\left[{}^{56}Fe\right]$	References
Solar Wind	$0.085^{+0.005}_{-0.022}$	Oetliker *et al.* [40]
Interstream SW	0.066±0.006	Ipavich *et al.* [41]
Coronal-hole SW	0.0595±0.006	Ipavich *et al.* [41]
CME	0.071±0.01	Ipavich *et al.* [41]
Interstream SW	0.065±0.003	This work
Terrestrial	0.0637±0.006 $^{1)}$	Audi and Wapsta [42]
Meteoritic	0.0632	Anders and Grevesse [1]

$^{1)}$ This isotopic ratio is derived from the ^{56}Fe abundance of 91.754(36)% and the ^{54}Fe abundance of 5.845(35)%. The uncertainty reflects the isotopic abundance variation of terrestrial samples [42].

undergone strong chemical fractionation, and therefore the isotopic fractionation also has to be very limited. For volatile elements, in addition, there is isotopic fractionation due to the evolution of the body in the solar system; for example, the isotopic composition for neon is significantly different in the solar wind than it is on the Earth [44; 45]. For a recent review on measurements of isotopic abundances in the solar wind see, for example, Wimmer *et al.* [46].

2.6 Conclusions

For interstream-type solar wind we found that the Fe/O and Si/O abundance ratios are enriched compared to their photospheric ratios by a factor of about four, which is a typical enrichment for low-FIP elements. In coronal-hole type solar wind a reduced FIP fractionation remains only for Fe but not for Si. Our findings are in good agreement with published results.

Furthermore, we can conclude from our measurements that there are not only two distinct modes of the solar wind—slow and fast solar wind—but there is also a continuous transition between these two extreme cases of solar wind flow. This continuous transition results from a varying FIP fractionation and cannot be explained by simple mixing of two types of solar wind. From a Monte-Carlo simulation it was concluded that in case of mixing, the transition would be much steeper than we measured[1]. This continuous transition is still seen when the Fe/O abundance ratios are plotted against the freeze-in temperature as has been reported before by Aellig *et al.* [29], which is considered by some to be a better organizing parameter than the solar wind velocity. In the event that CMEs, which are typically faster than the regular solar wind, are contained in the analyzed time interval the organization of abundance data with the freeze-in temperature is favorable. This is of no concern in this analysis due to the selection of a quiet Sun time period. These continuous transitions of the abundance ratios with solar wind velocities which we observed, and which have not been seen before, can be explained by the theoretical model of Peter [13] in which the chromospheric mass flow velocity determines the strength of the FIP fractionation process. By mapping the proton velocity we observed at 1 AU to the chromospheric mass flow velocity, we obtained reasonable agreement between the measured and predicted FIP fractionation. At present we cannot give a physical reason why the chromospheric mass flow velocity should be linked to the solar wind velocity. The differences we observe between the two low-FIP elements Si and Fe regarding their FIP fractionation cannot be explained either. This suggests that the processes involved in the FIP fractionation are more complex than are assumed in current models.

---

[1] M.R. Aellig, private communication (1998).

3 Elemental Composition of the January 6, 1997, CME Event

Using solar wind particle data from the CELIAS experiment on the SOHO mission, we studied the abundance of the elements O, Ne, Mg, Si, S, Ca, and Fe for the time period around the January 6, 1997, coronal mass ejection event (CME). In the interstream and coronal-hole regions before and after this event we found elemental abundances consistent with the expected abundance patterns of the respective flow regimes. However, during the passage of the CME and the passage of the erupted filament, which followed the CME, we found a mass-dependent element fractionation, with a monotonic increase toward heavier elements, which is markedly different from the composition in the interstream and coronal-hole regions before and after this event. We observed Si/O and Fe/O ratios on the order of one half during these time periods, which is significantly higher than for typical solar wind. We show that this elemental fractionation can be modeled by diffusion across magnetic field lines of coronal loops, the assumed precursor of the CME. Parts of the work reported in this chapter have already been published earlier by Wurz *et al.* [39; 47].

3.1 Introduction

In this chapter we present the analysis of the elemental composition of the coronal mass ejection (CME) which originated around 15:00 UT on January 6, 1997, on the solar surface and arrived at the SOHO spacecraft on January 10, 1997, at 04:11 UT. An overview of this event was given by Fox *et al.* [48] and covers the launch of the CME, its propagation through interplanetary space, and its effect on the Earth's atmosphere.

Approximately 30 minutes after the CME had reached the SOHO spacecraft, it arrived at the location of the WIND spacecraft (on January 10, 1997, at 4:48 UT). A review covering the present understanding of CMEs has been given recently by Gosling [49]. From the magnetic field measurements on WIND it has been concluded that this CME falls into the group of magnetic cloud events [50]. Their observational signature consists of an enhanced magnetic field strength, a smooth rotation of the magnetic field direction as the cloud traverses through interplanetary space and a low proton temperature. It has been found earlier that near 1 AU about one third of all CMEs in the ecliptic plane are magnetic cloud events [51].

The CME was slightly faster than the preceding solar wind and created a shock which was observed on SOHO on January 10, 1997, at 00:22 UT. The CME was followed by coronal-hole type solar wind, which arrived at the position of the SOHO spacecraft on January 11 at 06:56 UT. Just before the arrival of the coronal-hole a pronounced increase in the proton density was observed, which was attributed to an erupting filament (solar prominence material) on the solar surface [50]. Based on a complete set of solar wind plasma data (particles and magnetic field) available from the WIND spacecraft, the times and durations of the different phases of this event have been identified for the location of the WIND spacecraft [50]. With this information from the WIND spacecraft and with the plasma measurements from the SOHO/CELIAS proton monitor (PM) the times and durations of the different phases of this event at the location of the SOHO spacecraft have been established for the data analysis.

We measured the solar wind plasma parameters—namely the solar wind velocity, thermal velocity, proton density, and N/S solar wind flow angle—with the proton monitor (PM), which is part of the MTOF sensor of the CELIAS instrument. Using these solar wind plasma parameters, together with the particles and fields information from the WIND spacecraft, the times of the passages of the shock, the CME, the filament, and the coronal-hole-associated solar wind were identified. The measured solar wind plasma parameters are shown in Figure 3-1 for the investigated time interval around the CME event. Due to saturation of the PM, the proton density spike from the filament eruption could not be measured correctly. WIND/SWE results indicate that the proton density was about 185 cm^{-3} in the spike resulting from the filament eruption, a value which is about a factor of 20 above typical proton densities in slow solar wind and probably is the highest proton density ever observed.

The chosen time period offers a good opportunity to compare the elemental composition of the plasma during the CME passage with the two forms of *regular* solar wind composition, solar wind originating from the streamer belt (also called interstream or slow solar wind), which preceded the CME event, and with solar wind originating from a coronal-hole (also called fast solar wind) following the CME event. The measurements were taken with the MTOF sensor (Mass Time-of-Flight) of the CELIAS (Charge, Element, and Isotope Analysis System) instrument [6] on the SOHO spacecraft [7], which is located at the L1 libration point between Earth and Sun. The MTOF sensor is an isochronous time-of-flight (TOF) mass spectrometer utilizing the carbon foil technique, combined with an electrostatic entrance system. The entrance system allows ions to enter the sensor in a large energy range (only discriminating against protons, and partly against alpha particles) and through a wide angular acceptance cone. The MTOF sensor determines the mass of incoming ions with high resolution, sufficient to identify many isotopes and rare elements in the solar wind (see Figure 1-1 in Chapter 1).

3.2 Data Analysis

Data collected by the MTOF sensor of the CELIAS instrument on the SOHO spacecraft were used for this analysis. The CELIAS instrument and its sensors, among them the MTOF sensor and the PM, have been described in detail before [6]. From the ions recorded with the MTOF sensor, the CELIAS data processing unit accumulated time-of-flight (TOF) spectra for five minutes, which then were transmitted to ground. Mass peaks for the different elements were extracted from each of these TOF spectra. Subsequently, the overall efficiency of the MTOF sensor was calculated for each element and for each accumulation interval. To obtain densities of

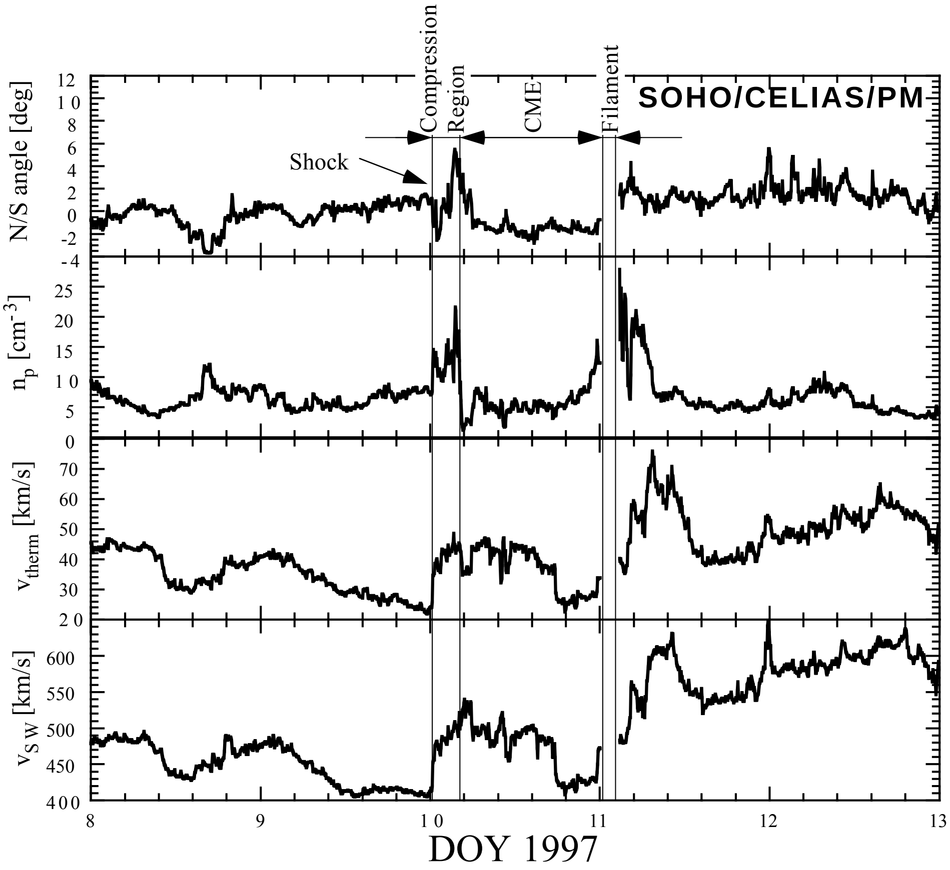

Figure 3-1: Solar wind plasma parameters as they are measured with the proton monitor, a sensor of the CELIAS instrument on SOHO, are shown for the time period of interest for this study.

the indicated elements, the instrument response of the MTOF sensor, which comprises the response of the entrance system (see Chapter 6.1) and the transmission of the isochronous TOF mass spectrometer (see Chapters 6.1 and 6.2), was taken into account in great detail. Furthermore, the instrument response was evaluated at the actual solar wind plasma parameters, which were measured by the PM (see Figure 3-1). By applying the instrument function to the measured data, absolute densities for the different elements were derived. See Chapter 6 for the details of the instrument functions and its limitations, and Chapter 7 for the comparison to calibration data. Although the determination of the solar wind plasma parameters from the PM is very accurate [15], this precision is actually more than needed for an accurate determination of absolute densities with the MTOF sensor.

Another input parameter needed for the determination of the MTOF sensor response, and in particular for the determination of the active area of the entrance system, is the charge-state distribution of the solar wind ions for each element and for each accumulation interval. The MTOF sensor determines only the mass of the incoming ion. The charge information of the incoming ions is lost because the ions undergo an efficient charge exchange process inside the sensor when they pass the carbon foil of the isochronous TOF mass spectrometer. Therefore, we used the established anti-correlation between the solar wind velocity and the freeze-in temperature of the ions [20-22] to derive the so-called freeze-in temperature from the measured solar wind velocity (see Chapter 8.2.1). From the freeze-in temperature we obtained charge-state distributions for each element by assuming an ionization equilibrium in the corona and by applying ionization and recombination rates for electronic collisions from Arnaud and coworkers [23; 24]. The application of the sensor response to the measured data yielded densities for the different elements.

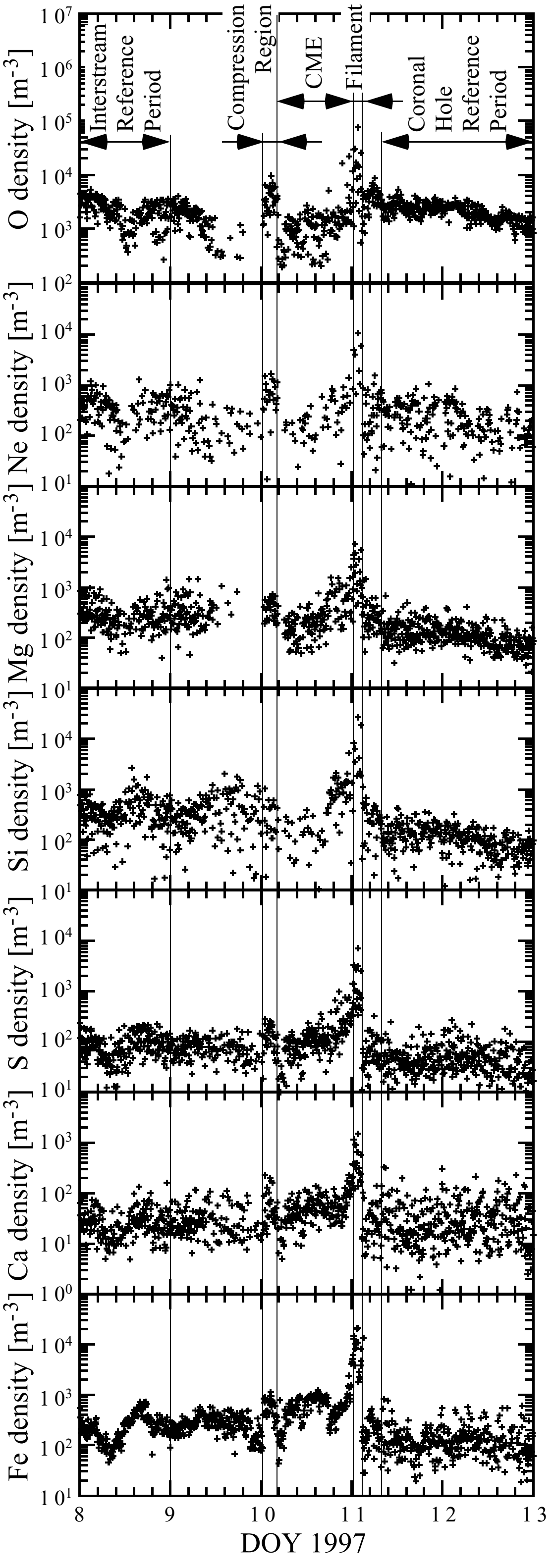

Figure 3-2: Densities for the different elements for the time period around the CME event. Each data point represents a measurement of 5 minutes. No smoothing of the data has been applied.

The MTOF instrument settings, which are cycled, have been optimized for a broad range of solar wind conditions. The stepping sequence includes two voltage settings for the entrance system and three values for the potential difference between the entrance system and the TOF mass spectrometer, V_F (negative, zero, and positive potential difference). For the present analysis only the steps with negative or zero potential difference have been used. In principle, a time resolution of five minutes can be obtained if the sensitivity of the MTOF sensor is high enough for the particular element considered. For typical solar wind conditions, it is indeed possible to derive densities with this high time resolution for the more abundant heavy elements in the solar wind, as will be shown later in this work.

3.3 Results and Discussion

Preliminary densities derived from the measured data for the elements O, Ne, Mg, Si, S, Ca, and Fe are shown in Figure 3-2 for the time period around the CME event. No smoothing of the data has been performed. What can be seen already from the data in Figure 3-2 without detailed analysis is that the compressed region after the shock (DOY 10, 1997, from 00:36 UT until 04:24 UT) had larger densities than the preceding interstream solar wind (with DOY denoting the day of year). This was also observed for the filament eruption (DOY 11, 1997, from 00:22 UT until 02:27 UT), for which a substantial increase in density was observed for that period. The time periods for the compression region after the shock, for the CME (DOY 10, 1997, from 04:24 UT until DOY 11, 00:22 UT), and for the filament are indicated by vertical bars in Figure 3-2. To derive a reference density for the interstream regime, the data accumulated during DOY 8 have been evaluated. For the reference density in the coronal-hole-associated solar wind data from the time period after the stream interface (DOY 11, 1997, 06:22 UT) until the end of DOY 12 have been evaluated. The stream interface was identified according to Burlaga [52] through a decrease in proton density by a factor of about two and an accompanying two-fold increase in kinetic temperature. For the two reference periods we find that the abundance ratios relative to oxygen agree with published data of interstream and coronal-hole type solar wind as reviewed by von Steiger *et al.* [53] and agree with the evaluation for a longer time period given in Chapter 2.

3.3.1 The Reference Solar Wind

Before we go into the details of the CME event itself, we will first discuss the unperturbed solar wind, in the interstream regime (the slow solar wind) and in the coronal-hole regime (the fast solar wind). The abundance of elements was highly variable over time during these two reference periods, which is quite common, as we discussed already in Chapter 2. Usually averages over long time periods have been performed to give reliable ratios of elemental abundances. Since we focused on the analysis of the CME event, we only used an integration period of about one day for the analysis of the unperturbed solar wind (the two reference periods). We found that the abundance ratios with respect to oxygen of elements with low first ionization potential (FIP), the FIP being less than about 10 eV (for example, the elements Mg, Si, Ca, and Fe in our study), were enhanced by a factor of about four in the interstream regime compared to the photospheric value. The enhancement amounted to less than a factor of two in the coronal-hole-associated solar wind for the low-FIP elements. For Ne, a high-FIP element, we found a small enrichment by a factor of 1.2 in the inter-

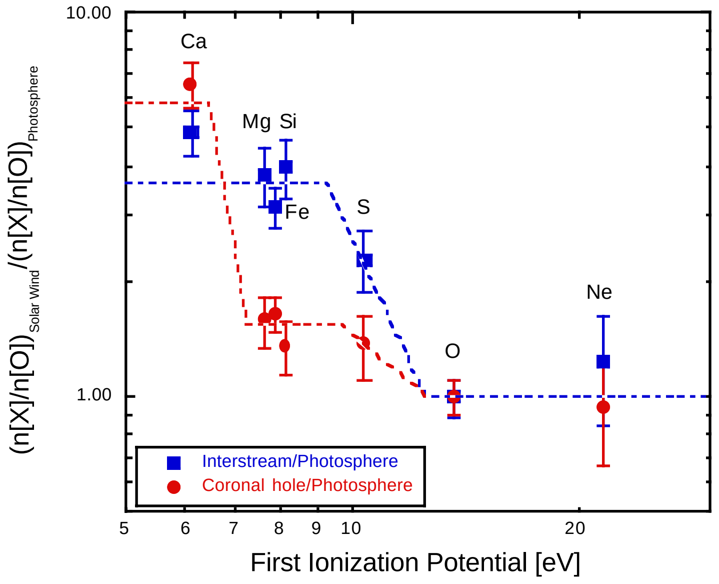

Figure 3-3: Solar wind abundance ratios for slow and fast solar wind (reference for interstream SW and reference for coronal-hole SW) relative to oxygen compared to photospheric ratios are plotted as a function of FIP. The photospheric abundances were taken from [2]. The dashed lines indicate the organization of the abundance ratios with respect to the FIP effect.

stream regime and we found photospheric abundances in the coronal-hole-associated solar wind. This organization of the abundance ratios of elements in the solar wind compared to their photospheric abundance ratios by their FIP is the well-known FIP effect [12; 54; 55]. However, the underlying physical processes causing the FIP effect are not yet fully understood, as has been reported in a recent review by von Steiger [3]. A plot of our data in the usual format regarding the FIP effect is displayed in Figure 3-3. The dashed lines in Figure 3-3 indicate the organization of the abundance ratios for the investigated elements with respect to the FIP effect. The abundance ratios of the elements fall approximately onto horizontal lines, with the level depending on whether they are low-FIP or high-FIP elements, and depending on the type of solar wind flow (interstream or coronal-hole). Only the abundance ratio of Ca does not fit in this simple picture, which is discussed below. Our abundance ratio data are commensurate with published data on elemental abundance ratios in the solar wind and with the results reported in Chapter 2, considering that only one day of data for the interstream and one day of data for the coronal-hole solar wind has been used for the analysis. The Si/O and Fe/O abundance ratios are a little bit lower than the values reported in Chapter 2, which indicates that one day of data is not enough to average out the short-time variability in the solar wind.

For Ca, not studied in detail in the regular solar wind before, we found an even larger enrichment in the interstream regime than for the other low-FIP elements during this time period. This agrees with the coronal abundance of Ca obtained from measurements of solar energetic particles (SEP) [56]. The enhancement of the Ca abundance ratio in the coronal-hole type solar wind is much larger than is expected for a low-FIP element. The Ca abundance ratio practically remained the same in the interstream and coronal-hole regimes, possibly it is even larger in the coronal-hole solar wind than in the interstream solar wind. Since Ca has such a low FIP it is already well ionized in the chromosphere. Thus the requirement that an element being neutral in the chromosphere for the FIP fractionation effect to occur is not fulfilled. The Ca abundance in the solar wind will be discussed in detail in the following chapter.

Due to the high efficiency and high mass resolution of MTOF and the favorable observation conditions on SOHO, we were also able to measure the sulfur density with much improved time resolution compared to earlier investigations. Until now there have been two reports for solar wind sulfur abundances, one by Shafer *et al.* [57] and one by Galvin [58]. In the framework of the FIP effect, sulfur is an interesting element, because its ionization potential is approximately where one expects the transition between low-FIP and high-FIP elements to be. We found that the sulfur-to-oxygen abundance ratio is increased in the slow solar wind by a factor of 2.3±0.4 compared to its photospheric abundance ratio, which compares reasonably well with 2.8±0.7, the value reported by Galvin [58] for this measurement. In the coronal-hole type solar wind we found that the sulfur-to-oxygen abundance ratio is increased by a factor of 1.4±0.3, which is almost the photospheric value. Thus sulfur is indeed in the transition between low and high FIP elements. For the S/Si abundance ratio we found values of 0.27±0.08 and 0.45±0.09 for the interstream and the coronal-hole-associated solar wind, respectively. Considering the reported uncertainties, this is in reasonably good agreement with the values 0.30±0.12 and 0.40±0.15, respectively, from the earlier study by Shafer *et al.* [57].

3.3.2 The Perturbed Solar Wind

The perturbed solar wind consists of the compression region after the shock, the actual CME (or magnetic cloud), and the filament. These three plasma populations have been analyzed separately and are discussed in detail below.

In the compression region after the shock and before the CME, the densities of all elements increased by a factor of about two compared to their reference densities in the interstream region. The proton density, measured independently by the PM, also went up by a factor of two during this time period. No mass dependence was found for the composition in the compression region. Similarly, the abundance ratios relative to oxygen clearly showed that the composition of the compression region resembled that of the preceding interstream solar wind regime, which is of course what one would expect for compressed solar wind following a shock.

For the CME we observed a markedly different elemental composition compared to the interstream solar wind [59]. Lower-mass elements—and especially oxygen—appeared to be depleted, whereas heavier elements were enriched compared to their interstream densities. Figure 3-4 shows the densities for the CME plasma compared to the reference density of the interstream regime. The oxygen density was only a factor of 0.66±0.13 of its interstream value, the magnesium density remained at its value of 1.0±0.2, and the iron density went up by a factor of 2.6±0.4. Note that we performed the comparison to the interstream reference densities, which already have a FIP bias compared to the photospheric abundances. No obvious correlation of the elemental abundances in the CME and the FIP was found (see Figure 3-5).

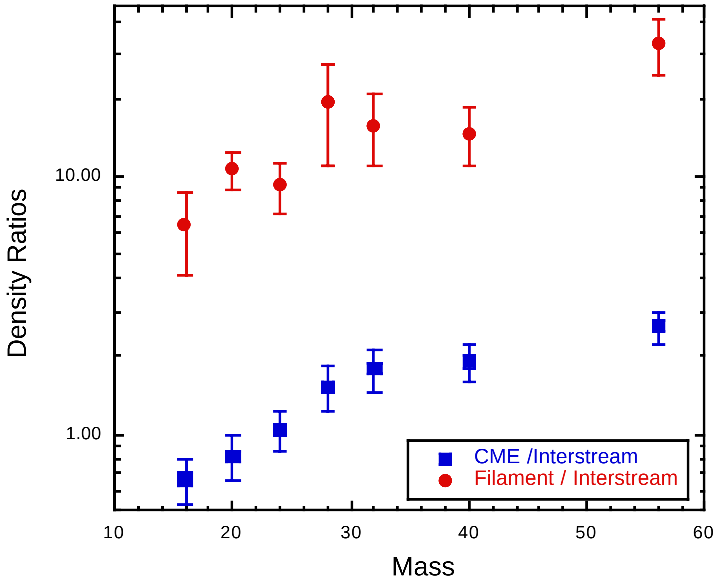

Figure 3-4: Densities ratios are given for the different elements evaluated for the CME and filament passage divided by their density in the interstream reference regime. Error bars are 1 σ wide and include statistical and instrumental errors.

Looking at the elemental abundances with respect to oxygen, we also found a clear correlation between the mass and the abundance ratio with respect to oxygen. For the Ne/O abundance ratio an enrichment of a factor of 1.2±0.2 compared to its interstream abundance was found. For higher masses, the enrichment then increased monotonically up to a factor of 4.0±0.6 for the Fe/O abundance ratio. For the CME plasma a Si/O abundance ratio of 0.43±0.14 and a Fe/O abundance ratio of 0.42±0.11 were found. No correlation was found between the abundance ratio with respect to oxygen and the first ionization potential (FIP) of the elements.

In the erupted filament the densities of all elements increased dramatically compared to their interstream values. A similar increase in density has also been observed for the protons [50]. Again we observed a clear mass dependence such as was found for the CME period (see Figure 3-4). Actually, the two measurements look very similar, with the enrichment during the passage of the erupted filament being about a factor of 10 higher than in the CME plasma. For the O density we observed an increase by a factor of 6.5±2.1 compared to its interstream reference density in the filament plasma. On the high-mass side we observed an increase by a factor of 19±8 and 33±7 for the Si and Fe densities, respectively, compared to their interstream reference densities. The mass dependence is also seen in the abundance ratio with respect to oxygen. For the filament plasma a Si/O ratio of 0.49±0.25 and a Fe/O ratio of 0.53±0.21 were found. Again, the in-

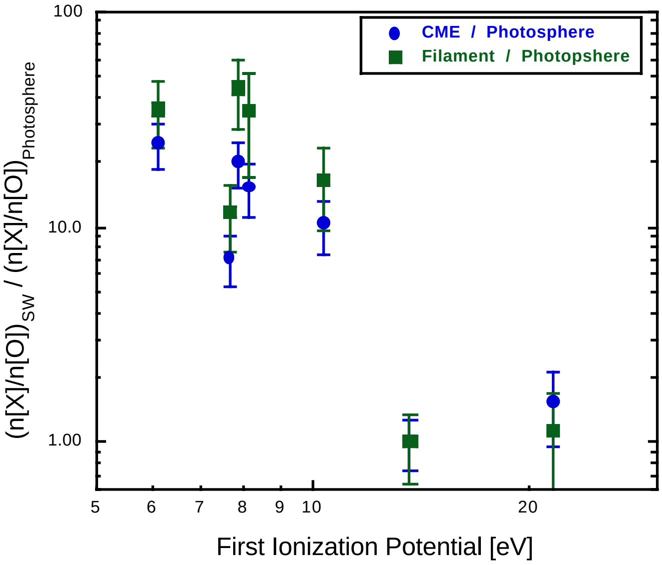

Figure 3-5: The abundance ratios for the CME and filament plasmas (relative to oxygen) compared to photospheric abundance ratios are plotted as a function of FIP. Data and error bars are the same as in Figure 3-4.

crease in density cannot be correlated with the FIP (see Figure 3-5).

One possible explanation of the unusual elemental composition we found for the CME and the filament plasma is that an isolated volume of material, the precursor of the CME and the erupting filament, resides on the solar surface where matter boils off from the volume. Given the gravitational field of the Sun, lighter elements would be lost more easily than heavier ones and a mass-dependent change of composition would result if the volume was reasonably isolated for a sufficiently long time on the solar surface. It has been observed frequently that CMEs begin as a slow swelling of a coronal streamer on time scales of several days [59]. Once this isolated volume is released into space in the form of a CME or an erupting filament, it will carry with it the altered compositional information as observed in our particle data at 1 AU. Another explanation for the unusual composition could be fractionation by selective acceleration after the release of the isolated volume. The mass-dependence we found for the elemental abundance during the CME and during the filament eruption could equally well be interpreted as a mass-per-charge dependence. Inferring the charge from the type of solar wind (since MTOF determines only the mass of ions)[2], we also obtained a monotonic function for the increase of the elemental abundance with mass-per-charge during these time periods. ^{3}He-rich flares, i.e., impulsive flares, usually also show enhancements of heavy elements, with Fe/O abundance ratios up to one [56; 60]. This enhancement is monotonic with mass, and is also called *mass bias*, and results from the ion acceleration process that depends on the mass-per-charge of an ion as well as its velocity. However, whether the low energies (typically 1 keV/nuc) of the particles we measured are sufficient to achieve the observed change in composition due to fractionation in the acceleration process remains to be demonstrated. Another concept, which could explain the observed mass fractionation, is diffusion across magnetic field lines. This is our favored concept to explain the measurements, and is discussed in detail below.

3.4 Disintegration of a Loop

The January 6, 1997, CME is associated with a large filament structure on the solar surface (S24° W10° [61]), since this filament is located where the projection of the CME trajectory maps back on to the solar surface. Moreover, there is no other feature visible on the solar disk, which could possibly be responsible for the CME release. After all, this CME event occurred around solar minimum. Neither flare activity [62] nor energetic particles [63; 64] have been observed in connection with this CME, making the CME an even more unusual event. The filament, with a length of about $1.5 \cdot 10^5$ km on the solar surface, went through considerable change during the days before the assumed release of the CME [61]. The filament existed several days after the CME left the solar surface, and was even the presumed starting location for a later CME on February 7, 1997 [61]. Thus we cannot directly link the disintegration of this filament with the observed CME, but possibly with the disintegration of parts of this filament structure. Careful inspection of the YOHKOH images of the zoo of loops of the filament structure revealed that a subset of these loops at the northwest end of the filament, a loop structure of about a quarter of the size of the filament, was missing after the release of the CME. There is no other feature in that area on the solar surface identified so far, which can be considered a candidate for a precursor to the CME. Thus, in the following we will base our interpretation of our observations on the disintegration of loops.

It is well established that CMEs arise preferentially from closed magnetic field regions in the solar atmosphere where the field normally was sufficiently strong to constrain the coronal plasma from expanding outward into the heliosphere [49]. Moreover, many of the ejections had the appearance of closed magnetic loops attached to the Sun at both ends [49]. So far, the fundamental question of what causes the eruption of a CME is unanswered. Extensive computer modeling efforts [65] as well as theoretical investigations [66] currently under way are aimed at understanding how a CME is actually released. Computer modelling shows that increased

---

[2] Preliminary analysis of WIND data indicated that the charge-state distribution for the minor ions in this CME is very similar to regular slow solar wind, unlike in many other CMEs (private information, Fred M. Ipavich, University of Maryland, 1997).

magnetic shear in the coronal loop will lead to instability, if a critical shear is exceeded, and eventual launch into interplanetary space [65]. In addition to this slow increase of magnetic energy in a loop due to the energy deposited by shearing, there exists also an alternative model of injected magnetic energy into an existing loop structure driving the structure out of equilibrium and leading to disintegration [66].

Our model of the CME event is as follows. A loop emerges from the solar surface and takes with it photospheric material. Due to the expansion of the cross section of a part of the loop with the height [66] a magnetic bottle is established between the two footpoints, which traps electrons and ions inside this structure. The confinement of plasma in a magnetic bottle is an imperfect process, because there is always a loss cone in velocity space from which ions can escape. Note that the loss cone is independent of the mass or charge of the particle [67]. The loop heats up and the hot electrons subsequently bring the trapped ions into higher ionization states corresponding to the temperature of the electrons in the loop. Many loops along the filament were observed with the YOHKOH SXT instrument, which mainly observes radiation from the electron plasma of 10 MK temperature. Thus one can safely assume the validity of the hot loop model [68], and electron temperatures similar to those of the solar corona. The foot-points of the loop move, and if this movement winds up the magnetic field lines of a loop enough, the loop will disintegrate and set free the trapped plasma material into an expansion into space. Let us assume that the disintegrated loop evolves to be the CME. This CME was observed first by SOHO/UVCS as a halo CME propagating toward the Earth, and was later detected *in situ* in the particle data with the SOHO/CELIAS instrument. Of course, a single loop will not release sufficient material to account for the mass of the CME as it was observed. It will take many loops to disintegrate at the same time to come up with the mass. From the sequence of images of the filament one can deduce quite some activity on this part of the solar surface. Since the filament could be observed on the solar surface for more than ten days before the release of the CME (the filament became visible on the east limb of the Sun on the morning of December 28, 1996), the loops will also have existed for the same time period. The plasma inside the loop is reasonably trapped by the magnetic bottle structure of the loop. However, we also have to consider diffusion across magnetic field lines, which results in a loss of ions from the loop. The diffusion across magnetic field lines is given by the corresponding diffusion coefficient

$$D_T = \frac{D_0}{1+\omega_c^2\tau^2} \qquad \text{Eq. 3-1}$$

With

$$\omega_c = \frac{q}{m} e B \qquad \text{Eq. 3-2}$$

the cyclotron frequency of an ion with a mass per charge ratio m/q in a magnetic field B. τ is the time between two collisions, and D_0 the diffusion coefficient parallel to the magnetic field. The time between two collisions is the inverse of the collision frequency for ion-ion collisions

$$\upsilon_{jk} = \frac{1}{\tau} = \frac{16}{3}\sqrt{\pi}\,\frac{\sqrt{\mu_{jk}}}{m_j}\left(\frac{Z_j Z_k e^2}{4\pi\varepsilon_0}\right)^2 \left(2\pi T_{jk}\right)^{-\frac{3}{2}} \ln\Lambda\, n_k \qquad \text{Eq. 3-3}$$

with Z_j and Z_k the charge of the ions *j* and *k* with the respective masses m_j and m_k. The main collision partners are assumed to be protons, thus $Z_k = 1$ and $m_k = m_p$. Furthermore,

$$\ln\Lambda = \ln\left(12\pi N \lambda_D^3\right)$$

is the Coulomb logarithm, with the Debye length being determined from the main plasma, the protons,

$$\lambda_D = \sqrt{\frac{\varepsilon_0 k_B T_p}{e^2 n_p}}$$

e is the elementary charge, k_B is the Boltzmann constant, and ε_0 is the dielectric constant.

$$\mu_{jk} = \frac{m_j\, m_k}{m_j + m_k} \qquad \text{Eq. 3-4}$$

is the reduced mass of the collision partners, and

$$T_{jk} = \mu_{jk}\left(\frac{T_j}{m_j} + \frac{T_k}{m_k}\right)$$

is the reduced temperature. The ion temperature is assumed to be 10^4 K for both collision partners, which is rather cold compared to the electron temperature in the loop. The ions will get heated later in the corona, starting at an altitude of around one solar radius above the solar surface [69], presumably by ion-cyclotron resonant Alfvén waves [70]. The diffusion coefficient for species i is

$$D_{0,i} = \frac{k_B T}{m_i\, \upsilon_{ij}}$$

Now we have all the ingredients to evaluate the diffusion across magnetic field lines (Eq. 3-1). In Figure 3-6 the results for the diffusion coefficient for diffusion across magnetic field lines are shown for the hot loop model, using parameters which have been reported to be typical for this scenario [68]. The assumed ion and proton temperatures are $T_i = T_p = 10^4 K$, the magnetic field strength is $B = 10^{-3}\,T$, the proton density is $n_p = 4 \cdot 10^{16} m^{-3}$, and the electron temperature is $T_e = 1.5 \cdot 10^6 K$ in this calculation. We find a considerable mass dependence in this diffusion coefficient, such that the lighter ions diffuse out of the loop more easily than the heavier ions. Thus, the plasma inside this loop is depleted of lighter ions. If the material contained in the loop eventually becomes the observed CME, the observed mass fractionation (compare with Figure 3-4) can be explained, at this point only qualitatively, by the different losses of the various heavy ions contained in the loop. Even the mass dependence of the diffusion coefficient we find, with a steeper reduction of D_T for the lighter ions and an almost constant diffusion coefficient for silicon and heavier ions, appears to be just the inverse of the observed fractionation. Assuming that diffusion across magnetic field lines is the relevant physical process to explain our observational data results in the fractionation being according to mass-per-charge rather than being a plain mass fractionation.

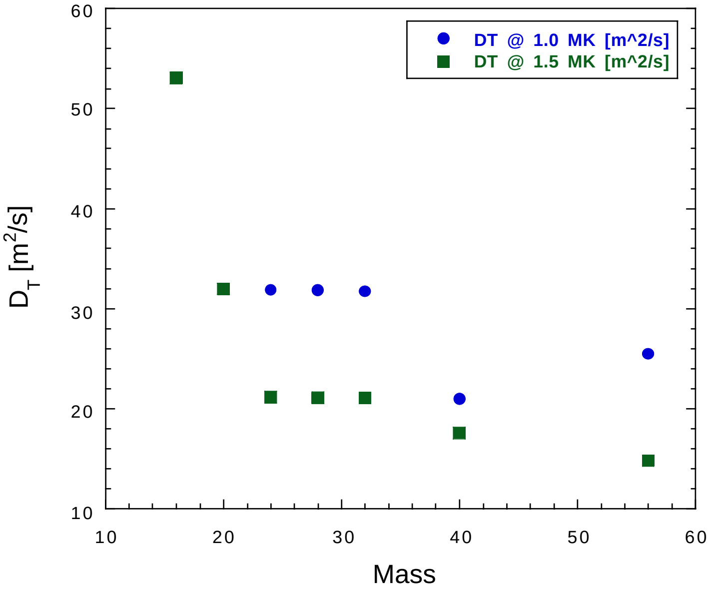

Figure 3-6: Diffusion coefficients for diffusion across magnetic field lines using the parameters (hot loop model): $T_i = T_p = 10^4 K$, $B = 0.001 T$, $N_p = 4 \cdot 10^{16} m^{-3}$, $T_e = 1.0 \cdot 10^6 K$ (circles) and $T_e = 1.5 \cdot 10^6 K$ (squares). For oxygen and neon the diffusion coefficients are the same for the two electron temperatures.

The various parameters can vary in a limited range to produce the mass-dependent D_T of this particular shape.

Going to lower magnetic field strengths ($B = 10^{-4} T$) maintains the distribution versus mass, and the diffusion coefficients increase in value. The difference in the diffusion coefficients for light and heavy ions increases as well. For higher magnetic fields the difference in the diffusion coefficient between the light and heavy ions becomes smaller until it vanishes around $B = 0.01T$, which is a factor of ten higher than is considered the field strength in a hot loop. The proton density cannot be much lower than the assumed value, otherwise the diffusion becomes very small and the pattern changes considerably for $n_p \leq 2 \cdot 10^{15} m^{-3}$. Higher proton densities $n_p \geq 10^{17} m^{-3}$ do not change the picture significantly. The dependence on the temperature of the ions is weak; in particular the temperature of the heavy ions is a very uncritical parameter. The electron temperature is also not critical, although it has to be above 1 MK to obtain the particular distribution of diffusion coefficients. We adopted a temperature of 1.5 MK for further calculations. However, we need hot loops to explain the measured data. For an electron temperature of 10^4 K, as would be the case in the cold loop model, the diffusion coefficients are about 280 m^2/s for every element. If we have the same diffusion coefficients for all elements we cannot explain the mass-dependent fractionation we observe.

An additional effect altering the composition of a flux tube may arise from the curvature and gradient of the magnetic field of a flux tube [71], which causes an average ion drift in the direction of the gradient and curvature of the magnetic field. This drift velocity is proportional to q^{-1} of the ion and thus favors the loss of lighter ions since their charge is smaller at the considered temperatures. For the geometry and the magnetic fields of typical flux tubes the associated drift velocities are very small (≈ 10^{-3} m/s) and the resulting fractionation is small as well.

Having found the diffusion coefficients we can pursue the model one step further by trying to derive a quantitative fractionation of the elements. We assume a loop of cylindrical cross section and calculate the loss of a specific element with time due to the diffusion across magnetic field lines. The loop geometry is defined as a tube of diameter $2a$ with a density of n_0 of a specific element inside the tube

$$n(r,0) = \begin{cases} n_0 & 0 \leq |r| < a \\ 0 & a \leq |r| \leq \infty \end{cases} \qquad \text{Eq. 3-5}$$

Outside the tube is vacuum

$$n(a,t) = 0 \qquad \text{Eq. 3-6}$$

Before we get started on the calculation we introduce the following variable transformation, which makes the calculations easier:

$$n_s(r,t) = n_0 - n(r,t) \qquad \text{Eq. 3-7}$$

changing the boundary conditions such that

$$n_s(r,0) = \begin{cases} 0 & 0 \leq |r| < a \\ n_0 & a \leq |r| \leq \infty \end{cases} \qquad \text{Eq. 3-8}$$

$$n_s(a,t) = n_0$$

For this problem we have to solve the diffusion equation

$$\frac{\partial n_s}{\partial t} = D_T \nabla^2 n_s$$

which is performed in cylindrical coordinates

$$\frac{\partial n_s}{\partial t} = D_T \frac{1}{r} \frac{\partial}{\partial r} \left(\frac{1}{r} \frac{\partial n_s}{\partial r} \right) = D_T \left(\frac{\partial^2 n_s}{\partial r^2} + \frac{1}{r} \frac{\partial n_s}{\partial r} \right)$$

and assumes only a radial dependence. No dependence along the loop or as a function of azimuth angle is considered. Thus we get

$$\frac{\partial^2 n_s}{\partial \xi^2} + \frac{1}{\xi}\frac{\partial n_s}{\partial \xi} - \frac{\partial n_s}{\partial t} = 0 \qquad \text{Eq. 3-9}$$

using the substitution $r = \xi\sqrt{D_T}$. Note that in Eq. 3-9 the elemental dependence is now contained in the variable ξ via the diffusion coefficient D_T. We apply the Laplace transform to solve Eq. 3-9

$$L\{f(t)\} = \int_0^\infty f(t)e^{-st}\,dt = \tilde{f}(s)$$

and get

$$\frac{\partial^2 \tilde{n}_s}{\partial x^2} + \frac{1}{x}\frac{\partial \tilde{n}_s}{\partial x} - \tilde{n}_s = 0 \qquad \text{Eq. 3-10}$$

using the substitution $x = \xi\sqrt{s}$. This equation is known as the modified Bessel differential equation and has the solution

$$\tilde{n}_s(\xi, x) = A(s)\,I_0(x) + B(s)\,K_0(x) \qquad \text{Eq. 3-11}$$

with I_0 being the modified Bessel function and K_0 being the modified Hankel function. The prefactor $B(s)$ is set to zero, since

$$\lim_{x\to 0} K_0(x) \approx \ln x$$

is divergent for $x \to 0$. The prefactor $A(s)$ is derived from the boundary condition Eq. 3-8

$$\tilde{n}_s(\xi_0, s) = \int_0^\infty n_s(\xi_0, t)e^{-st}\,dt = \int_0^\infty n_0\, e^{-st}\,dt = \frac{n_0}{s}$$

using the substitution $a = \xi_0\sqrt{D_T}$. Thus we obtain for the coefficient $A(s)$ in Eq. 3-11

$$A(s) = \frac{n_0}{s}\frac{1}{I_0\left(\sqrt{s}\,\xi_0\right)}$$

and the solution of Eq. 3-10 becomes

$$\tilde{n}_s(\xi, s) = \frac{n_0}{s}\frac{I_0\left(\sqrt{s}\,\xi\right)}{I_0\left(\sqrt{s}\,\xi_0\right)} = \frac{n_0}{s}\frac{J_0\left(i\sqrt{s}\,\xi\right)}{J_0\left(i\sqrt{s}\,\xi_0\right)} \qquad \text{Eq. 3-12}$$

with J_0 being the Bessel function and using

$$I_m(x) = i^m J_m(i\,x).$$

The solution in the time domain is obtained by inverse Laplace transformation of Eq. 3-12

$$n_s(r,t) = \frac{n_0}{2\pi i}\oint_C \frac{1}{s}\frac{J_0\left(i\sqrt{s}\,\xi\right)}{J_0\left(i\sqrt{s}\,\xi_0\right)}e^{st}\,ds \qquad \text{Eq. 3-13}$$

with the closed contour C of the contour integral given in Figure 3-7. The value of the contour integral in Eq. 3-13 is obtained by the residue theorem

$$\frac{1}{2\pi i}\oint_C f(\zeta)\,d\zeta = \sum_{k=1}^{n}\mathrm{Res}_f\left(z_k\right)$$

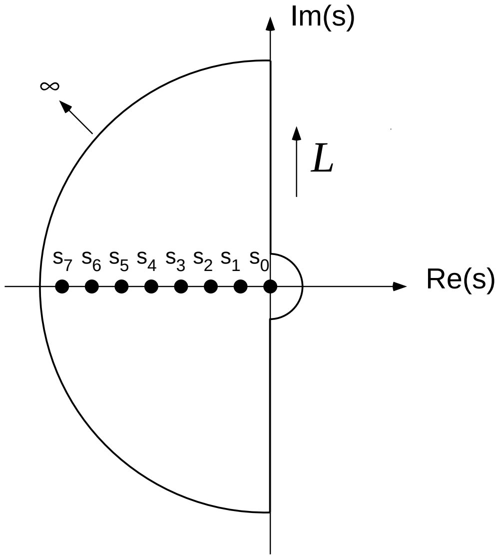

Figure 3-7: Contour path used for the integration in Eq. 3-13.

with the z_k's the points for which the function $f(\zeta)$ is singular. The power series representation of $J_0(z)$ has only even powers of z, so we do not need to worry about branch cuts. There is a singularity at $s=0$ in the argument of the integral of Eq. 3-13, which evaluates to $\mathrm{Res}_f(s=0)=1$. The other singularities occur at the points s_j where

$$J_0\left(i\sqrt{s_j}\,\xi_0\right)=0\,.$$

Since J_0 is analytic and the singularities are not at infinity we can write

$$\begin{aligned}\mathrm{Res}_f(\alpha_j) &= \frac{\frac{1}{s_j}J_0\left(i\sqrt{s_j}\,\xi\right)e^{s_j t}}{\frac{d}{ds}J_0\left(i\sqrt{s_j}\,\xi_0\right)} = \\ &= \frac{-\frac{\xi_0^2}{\alpha_j^2}J_0\left(\alpha_j\frac{\xi}{\xi_0}\right)e^{\frac{-\alpha_j^2}{\xi_0^2}t}}{\frac{\xi_0^2}{2\alpha_j}J_1\left(\alpha_j\right)}\end{aligned}$$

with α_j being the arguments for which the Bessel function is zero ($J_0(\alpha_j)=0$) and therefore $s_j=-\alpha_j^2/\xi_0^2$. Thus we obtain

$$n_s(r,t)=n_0\left(1-\sum_{j=1}^{\infty}\frac{2}{\alpha_j}e^{\frac{-\alpha_j^2}{a^2}D_T\,t}\,\frac{J_0\left(\alpha_j\frac{r}{a}\right)}{J_1\left(\alpha_j\right)}\right)$$

and finally, by undoing the substitution of Eq. 3-7 we get

$$n(r,t)=n_0\sum_{j=1}^{\infty}\frac{2}{\alpha_j}e^{\frac{-\alpha_j^2}{a^2}D_T\,t}\,\frac{J_0\left(\alpha_j\frac{r}{a}\right)}{J_1\left(\alpha_j\right)} \qquad \text{Eq. 3-14}$$

which is an exact solution of our problem and a convergent sum. Typically, we are interested in long time periods, so we only need to consider a few terms of the sum in Eq. 3-14, because of the exponential term. To compare the calculations with the measurements presented above (in Figure 3-4) we need to integrate Eq. 3-14 over the entire flux tube

$$N(t)=2\pi\int_0^a n(r,t)\,r\,dr=2\pi n_0\sum_{j=1}^{\infty}\frac{2}{\alpha_j}e^{\frac{-\alpha_j^2}{a^2}D_T\,t}\,\frac{1}{J_1\left(\alpha_j\right)}\int_0^a J_0\left(\alpha_j\frac{r}{a}\right)r\,dr$$

which resolves to

$$N(t)=n_0\sum_{j=1}^{\infty}\frac{4\pi a^2}{\alpha_j^2}e^{\frac{-\alpha_j^2}{a^2}D_T\,t} \qquad \text{Eq. 3-15}$$

Using the initial number of ions $N_0 = \pi a^2 n_0$ we can write Eq. 3-15 as

$$N(t) = N_0 \sum_{j=1}^{\infty} \frac{4}{\alpha_j^2} e^{\frac{-\alpha_j^2}{a^2} D_T t} \qquad \text{Eq. 3-16}$$

Now we can evaluate Eq. 3-16 for the different ions using the diffusion coefficients we derived earlier (see Figure 3-6). For this evaluation we will consider $N(t)/N_0$ for each element; that is, we simply investigate the depletion each ion species suffers due to diffusion perpendicular to the magnetic field lines as a function of time. This makes us independent of any assumptions on the initial abundance of the elements (for example, the photospheric abundance). By multiplying $N(t)/N_0$ with an initial density for an element we will get the final abundances of elements at the time of the release of the CME. However, coming up with an initial abundance is an involved endeavor and is not necessary here to explain the observed mass fractionation. Also, we can assume that these initial elemental abundances are modified by the FIP effect given the closeness of this region to the solar equator.

The comparison of the measured elemental fractionation in the CME and in the filament with the fractionation due to diffusion across magnetic field lines is shown in two separate panels in Figure 3-8 for flux tubes of 10^4 m radius. The crosses with the error bars are the measured data from Figure 3-5 (the pertaining *y*-axis is on the left side of the panels). The results from the model calculation are indicated by the circles (the pertaining *y*-axis is on the right side of the panels). The left and right *y*-axes are chosen such that they span the same relative range between minimum and maximum value, a factor of 6 for the CME (left panel), and a factor of 7 for the filament (right panel). The time necessary for the fractionation has been chosen to reproduce the measured data with the model data, via visual comparison. The fractionation data shown in Figure 3-8 are obtained after a time of about 7 days for which the loop system must have existed and the diffusion changed the elemental abundance—a time which compares well with the time the loop system was observed on the solar disk. The long time needed to come up with the elemental fractionation appears to be particular to this CME event, and could also be the reason why for most of the observed CMEs such a strong elemental fractionation has not been observed.

If one wants to push the idea of disintegrating loops as the initial step of a CME release further one could possibly explain the variety in the composition observed in CMEs. Given the variety of loops, in terms of temperature, size, and many other parameters [68], and the temporal development of the elemental abundance, or the development of the charge

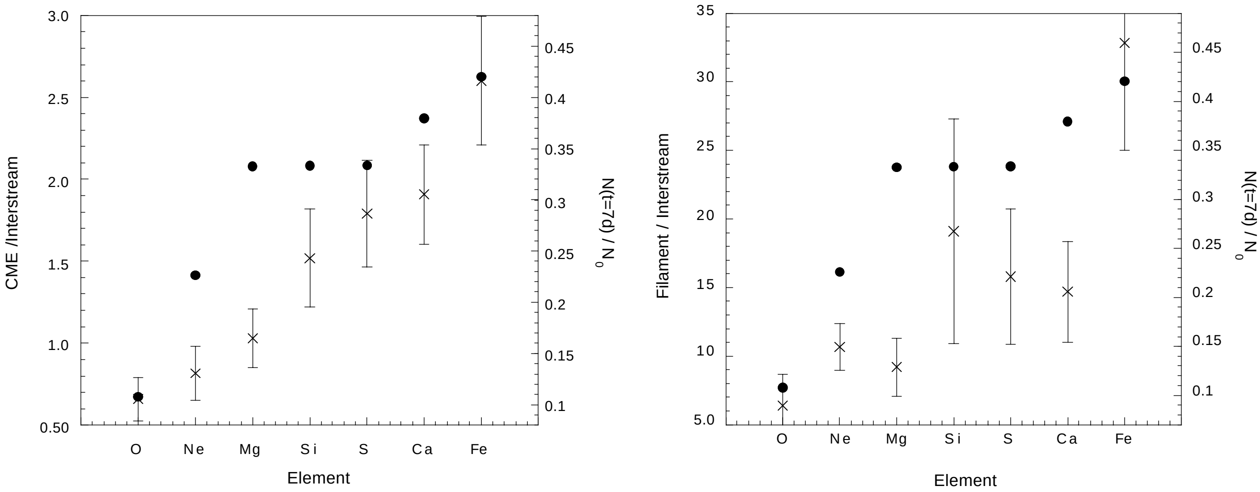

Figure 3-8: Comparison of the observed elemental fractionation in the CME (left panel) and the filament (right panel) with respect to the interstream elemental abundances before the event, with the result from the calculation of the depletion of elements due to diffusion across magnetic field lines. For the model calculation a time of 7 days has been used. For the measured data the *y*-axis is always on the left (crosses with error bars) and for the calculated data the *y*-axis is on the right (circles). The range of the left and right *y*-axes for each plot is set such that they span the same factor between minimum and maximum.

distribution, one can easily explain many observations of CMEs by finding the proper initial conditions in a loop system on the solar surface, which will eventually evolve in the CME to the final observed plasma composition.

In the above calculation we used only one electron temperature for all elements to derive the ionization state of an element. It is known that the charge-state distribution for different elements is governed by different electron temperatures, or rather the balance between ionization and recombination for a particular charge state of an element is reached at different electron temperatures (see, for example, [3; 32], and Chapter 8.2.1). Also, non-Maxwellian tails in the electron distribution will affect the ionization balance [72]. Furthermore, only one charge state for each element, the most abundant charge state of the distribution, has been considered in the calculation. In conclusion, the model presented above could be improved by elaborating on these details, and it is anticipated that the improved model will reproduce the observed elemental fractionation even better. However, already at this stage, the model can explain the mass-dependent fractionation, with a monotonic increase toward heavier elements. Furthermore, the model can also explain the magnitude of the fractionation, with the Si/O and Fe/O abundance ratios being about a factor of four higher than observed in regular solar wind.

4 Calcium in the Solar Wind

Calcium is an interesting element for at least two reasons. First, Ca is a very low-FIP element with a first ionization potential (FIP) of 6.11 eV, which is considerably lower than the FIP of the commonly studied low-FIP elements Mg, Si, and Fe in the solar wind (for example, see Chapter 2). A preliminary analysis performed in conjunction with the analysis of the CME of January 6, 1997, showed that Ca might have an anomalous behavior with regard to the FIP fractionation, such that its abundance remains about the same for slow and fast solar wind (see Chapter 3). This is in contrast to other low-FIP elements for which the density is markedly different in the slow and in the fast solar wind (see Chapters 2 and 3). Such a behavior is usually only observed for the high-FIP elements; however, their densities are not enriched with respect to oxygen.

Second, Ca ions in the regular solar wind cannot be measured by SWICS-type instruments, for example, linear TOF sensors, since their small signal is masked by the more abundant silicon and iron ions in the M–M/Q matrix. Since CTOF is also a linear TOF sensor we don’t anticipate being able to derive Ca abundances from CTOF data. So far the Ca abundance has been determined mostly from SEPs for the SEP-derived corona, for example, by Breneman and Stone [4]. Besides our earlier work in connection with the January 6, 1997, CME [47], there is one other study of the calcium abundance by Kern *et al.* [73] for slow solar wind in a limited velocity range. Thus measuring the Ca abundance directly in the solar wind for a large solar wind velocity range will add to the general understanding of heavy ions in the solar wind.

Data extraction of Ca peaks from MTOF spectra is rather straightforward and is performed in the same way as was discussed above. The Ca peak is not contaminated by a doubly charged ion of higher mass, nor does the Ca signal suffer from being situated on the shoulder of a peak of an abundant element. Also, the instrument function is reasonably good-natured (as it is for Fe) compared to lower mass elements. The ionization state of Ca in the solar wind is

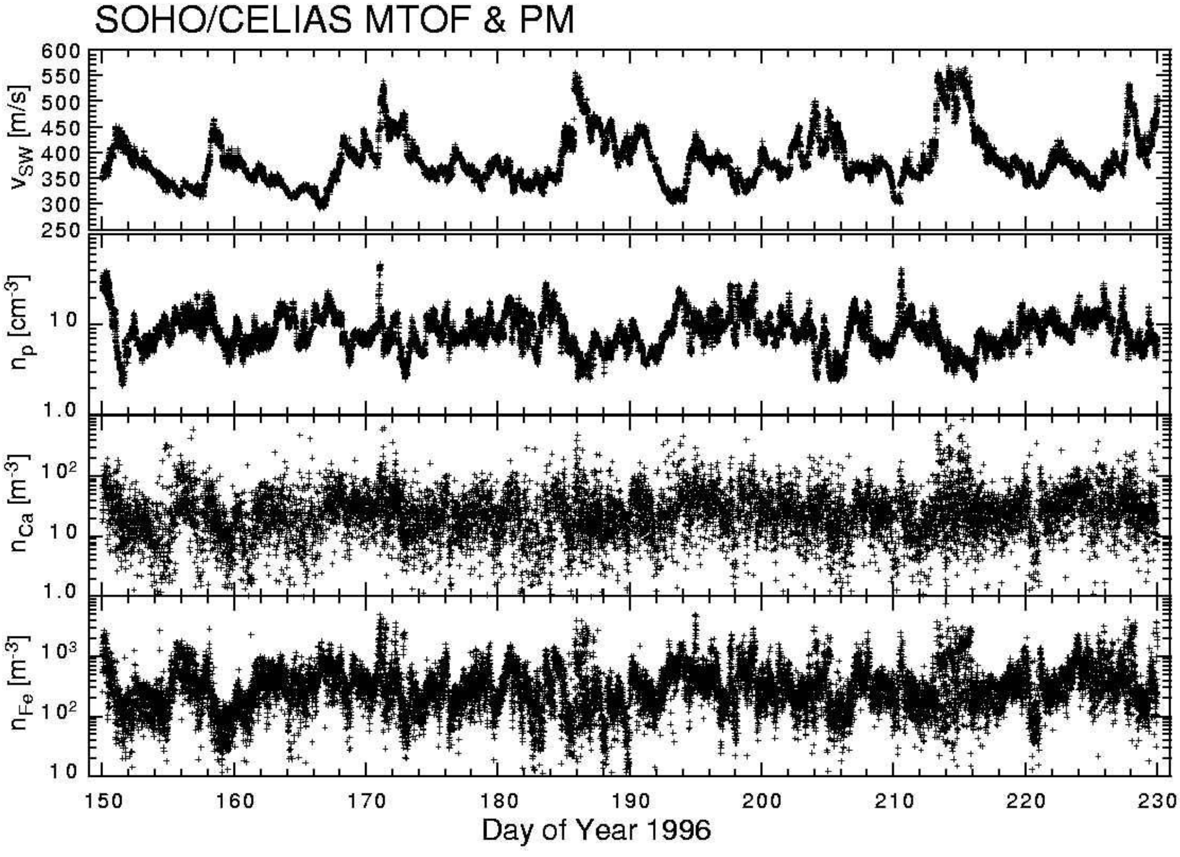

Figure 4-1: Period of 80 days of the data set used in this study, as derived from the MTOF and PM sensors. Data are shown with a time resolution of five minutes. No smoothing has been applied to the data.

mostly 10^+ and 11^+ for a large electron temperature range [73], which makes the data evaluation easier and more reliable. The raw count rates for the Ca peak are typically between 10 and 20 counts in a five-minute spectrum, enough for reliable fitting of the mass line and background subtraction. The main difficulty in the data analysis is obtaining an absolute value for the density in the absence of a pre-flight calibration of the MTOF sensor with calcium ions.

Figure 4-1 shows a section of the data used in the present study. The top two panels show the solar wind velocity and the proton density (as derived from PM measurements) in order to give an impression of the state of the solar wind. The lower two panels give the calcium and iron densities. This is the first time a time series of calcium densities could be measured in the solar wind. Individual measurements obtained from the MTOF sensor at each five-minute measurement step are displayed in Figure 4-1, and no smoothing of the data has been performed. In general, the two heavy ion densities trace each other pretty well with time. However, the calcium density shows more noise than the iron density because its signal is lower by a factor of about ten. A meaningful temporal resolution for further scientific analysis in the heavy ion densities will be around an hour. As has been discussed above (see Chapter 2), the variability in the heavy ion densities is much larger than the variability of the proton density. We find that the correlation between the heavy ion densities and the proton density is less pronounced than the correlation between the heavy ion densities themselves. However, occasionally even very brief features in the proton density are found in the heavy ion densities as well (see DOY 172 or DOY 210, for example).

4.1 Results

The aim of this study was to derive the calcium abundance in the slow and fast solar wind, in a manner similar to that used for the silicon and iron ions. An extended data set has been studied here to derive reliable average abundances of calcium in the solar wind. The data set evaluated for this study spans the time from DOY 30 through DOY 359 of 1996. Thus the data set is also representative of solar wind associated with the quiet Sun. No flares or CMEs, which might interfere with the data analysis, were observed in the particle data during this time period.

The results of the data analysis are given in Figure 4-2, which shows the calcium densities as a function of the solar wind velocity (the proton velocity). Note that the data in Figure 4-2 can shift up or down because the absolute value of the instrument function is still uncertain. What is immediately obvious from Figure 4-2 is that the calcium density is almost constant for a large solar wind velocity range. This is in sharp contrast to what was expected based on the current understanding of the FIP effect. Moreover, this is in contrast to other observations from low-FIP ions like silicon or iron, for which a gradual reduction in their abundance by a factor two to four relative to oxygen was observed in the solar wind velocity range from 380 to 480 km/s, as was reported in Chapter 2 above. For direct comparison, the oxygen, silicon, and iron densities are shown in Figure 4-3. The densities of all these ions drop in the solar wind velocity range from 380 to 480 km/s considerably more than the calcium density. The oxygen density drops only by a factor of less than two, but the iron and silicon densities drop by factors of about three and five, respectively. Upon careful inspection of Figure 4-2, a small, gradual, decrease of the calcium density range from 25 m^{-3} to 16 m^{-3} can be seen over the entire velocity range. This is a smaller decrease in density than we observed even for oxygen, which usually serves as a reference for investigations concerning the abundance of heavy ions in the solar wind. Below and above the velocity range from 380 to 480 km/s the oxygen, silicon, and iron densities remain essentially constant, which is different from the velocity dependence of calcium.

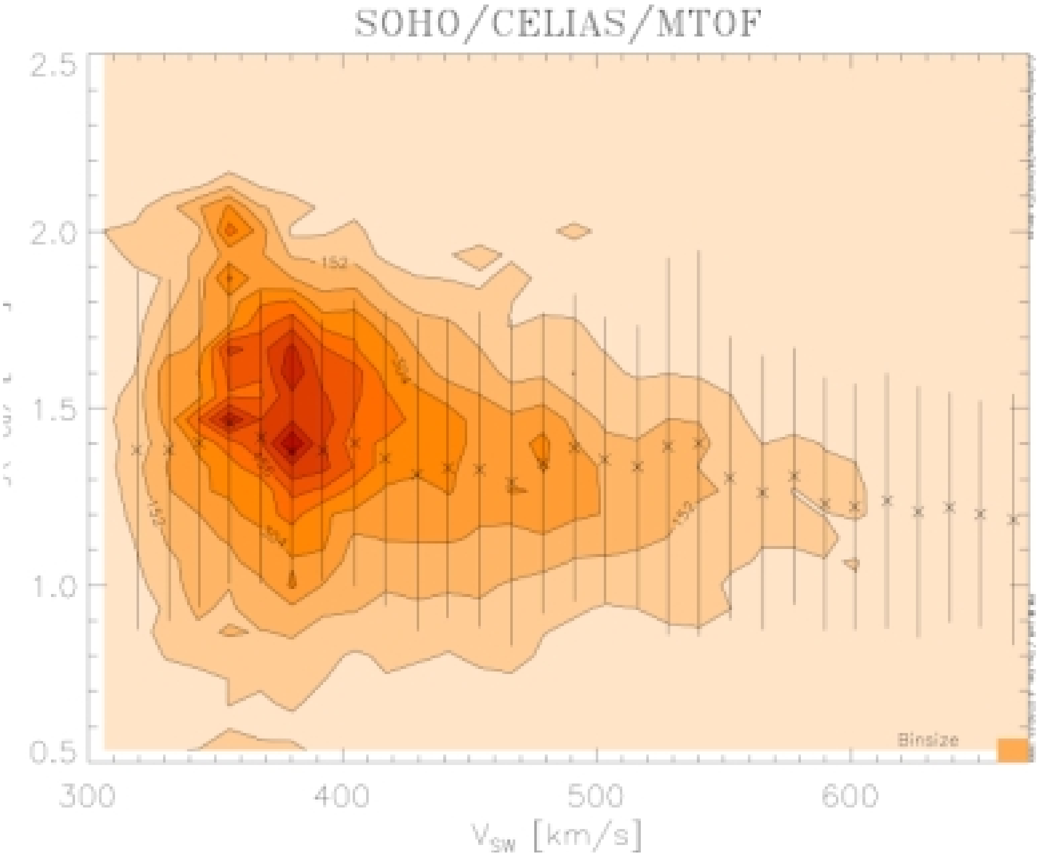

Figure 4-2: Logarithm of calcium densities measured with CELIAS/MTOF versus the solar wind velocity. The ten linearly spaced contours give the number of measurements for a particular bin. Data have been selected from DOY 30 through DOY 359 of 1996. During that time period there was mostly slow solar wind, which explains the clustering of measurements between 300 and 400 km/s. The overlaid symbols are the mean for a particular velocity bin and the error bars are the standard deviation of log(N_{Ca}) for a single measurement.

4.2 Discussion

The present investigation indeed demonstrates that the calcium density shows a different dependence on solar wind velocity from what would be expected for a low-FIP element on theoretical grounds, and it is also markedly different from observations of other low-FIP elements.

When the solar wind abundance data are presented in the usual way, relative to oxygen, the calcium abundance ratio for fast solar wind comes out to be higher than for slow solar wind, since the oxygen density is smaller in the fast solar wind. From the present data analysis we derive a FIP fractionation factor, i.e.,

$$f_{Ca,O} = \frac{\left(n[Ca]/n[O]\right)_{\text{Solar Wind}}}{\left(n[Ca]/n[O]\right)_{\text{Photosphere}}} \qquad \text{Eq. 4-1}$$

of 3.4±0.8 for the slow solar wind and 3.7±0.8 for the fast solar wind for about one year of data during a quiet Sun period. Thus, the earlier finding that calcium has almost the same abundance ratio with respect to oxygen in the slow and in the fast solar wind (see Chapter 3 and [47]), as derived from the analysis of two days of data close in time to the January 6, 1997, CME (one day of slow solar wind and one day of fast solar wind), is confirmed by this more elaborate investigation. That the calcium abundance ratio is higher in the fast solar wind than in the slow solar wind can also be seen in Figure 3-3 above, although the FIP fractionation factors are somewhat larger in the particular time interval around that CME. This is also an indication that to average out the short-term fluctuations in the solar wind one needs more than one day of data for the analysis. Similar results for the FIP fractionation factor are obtained when using

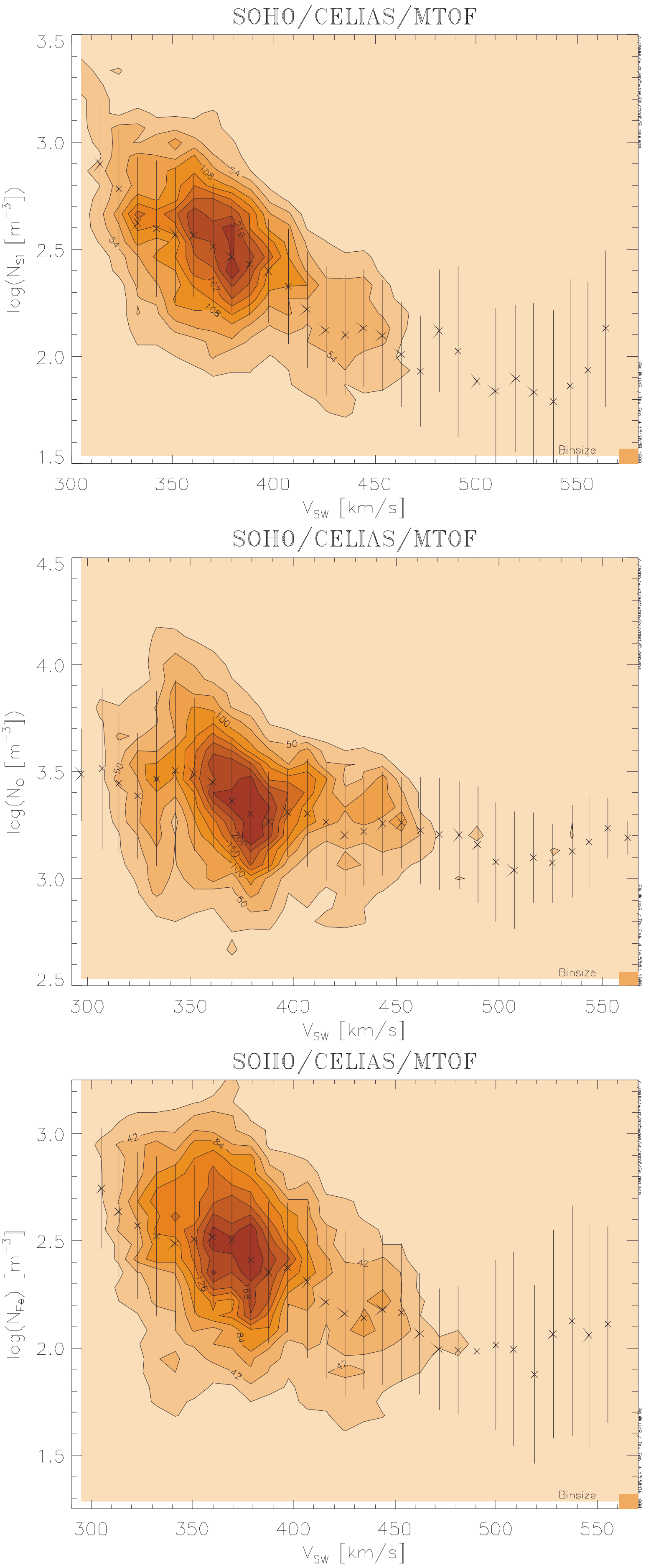

Figure 4-3: The three panels show the logarithms of the densities of oxygen (top), silicon (middle), and iron (bottom) as a function of solar wind velocity. The displayed densities are the data used in Chapter 2, but are now shown directly, and not relative to the oxygen density. The ten linearly spaced contours give the number of measurements for a particular bin. Data have been selected from DOY 30 through DOY 359 of 1996. During that period there was mostly slow solar wind, which explains the clustering of measurements between 300 km/s and 400 km/s. The overlaid symbols are the mean for a particular velocity bin, and the error bars are the standard deviation of $\log(N_X)$ for a single measurement.

Table 4-1: Calcium abundance data in the photosphere, in the solar corona, in SEPs, and in solar flares are given. From the reported measurements calcium abundances in the solar wind at 1 AU is derived using assumptions given below.

Measured regime	Measured quantity	Method	Measured value	Ca/H derived	Ca density [m^{-3}]	Reference
Photosphere	Ca/H	Optical	2.24±0.46 10^{-6}	–	22.4 1)	Ross and Aller [75]
Photosphere	Ca/H	Optical	2.19±0.41 10^{-6}	–	21.9 1)	Lambert and Luck [76]
Photosphere	Ca/H	Optical	2.29±0.12 10^{-6}	–	22.9 1)	Grevesse and Anders [77]
Photosphere	Ca/H	Optical	2.29±0.10 10^{-6}	–	22.9 1)	Grevesse and Sauval [2]
Solar Corona	Ca/H	Optical	$3.24^{+1.33}_{-1.23}\,10^{-6}$	–	32.4 1)	Veck and Parkinson [78]
Solar Corona	Ca/H	Optical	3.6±1.7 10^{-6}	–	35.5 1)	Grevesse and Anders [77]
Solar Flare	Ca/H	Optical	Min. 4 10^{-6} Ave. 6.7 10^{-6} Max. 9 10^{-6}	–	67 1)	Lemen *et al.* [79]
Solar Flare	Fe/Ca	Optical	6.8±1.0 6.0±1.5	1.76±0.37 10^{-5} 4) 2.00±0.58 10^{-5} 4)	46.5 3) 52.7 3)	Phillips and Feldman [80]
Solar Flare	Ca/H	Optical	Min. 3.6 10^{-6} Ave. 5.0 10^{-6} Max. 7.0 10^{-6}	–	36.0 1) 50.0 1) 70.0 1)	Sterling *et al.* [81]
Solar Flare	Ca/H	Optical	Min. 2.510^{-6} Ave. $3.40{\pm}0.42^{-6}$ Max. 4.510^{-6}	–	34.0 1)	Fludra *et al.* [82]
Solar Wind, slow	Ca/Si	Particles	0.049±0.006	4.9±0.8 10^{-6} 5)	19.5 2)	Kern *et al.* [73]
Solar Wind, slow	Ca/O	Particles	0.0134±0.0032	3.12±0.88 10^{-6}	29.1	Wurz *et al.* [47]
Solar Wind, fast	Ca/O	Particles	0.0186±0.0042	5.0±1.5 10^{-6}	35.4	Wurz *et al.* [47]
Solar Wind, slow	n[Ca]	Particles	25±6 m^{-3}	2.36±0.58 10^{-6} 6)	25±6	This work
Solar Wind, fast	n[Ca]	Particles	16±4 m^{-3}	3.17±0.79 10^{-6} 7)	16±4	This work
SEP, mass unbiased baseline	Ca/Si	Particles	0.076±0.042	7.6±4.2 10^{-6} 5)	30.2 2)	Meyer [60]
SEP derived corona	Ca/Si	Particles	$0.082^{\pm 0.014}_{-0.012}$	$8.2^{\pm 2.2}_{-2.0}\,10^{-6}$ 5)	32.6 2)	Breneman and Stone [4]
SEP	Ca/Si	Particles	0.077±0.010	1.02±0.12 10^{-6}	30.6 2)	Reames [83]
SEP derived corona	Ca/H	Particles	3.80±0.70 10^{-6}	–	38.0 1)	Grevesse and Anders [77]
SEP derived corona	Ca/O	Particles	10.6±0.0.4 10^{-3}	6.75±0.98 10^{-6}	67.5 1)	Reames [84]

1) Value is derived by assuming a proton density of 10 cm^{-3} at 1 AU.

2) Value is derived using a Si density of 400 cm^{-3} at 1 AU, from Chapter 2 (see also Figure 4-3).

3) Value is derived using a Fe density of 316 cm^{-3} at 1 AU, from Chapter 2 (see also Figure 4-3).

4) Value is derived using Fe/H = 1.2 10^{-4} from Ipavich *et al.* [33].

5) Value is derived using the Si/O abundance of 0.19 from Bochsler [35] (see also Table 2-2) and an H/O abundance of 1900 from Bame *et al.* [85].

6) The proton density was 10.6±0.6 cm^{-3} during this period in the solar wind velocity range from 300–400 km/s, as measured with CELIAS/MTOF/PM.

7) The proton density was 5.05±0.07 cm^{-3} during this period in the solar wind velocity range >500 km/s, as measured with CELIAS/MTOF/PM.

hydrogen as the reference instead of oxygen, as can be seen in Table 4-1, since hydrogen behaves similarly to a high-FIP element, as was already concluded earlier by Meyer [74].

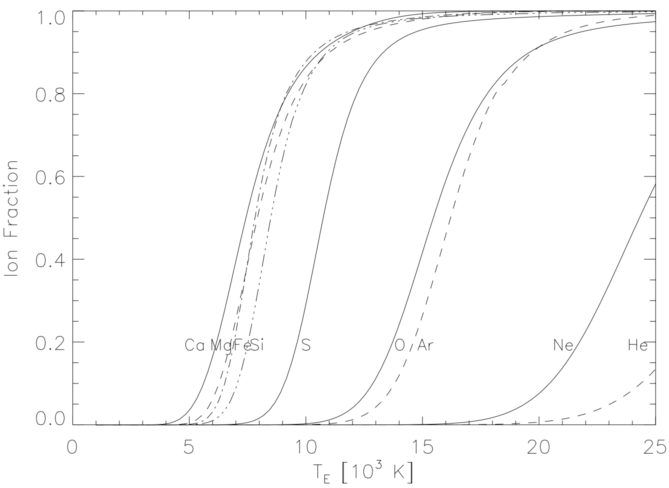

Figure 4-4: Ion fraction for selected elements, considering only ionization by the electron gas at a certain temperature in the solar atmosphere and assuming ionization equilibrium, according to Arnaud and co-workers [23; 24].

Table 4-1 gives a survey of the known measurements of the solar calcium abundance in various regimes together with the solar wind results obtained in this study. Abundance data from the photosphere, the solar corona, SEPs, and solar flares are given. From the reported measurements we tried to derive a Ca/H abundance ratio and a calcium density in the solar wind at 1 AU using certain assumptions detailed in Table 4-1. Apparently the solar corona is somewhat enriched in calcium compared to the photosphere. Using the photospheric calcium abundance [75; 76] we would expect a calcium density of about 22 m^{-3} at 1 AU. Using the solar corona measurement from Veck and Parkinson [78] the expected calcium density is about 32±12 m^{-3} at 1 AU. The calcium density in the solar wind derived in this work is 25±6 m^{-3} for a solar wind velocity range from 300 km/s to 400 km/s. Given the uncertainty in the absolute calibration of MTOF for the calcium measurement, the obtained density value in the solar wind is compatible with the density derived from the photospheric calcium abundance as well as with the density derived from the solar corona abundance. We have to await further calibration work for the MTOF sensor to make a statement regarding whether calcium in the solar wind is actually enriched with respect to its photospheric abundance. Calcium abundance ratios with respect to hydrogen derived from measurements of flares and SEPs show a large variation from event to event. Flares even show considerable variations in their elemental composition during the event itself. This makes SEPs and flares unreliable candidates for the determination of the regular solar wind composition. With some assumptions one can remove the *mass-bias* in the composition of SEPs to derive a so-called “base-line-composition of the SEPs”, which is assumed to be representative for the elemental abundances in the solar corona [60]. This seems to be indeed the case. If for the Ca/Si abundance ratios in SEPs the solar wind density of silicon is used (from Chapter 2), the Ca densities obtained from SEPs agree with the solar corona measurement reasonably well. Feldman *et al.* [86] have found, contrary to the above findings, that low-FIP elements are enhanced in the corona by a factor of about four rather than the high-FIP elements being depleted by this factor. Since this conclusion is based on solar flare observations, this finding seems to be true just for solar flares, but may not be extended to the elemental abundances in the solar corona.

The ionization state of an atom is roughly determined by its FIP. Actually, whether an atom stays neutral or becomes ionized depends upon the atom’s collisional and radiative ionization rates. In the solar atmosphere where the temperature is $T_e \leq 10^4 K$, some elements stay neutral while others become ionized. The fraction of ions for a certain electron temperature is shown in Figure 4-4 for selected elements, considering only ionization by the electron gas in the solar atmosphere and assuming ionization equilibrium [23; 24]. Ionization by UV and EUV radiation will even increase the ion fraction. The grouping of elements in classes of low-FIP (Ca, Mg, Si, Fe, …) and high-FIP (O, Ar, …) is immediately apparent in Figure 4-4. Also the intermediate position of sulfur is reproduced. From Figure 4-4 it appears that the FIP fractionation cannot be limited to the 10^4 K chromospheric temperature plateau and to the lower transition region, as is the generally accepted picture, but must start already much lower in the solar atmosphere where some appreciable amounts of neutral atoms still exist.

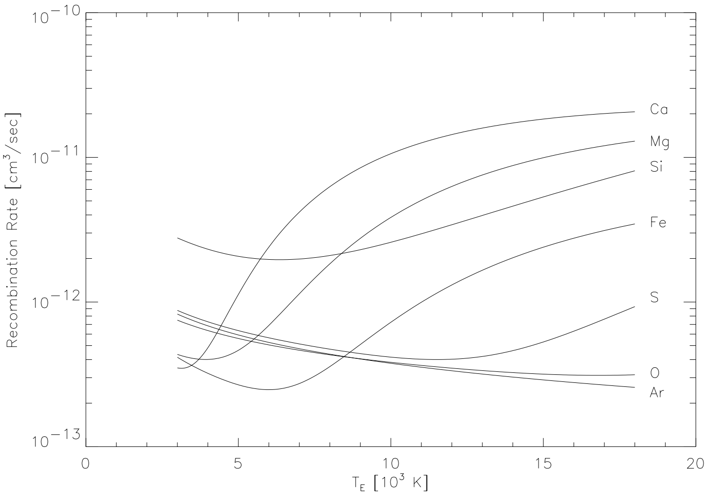

Figure 4-5: Neutralization rates from singly ionized species as derived according to Arnaud and co-workers [23; 24].

Ionization of Ca occurs at a somewhat lower temperature than ionization of the more abundant low-FIP elements Si and Fe, but not low enough to explain the special behavior we reported above. However, we have to consider that the particles start from the solar surface at a temperature of about 6000 K. At this point many elements are already ionized to a large fraction (for example, iron [29]). When rising through the solar atmosphere the particles pass through the temperature minimum around 4000 K at an altitude of about 500 km above the solar surface before the temperature rises again. In that region neutralization of the ions will occur. The recombination rate for neutralization is shown in Figure 4-5 as it is derived from the work of Arnaud and co-workers [23; 24]. Around the temperature minimum, the recombination rate for calcium is very low. Thus we can argue that calcium, which is highly ionized at the solar surface, will stay ionized when passing through the temperature minimum and therefore escapes the FIP-fractionation process. Furthermore, the recombination rate for iron is a factor of about 10 lower than the recombination rate of silicon around the temperature minimum and in the chromospheric temperature plateau. From this difference we conclude that silicon is much more likely to neutralize than iron when passing this region of the solar atmosphere. The difference in the neutralization might explain the different FIP factors we found for Si and Fe in Chapter 2. We found that in the slow solar wind both Si/O and Fe/O were enriched by a factor of about four compared to the respective photospheric values. In the coronal-hole-associated wind, however, the Fe/O ratio was about a factor of two higher than in the photosphere, but the Si/O was almost photospheric. This difference can be explained by silicon being neutralized more effectively than iron and silicon thus being depleted more by the ion-neutral fractionation process. Magnesium shows a FIP pattern similar to that of iron (see, for example, Geiss *et al.* [32] and Figure 3-3), and also has a low neutralization rate in this region of the solar atmosphere.

Fludra *et al.* [82] determined the abundances of S, Ca, and Fe relative to hydrogen for several flares. The authors also performed detailed analysis of the abundance ratios with respect to the temperature of the flare at the time when the spectra were taken. S/H and Fe/H showed a strong dependence on the flare temperature, whereas the Ca/H abundance ratio was almost independent of the electron temperature. This finding also suggests that calcium is ionized far down in the solar atmosphere before the flare acceleration takes place.

4.3 Conclusions

From the present analysis we conclude that oxygen and thus also the other high-FIP elements are depleted, rather than the low-FIP elements being enriched, in the solar wind. The main reason for this conclusion is that the calcium density shows very little change with changing solar wind velocity compared to the other low-FIP elements, but also compared to oxygen. Calcium is already ionized low in the solar atmosphere, and therefore escapes the FIP-fractionation process, which presumably is taking place in the upper chromosphere and lower transition region. The FIP-fractionation process is basically an ion-neutral separation process [3; 5; 12]. Only the ions are further accelerated in the solar corona to become part of the solar wind. Therefore, elements being ionized faster (low-FIP elements) will have an advantage over elements, which become ionized later (high-FIP elements). From this, one can also conclude that high-FIP elements are depleted with respect to low-FIP elements. That the high-FIP elements are depleted is in agreement with a large survey by Meyer [87] of elemental abundances in SEPs, in the solar wind, and in galactic cosmic-ray sources, for which he also found a depletion of high-FIP elements. This conclusion is also in agreement with the measurements of the elemental abundances in the solar corona by Veck and Parkinson [78]. Also in recent optical measurements of elemental abundances in coronal streamers performed with SOHO/UVCS by Raymond *et al*. [37; 38], a “depletion of the high-FIP elements oxygen and sulfur by a factor of three compared to low-FIP elements” was found.

Recently, Feldman [54] and Falconer *et al*. [88] introduced the class of very low-FIP elements with a FIP lower than 6.1 eV to distinguish these elements from low-FIP elements with a FIP from 7.5 eV to 10 eV. This new category was introduced due to their different behavior from that of the other low-FIP elements.

Finally, we conclude that oxygen is not a good reference to study elemental abundance ratios in the solar wind, since its density changes with solar wind velocity. Neither do hydrogen, although by far the most abundant element, and silicon appear to be particularly advantageous, since their densities also change significantly with solar wind velocity. From this analysis it appears that calcium is best suited to serve as a reference to study abundance ratios. Elements with very low FIP, like Al (5.98 eV), Na (5.14 eV) and perhaps even Cr (6.76 eV), probably will show similar dependence of their density on the solar wind velocity.

5 The MTOF Sensor

The Mass Time-of-Flight (MTOF) sensor is a high mass resolution mass spectrometer using an isochronous time-of-flight geometry for the determination of the mass of an incoming ion. Since the determination of the ion's mass is independent of the ion energy, no energy selection in the entrance system is necessary. Therefore, an entrance system with a wide energy acceptance is used for MTOF. This results in high sensitivity of the MTOF sensor combined with unprecedented mass resolution. Since no energy per charge scan of the entrance system is necessary, the MTOF sensor has a theoretical duty cycle of 100%. In reality, the sensor settings are cycled in six steps to cover the entire parameter space of the solar wind plasma for all heavy ions up to Ni. Depending on the ion under consideration and solar wind plasma parameters, this stepping procedure can reduce the duty cycle to about 50%.

5.1 The MTOF Entrance System

The MTOF entrance system is a Wide Angle Variable Energy/Charge electrostatic analyzer (WAVE). The WAVE entrance system was designed and built at the University of Bern. The function of WAVE is to accept solar wind ions over a large energy range as well as over a large range of incident angles (in the ecliptic plane along α, and out-of the ecliptic plane) and transmit them to the V-MASS mass spectrometer while eliminating the dominant proton component. Furthermore, WAVE efficiently suppresses the large flux of solar photons (UV and visible ranges) by more than eight orders of magnitude.

The WAVE consists of three staggered boxes of cylindrical symmetry (see Figure 5-1). High transparency grids at ground potential cover the front of each box. The voltage on the rear of each box is V_{WAVE}. With the help of three guarding rings along the inside perimeter of the boxes, a homogenous electric field is generated. Theoretically, the ion trajectories inside each box are parabolas. In reality, the trajectories are complicated by the lensing effects of the finite mesh size of the three grids and the non-ideal boundary conditions of the metallized guarding rings on the inside of each box.

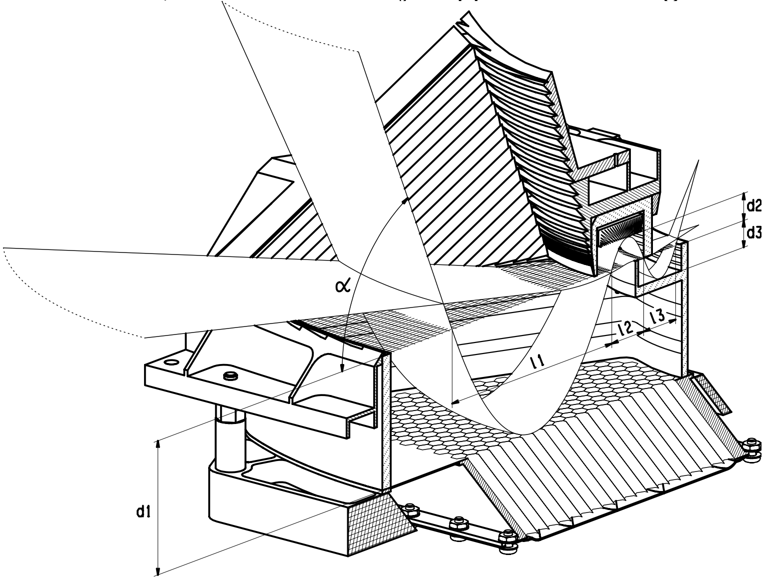

Figure 5-1: Schematic view of the MTOF WAVE entrance system. α is the incident angle in the ecliptic plane with respect to the ground plane, d_i are the individual box heights, and l_i are the lengths of the ion path parabolas projected on the ground plane.

The relative sizes of the boxes and the overall geometry are chosen such that for a given voltage, solar wind ions are accepted within an energy-per-charge range from $(E/Q)_{\min}$ to $(E/Q)_{\max}$, with a factor of five between these two limits. Basically, all solar wind heavy ions are accepted by WAVE; only protons and alpha particles are rejected under ideal operational conditions. The angular acceptance of WAVE ranges from 20° to 70° in the ecliptic plane and –25° to +25° out-of the ecliptic plane.

5.2 The Isochronous Mass Spectrometer

The application of carbon-foil time-of-flight (TOF) mass spectrometers to space science was a major improvement over previous instrumentation, providing detection efficiency and mass resolution exceeding previous instrumentation for solar wind plasma research considerably. In carbon-foil TOF instruments, an incoming particle is identified by having it pass a thin carbon foil (≈100Å) to produce a start signal and then measuring the elapsed time until the particle hits a stop detector at a given distance. Knowing the energy of the particle, its mass can be inferred from the flight time. This type of spectrometer was first proposed for measurements in space by Gloeckler and Hsieh [89] and has been successfully employed since then (for example, see references [90-93]). For cases when the resolution of isotopes or the unambiguous identification of molecules is needed, significant improvements to this type of mass spectrometer must be made. Isochronous TOF mass spectrometers have the necessary capabilities for these measurements.

5.2.1 Theory of Operation

In an isochronous TOF mass spectrometer, ions travel in a suitably configured electrostatic field, where the flight time depends solely on their mass-per-charge ratio and is independent of the initial conditions of the ions. Only the fraction of the incident particles emerging from the carbon foil as singly charged ions can be used. Independent of their initial charge state, the majority of particles leaves the foil neutral or as singly charged ions, because of efficient charge-exchange processes during passage of the carbon foil [16-18; 94]. The neutral particles are not deflected by the electrostatic field, and leave the isochronous TOF section. Since multiply charged ions are rare at the energies considered, the mass-per-charge spectrum consists mainly of singly charged ions and thus corresponds largely to a pure mass spectrum, with little interference from doubly charged species.

Within the analyzer section of an isochronous TOF instrument, the ions are reflected back to the entrance plane by a linearly increasing electrostatic field of the form

$$E(z) = -2wz,$$

which is derived from an electric potential of the form

$$\Phi(z) = wz^2$$

with w being the scaling constant. The z direction is taken perpendicular to the entrance plane (the xy plane), which is located at $z = 0$. Since the motion of the ion in z direction is independent of the motion in the xy plane, the motion in z direction is described by

$$\frac{d^2z}{dt^2} + 2w\frac{q}{m}z = 0 \qquad \text{Eq. 5-1}$$

with q and m the elementary charge and the mass of the particle, respectively. The solution of Eq. 5-1 describes a harmonic oscillation along the z-axis with a half-period of

$$t_{TOF} = \pi\sqrt{\frac{1}{2w}\frac{m}{q}} \ . \qquad \text{Eq. 5-2}$$

The period of this oscillation is independent of the initial conditions such as initial energy or entrance angle. Therefore, the TOF of an ion is only proportional to the square root of the mass per charge. For an ideal isochronous configuration, the resolution is only limited by the resolution of the time measuring system. An initial energy or angular spread will not degrade the mass resolution, and thus the mass/charge of the ions can be determined accurately. This was successfully demonstrated with a laboratory instrument [95]. For space applications, mass resolutions of 100 and more can be reached when the geometry of the electric field is close to ideal. However, realizations of isochronous instruments so far either approximate the electric field to a limited degree [96; 97] or use a configuration with an incomplete harmonic field combined with a linear TOF section [98]. The latter instrument, the so-called V-type mass spectrometer (or V-MASS), is currently in use on several space missions [6; 99; 100], and will be discussed in detail in this section. Recently, a new type of isochronous TOF mass spectro-

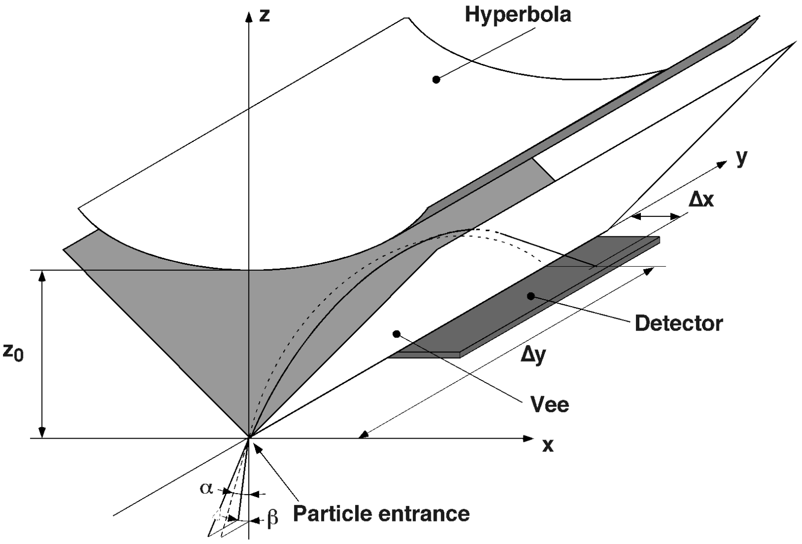

Figure 5-2: Schematics of a V-type isochronous mass spectrometer. The carbon foil is located at the particle entrance. Particles coming from a direction (α,β) move according to the electrostatic forces (solid bold line) until they exit through the sides of the Vee. The dashed line is the projection of the trajectory on the *yz* plane.

meter was introduced with a cylindrically symmetric harmonic potential which allows an almost exact realization of the ideal field [101; 102], and with a performance exceeding the currently used instruments [103].

The underlying physical principle of the V-type mass spectrometer is that the potential inside a quadrupole exhibits a quadratic behavior. Thus, one quadrant of such a quadrupole can serve as an isochronous mass spectrometer. It was realized already in the late 1960's that the harmonic field of a quadrupole can be used for a compact mass spectrometer (see review by Carrico [104]), but only limited experimental success with this type of mass spectrometer was accomplished, basically demonstrating the feasibility of the concept. For laboratory applications this type of mass spectrometer was not pursued any further, since better performance with simpler design is achieved with reflectron TOF instruments. For a space application, Hamilton and co-workers [98] were the first to build a prototype of a V-type isochronous mass spectrometer. Currently, instruments of this type are in use on the WIND mission in the SMS/MASS sensor [99], on the SOHO mission in the CELIAS/MTOF sensor [6], and on the ACE mission in the SWIMS sensor [100]. Figure 5-2 shows the schematics of the V-type instrument. The potential between the two electrodes (the hyperbola and the V-shaped ground plate, the "Vee") is given by

$$V(x,z)=\frac{\Phi_0}{z_0^2}\left(z^2-x^2\right) \qquad \text{Eq. 5-3}$$

with Φ_0 the voltage on the hyperbola and z_0 the separation of the hyperbola from the Vee, which is electrically grounded. This configuration produces the desired electric field with the linear increase in field strength in *z* direction.

We break the ion trajectory into two parts to calculate the flight time, where t_1 is the flight time inside the harmonic potential and t_2 is the flight time from the Vee to the detector. Before we go any further with the calculation, we introduce the following abbreviations to be used from here on

$$\tan\beta=\frac{v_{0x}}{v_{0z}} \quad \text{and} \quad t_0=\pi\sqrt{\frac{z_0^2}{2\Phi_0}\frac{m}{q_0}} \; .$$

The trajectory inside the harmonic potential is derived by integrating the acceleration from the electric field exerted on the ion along the trajectory

$$\begin{aligned} v_x(x)&=\frac{\pi}{t_0}\sqrt{x^2+v_{0x}^2\left(t_0/\pi\right)^2} \\ v_y(y)&=v_{0y} \\ v_z(z)&=\frac{\pi}{t_0}\sqrt{-z^2+v_{0z}^2\left(t_0/\pi\right)^2} \end{aligned} \qquad \text{Eq. 5-4}$$

with v_{0x}, v_{0y}, and v_{0z} being the components of the initial velocity of the ion exiting the carbon foil at $x=0$, $y=0$, and $z=0$. Further integration along the trajectory in the quadratic potential leads to

$$\begin{aligned} x(t) &= v_{0x}\frac{t_0}{\pi}\sinh\left(\pi\frac{t}{t_0}\right) \\ y(t) &= v_{0y}t \\ z(t) &= v_{0z}\frac{t_0}{\pi}\sin\left(\pi\frac{t}{t_0}\right) \end{aligned} \qquad \text{Eq. 5-5}$$

The ion leaves the Vee at a time t_1, which is where $x(t)=z(t)$. Thus we can calculate t_1 from

$$v_{0x}\sinh\left(\pi\frac{t_1}{t_0}\right) = v_{0z}\sin\left(\pi\frac{t_1}{t_0}\right) \qquad \text{Eq. 5-6}$$

For a start location other than $x_0=0$ we have to extend the right-hand side of Eq. 5-6 such that

$$v_{0x}\sinh\left(\pi\frac{t_1}{t_0}\right) = v_{0z}\sin\left(\pi\frac{t_1}{t_0}\right) + x_0\frac{\pi}{t_0}\cosh\left(\pi\frac{t_1}{t_0}\right) \qquad \text{Eq. 5-7}$$

on the left-hand side of Eq. 5-6. After leaving the Vee, the flight time of the ion in the field-free area between the Vee and the detector (located at $z=0$) is given by t_2

$$t_2 = -\frac{z(t_1)}{v_z(t_1)} = -\frac{t_0}{\pi}\tan\left(\pi\frac{t_1}{t_0}\right) .$$

The total flight time, t_{TOF}, is the sum of t_1 and t_2. For $\beta=0$ the solution of Eq. 5-7 is trivial and we get

$$t_{TOF} = t_0 = \pi\sqrt{\frac{z_0^2}{2\Phi_0}\frac{m}{q_0}} \qquad \text{Eq. 5-8}$$

For $\beta=0$ the flight time depends only on the mass per charge (and a constant instrumental parameter), but does not depend on the initial energy of the incoming ion. In the following we will investigate the case for $\beta\neq0$ and for $x_0\neq0$. For that purpose we have to solve Eq. 5-7, which is not possible analytically. The total flight time of ions as a function of β and x is displayed in Figure 5-3 using a numeric evaluation of Eq. 5-7. It is obvious that the flight time becomes longer for increasing β. Starting from a location $x_0\neq0$ makes this deviation even worse (see Figure 5-3). Therefore, the acceptance angle β of the detector has to be limited for sufficient time resolution and therefore mass resolution. For the same reason the entrance aperture size needs to be limited to a small value of x_0, which reduces the active area of this type of instrument.

To simplify further calculations we introduce the following abbreviations for the flight times in the two regions

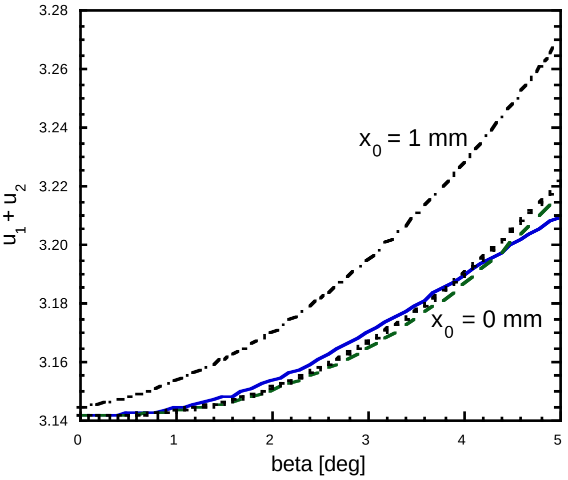

Figure 5-3: Dependence of TOF, u_1+u_2, on the angle β for a V-type instrument is shown by numerically solving Equation 5-6 and calculating the total flight time (pointed line) for x_0 = 0mm. For comparison the results from the approximations from equation 5-8 (solid line) and from Bürgi [105] (dashed line) are given. The numeric solution for x_0 = 1mm is also given (dashed-pointed line).

$$u_1 = \pi t_1 / t_0 \text{ and } u_2 = \pi t_2 / t_0$$

with

$$u_1 + u_2 \geq \pi$$

To obtain an approximation for the deviation of the flight time from t_0, we expand the left-hand and right-hand sides of Eq. 5-6 around $u_1 = \pi$. Using the approximation

$$\sin(u) \approx \frac{\exp(\pi)}{2}\left(1 + (u-\pi) + \frac{1}{2}(u-\pi)^2 + \cdots\right)$$

we get

$$u_1 \approx \pi - \left(\frac{\beta e^{\pi}}{2} + 1\right) + \sqrt{\frac{\left(\beta e^{\pi}\right)^2}{4} + 1}$$

For $\beta = 3°$ this approximation leads to $u_1 = 2.705$, which is close enough to the precise numerical value of 2.730 for u_1. One clearly sees that the ions can spend a considerable time outside the harmonic potential (approximately the remainder to π), which is the reason to describe this instrument type by an incomplete harmonic field. With the expansion

$$\tan(x) = x + \frac{x^3}{3} + \cdots$$

we get for the total flight time

$$t_{TOF} = t_1 + t_2 = \frac{t_0}{\pi}(u_1 + u_2) \approx t_0\left(1 + \frac{1}{3\pi}\left(\left(\frac{\beta e^{\pi}}{2} + 1\right) - \sqrt{\frac{\left(\beta e^{\pi}\right)^2}{4} + 1}\right)^3\right) \qquad \text{Eq. 5-9}$$

Fortunately, the first-order and second-order terms in u_1 and u_2 cancel out and the deviation of the flight time from t_0 is proportional to β^3. This explains that a V-type instrument has good mass resolution in spite of the fact that the ions travel a considerable time in field-free space. Up to $\beta = 5°$ this approximation is close to the exact numerical result. Expanding the individual terms to higher order yields an expression that is of course valid for even larger β [105]. The result of this approximation as well as the result derived by Bürgi [105] are shown in Figure 5-3. The flight time increases with β and x_0 but is still independent of the initial energy and angle. This describes a theoretical limit for the mass resolution to be obtained with a V-type instrument for a given detector width. Since the flight time only increases with deviations from the nominal entry conditions ($x_0 = 0$ and $\beta = 0$) we get an asymmetric appearance of the mass peaks in the recorded spectra if the entry conditions of the recorded ions have a distribution in x and β, which is usually the case. If this distribution is not centered along $x_0 = 0$ and $\beta = 0$ then even the average flight time (the peak center) increases, which has to be taken into account in the data analysis.

5.2.2 Mass Resolution

The mass resolution of a time-of-flight instrument is determined by the ratio of the flight time of an ion divided by its variation

$$\frac{m}{\Delta m} = \frac{1}{2}\frac{t_{TOF}}{\Delta\tau}$$

with the factor one half resulting from the quadratic dependence of the mass from the flight time (Eq. 5-8). For a V-type instrument we have to consider three contributions to $\Delta\tau$: the uncertainty of the TOF measurement, $\Delta\tau_e$; the theoretical limitations imposed by a spread in β and by x, $\Delta\tau_{\beta,x}$; and a term, $\Delta\tau_d$, resulting from the fact that the detector cannot be placed directly in the plane of vanishing z in a practical realization. Therefore we get

$$\left(\frac{m}{\Delta m}\right)=\frac{1}{2}\left(\frac{t_{TOF}}{\Delta\tau}\right)=\frac{1}{2}\left(\left(\frac{\Delta\tau_e}{t_{TOF}}\right)^2+\left(\frac{\Delta\tau_{\beta,x}}{t_{TOF}}\right)^2+\left(\frac{\Delta\tau_d}{t_{TOF}}\right)^2\right)^{-\frac{1}{2}} \qquad \text{Eq. 5-10}$$

The uncertainty of the TOF measurement, $\Delta\tau_e$, is a combination of the resolution of the electronics and the TOF dispersion of the start electrons on their way from the C-foil to the start detector. This uncertainty is constant; it does not depend on the particle's energy or mass. Therefore we can write

$$\frac{\Delta\tau_e}{t_{TOF}}=\frac{\Delta\tau_e}{\pi}\sqrt{\frac{2\Phi_0}{z_0^2}\frac{q_0}{m}} \qquad \text{Eq. 5-11}$$

The contribution from the second term has already been discussed above (see Figure 5-3). For the last term in Eq. 5-10 we have to evaluate the flight time differences for particles moving along a short linear TOF of length d_z with energies differing from the nominal energy E by $\pm\Delta E$

$$\Delta\tau_d=\frac{d_z}{4}\sqrt{\frac{2m}{E}}\left(\frac{\Delta E}{E}\right)_{C-foil}\approx\frac{d_z}{2\sqrt{2}}\frac{k_e}{E} \qquad \text{Eq. 5-12}$$

where ΔE is mainly caused by the energy straggling in the carbon foil. In Eq. 5-12 an approximation for the energy straggling is used [106; 107] with k_e being a constant. Of course, the energy resolution of the entrance system or the plasma temperature have to be folded into ΔE, which usually contributes only little to $\Delta\tau_d$ for these instruments. Figure 5-4 shows the calculated mass resolution together with published experimental results from the laboratory prototype [98], the calibration data for the WIND/SMS/MASS sensor [99] and the calibration data for the SOHO/CELIAS/MTOF sensor [6]. For the MTOF sensor the mass resolution during flight is between 65 and 100 depending on the MTOF sensor settings and the solar wind parameters. This value for the mass resolution is derived from the five-minute mass spectra recorded by MTOF.

The mass resolution scales linearly with z_0 (through t_{TOF}), and is mainly limited by the acceptance angle and the aperture size. For ions of low mass, limitations caused by $\Delta\tau_e$ become noticeable. In spite of these theoretical and practical limitations, the V-type instruments currently in use [6; 99] have sufficient mass resolution for isotope analysis at the expense of overall detection efficiency. For the data analysis we do not

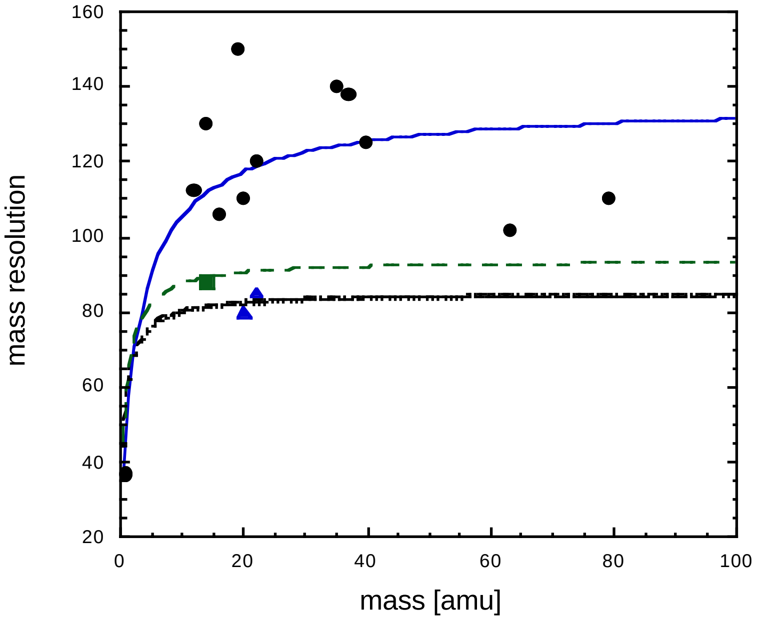

Figure 5-4: Mass resolution of V-type isochronous mass spectrometer as determined by Eq. 5-10 for $\beta = 1.5°$ (solid line), $\beta = 2.3°$ (dashed line), and $\beta = 3.0°$ (textured line) using $z_0 = 5cm$ and $\Phi_0 = 20kV$. Some experimental results are indicated by symbols: circles [98], squares [99], and triangles [6].

need to know the precise value of the mass resolution for a certain mass, since the peaks are fitted. But it is important to know what resolution can be expected so that the fitting routine does not run astray.

The importance of the angular acceptance arises from the angular scattering of the ions in the carbon foil, in addition to the angular acceptance of the ion optical entrance system. The angular scattering in the carbon foil is substantial (on the order of ±10°; see Chapter 6.3.1) for the ion energies in the range of keV/nuc [108]. For good overall detection efficiency, the mass spectrometer needs a large angular acceptance. For the V-type instrument, evaluation of the angular acceptance is straightforward. In y direction the instrument is built long enough to accept most of the scattered ions in α direction. In β angle the angular acceptance is constrained by the detector width. A trade-off between mass resolution and angular acceptance is necessary.

6 The MTOF Instrument Function

In this chapter we will describe the MTOF instrument function. Basically, the instrument function consists of two major parts. One part describes the WAVE entrance system, which is based largely on calibration. The other part describes the V-MASS time-of-flight mass spectrometer, which is based largely on computer simulation and theory. Also the interface between WAVE and V-MASS is described here. For the calculation of the instrument function some assumptions about the nature of the solar wind have to be made, which are given at the end of this chapter.

6.1 The Entrance System

The WAVE entrance system was calibrated at the CASYMS calibration facility at the University of Bern [109; 110]. The calibration was performed at the component level, with the WAVE entrance system alone, with the WAVE entrance system integrated into the MTOF sensor, and with the WAVE entrance system integrated in a V-MASS mock-up. The calibration data are available in the form of an active area depending on the energy per charge E/Q, the angle in the ecliptic plane, α, and the angle out-of the ecliptic plane, β, of the incoming ion

$$A = A\left(k_{WAVE}, \alpha, \beta\right) \qquad \text{Eq. 6-1}$$

with k_{WAVE} the analyzer constant of the WAVE entrance system

$$k_{WAVE} = \frac{E/Q}{V_{WAVE}} \qquad \text{Eq. 6-2}$$

being the ratio between E/Q and V_{WAVE}, the WAVE voltage. The calibration data are available in the form of a three-dimensional array, with 23 steps along the k_{WAVE} axis (ranging from 0.2857 to 5.4286, spaced non-linearly), 10 steps along the α-axis (ranging from 25° to 70° in steps of 5°), and 4 steps along the β-axis (for 10°, 0°, –10°, and –20°, with the data at 20° taken to be equal to the data at –20°). Outside this range of values for E/Q, α, and β, the active area is zero. In order to have a finer grid the three-dimensional array of calibration data has been linearly interpolated along the k_{WAVE} axis to 46 steps. Also, two steps on the β axis at –5° and 5° have been added by linear interpolation to overcome the rather large steps of 10° with respect to the out-of ecliptic angle, which deviates from 0° by a few degrees in both directions for typical solar wind.

The calibration data were taken at the CASYMS calibration facility using a pencil ion beam. The solar wind, however, has a considerable kinetic temperature. Therefore, the measured acceptance of the WAVE entrance system in E/Q, α, and β for a pencil beam has to be convoluted with the distribution of the actual solar wind ions at the time when the data were recorded by MTOF. For this convolution, the solar wind is assumed to have a three-dimensional Maxwellian distribution characterized by a temperature T_i that is convected away from the Sun with the bulk velocity $\vec{v}_b$. Different temperatures parallel and perpendicular to the magnetic field are not considered since this information is not available from the CELIAS data set. Non-Maxwellian tails are not included either since the fluxes associated with these tails are very low. Also, it is assumed that the distribution is spatially uniform on the length scale of the sensor. The solar wind distribution is described by

$$f_{SW}^{i}(\vec{v}) = n_i \left(\frac{m_i}{2\pi k_B T_i} \right)^{\frac{3}{2}} \exp\left(-\frac{m_i \left(\vec{v} - \vec{v}_{i,0} \right)^2}{2 k_B T_i} \right) \qquad \text{Eq. 6-3}$$

with n_i being the density of an ion species *i*, T_i its temperature, $\vec{v}$ its velocity, and $\vec{v}_{i,0}$ the bulk velocity of the species *i*. The bulk velocity of the heavy ions (species *i*) is taken to be a little bit higher than the proton velocity depending on species and proton velocity (see Chapter 8.2.2).

For most of the time, the ion temperature is proportional to the mass of the ion [111]; that is, the ratio T_i/m_i remains constant and can be taken from the proton measurement T_p/m_p:

$$v_{therm} = \sqrt{\frac{2k_B T_i}{m_i}} = \sqrt{\frac{2k_B T_p}{m_p}} \qquad \text{Eq. 6-4}$$

with v_{therm} being the thermal velocity, a parameter which is measured by the PM. For the data analysis discussed in the following it is always assumed that Eq. 6-4 is valid. Observations show that this assumption is true most of the time [111], with rare exceptions occurring sometimes at slow solar wind velocities [22]. Thus it is more convenient to write Eq. 6-3 as

$$f_{SW}^{i}(v_x, v_y, v_z) = \frac{n_i}{(\pi v_{therm})^{\frac{3}{2}}} \exp\left(-\frac{(v_x - v_{i,0,x})^2}{v_{therm}^2} - \frac{(v_y - v_{i,0,y})^2}{v_{therm}^2} - \frac{(v_z - v_{i,0,z})^2}{v_{therm}^2} \right)$$

with the $v_{i,0}$ being the Cartesian components of the bulk velocity of species i in the solar wind. In the spherical coordinate system used for the MTOF sensor the distribution can be written as follows

$$\begin{aligned} f_{SW}^{i}(v,\alpha,\beta) = \frac{n_i}{(\pi v_{therm})^{\frac{3}{2}}} \cdot \exp\left(-\frac{(v - v_{i,0})^2}{v_{therm}^2} \cos^2\beta_b \cos^2\alpha_b \right) \times \\ \exp\left(-\frac{v_{i,0}^2 \cos^2\beta_0}{v_{therm}^2} (\sin\alpha - \sin\alpha_b)^2 \right) \times \\ \exp\left(-\frac{v_{i,0}^2}{v_{therm}^2} (\sin\beta - \sin\beta_b)^2 \right) \end{aligned}$$

with α_b and β_b the solar wind bulk flow direction in the ecliptic plane and perpendicular to it, respectively. This representation assumes that the particle flow to the spacecraft is in x direction and the ecliptic plane is in the x-y plane with y pointing in the direction of spacecraft movement and the z direction completing a right-handed coordinate system. The distribution can be approximated very well by

$$f_{SW}^{i}(v,\alpha,\beta) = \frac{n_i}{(\pi v_{therm})^{\frac{3}{2}}} \exp\left(-\left(\frac{v - v_{i,0}}{v_{therm}}\right)^2 - \left(\frac{\alpha - \alpha_b}{\alpha_{therm}}\right)^2 - \left(\frac{\beta - \beta_b}{\beta_{therm}}\right)^2 \right) \qquad \text{Eq. 6-5}$$

with

$$\alpha_{therm} = \beta_{therm} = \arctan\frac{v_{therm}}{v_{i,0}}$$

To obtain the effective area with which the MTOF "sees" the solar wind, A_{eff}, we have to convolute the distribution of the solar wind with the active area of WAVE. Since the active area of WAVE is given in polar coordinates we rewrite

$$A_{eff}(v,\alpha,\beta) = \iiint A(k_{WAVE},\alpha,\beta) \frac{f_{SW}^{i}(v,\alpha,\beta)}{n_i} v^2 dv\, d\alpha \cos\beta\, d\beta \qquad \text{Eq. 6-6}$$

using only the normalized part of the solar wind distribution, and with α being the angle in the ecliptic plane and β being the angle out-of the ecliptic plane. Inserting Eq. 6-5 in Eq. 6-6 we obtain

$$A_{eff}(v,\alpha,\beta) = \frac{1}{(\pi v_{therm})^{\frac{3}{2}}} \iiint A(k_{WAVE},\alpha,\beta) \times$$

$$\exp\left(-\left(\frac{v-v_{0,i}}{v_{therm}}\right)^2\right)\exp\left(-\left(\frac{\alpha-\alpha_b}{\alpha_{therm}}\right)^2\right)\exp\left(-\left(\frac{\beta-\beta_b}{\beta_{therm}}\right)^2\right)v^2 d v\, d\alpha \cos\beta\, d\beta$$

Eq. 6-7

with α_b and β_b being the angles of the bulk flow in the ecliptic plane and out-of the ecliptic plane, respectively. The parameters v_b, v_{therm}, and β_b are measured by the PM ($v_{0,i}$ is derived from v_b). α_b is not measured on SOHO and we have to assume that $\alpha_b = 45°$ (i.e., radial flow, since we don't have this measurement available). α_{therm} and β_{therm} are calculated from v_{therm} assuming a symmetric distribution. It is known that the solar wind exhibits anisotropies in the temperatures (i.e., the thermal velocity) parallel and perpendicular to the magnetic field, particularly further inside the inner heliosphere [112; 113]. This information is not available on SOHO and we have to assume a symmetric distribution for further analysis.

The effective area of WAVE in the plane spanned by the parameters k_{WAVE} and α is shown in Figure 6-1. The acceptance range along the k_{WAVE} coordinate goes from 0.2 to 1, a factor of 5 between the lowest and highest energy transmitted. For the α coordinate the acceptance range goes from 25° to 70°, that is about $\pm 25^\circ$ from the nominal 45° angle. The contours of the ion distributions in the k_{WAVE} and α plane are overlaid in Figure 6-1 for the different iron ions for a solar wind velocity of 350 km/s and a thermal velocity of 30 km/s. In this example the iron ions are located in the center of the acceptance range and the active area for this measurement is large. With higher solar wind velocity the ions will move up in Figure 6-1 toward and beyond the limit of acceptance in k_{WAVE}. The parameter k_{WAVE} is derived from the current value of V_{WAVE} given by the stepping sequence of MTOF and from the current value of E/Q. The current energy, E, is derived from the proton velocity, assuming that the heavy ions have about the same velocity as the protons (with some minor modifications, which will be

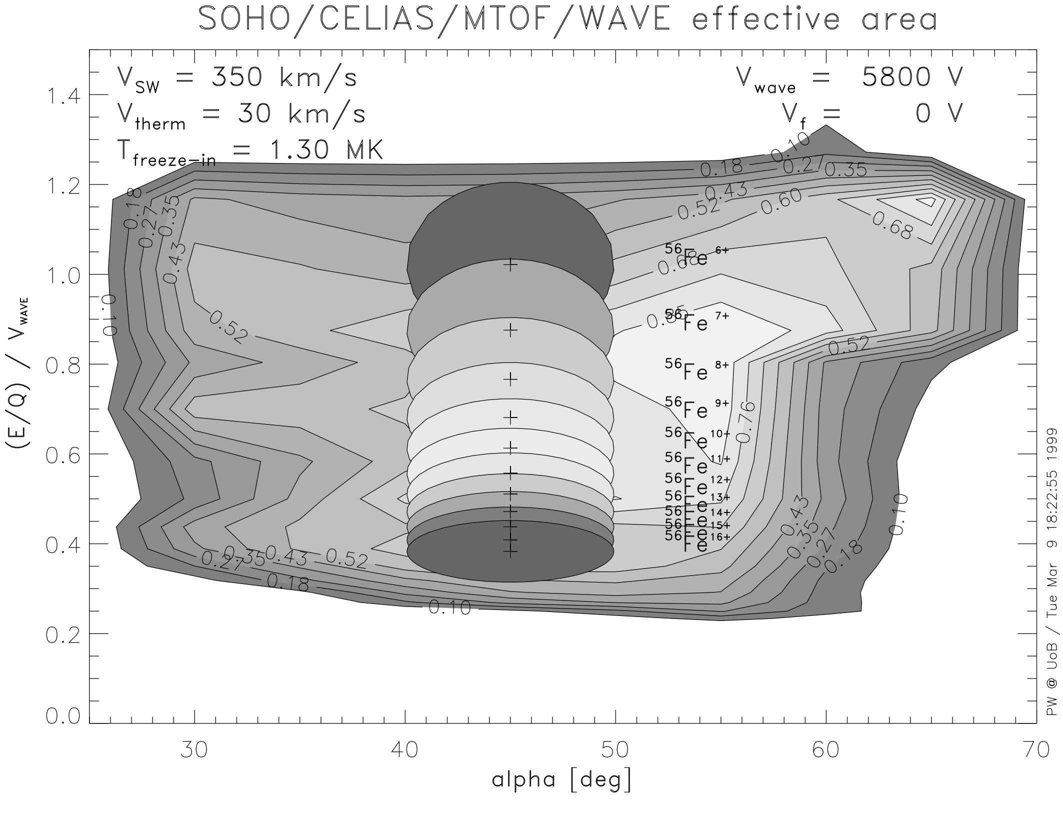

Figure 6-1: Contour plot of the calibration data of the active area of the WAVE entrance system for V_{WAVE} = 5800 V and V_F = 0V. Overlaid are the 50% contours for the different iron ions for a solar wind velocity of 350 km/s and a thermal velocity of 30 km/s. The gray levels are logarithmically coded for the ion intensity (derived from an electron temperature of 1.3 MK), with the brightest contour being 1, then 0.3, 0.1, until 10^{-5}. The crosses indicate the center of the distribution of the ions in this parameter plane.

given later in Chapter 8.2.2). The ionic composition of the solar wind is not measured by MTOF, and for most of the time during the SOHO mission it is not measured by any other sensor either. Thus, the charge—or rather, the charge distribution—for an element of interest has to be derived by some other means. This will be discussed in detail in Chapter 8.2.1.

The triple integral of Eq. 6-7 is performed numerically, with the distribution function being evaluated on the grid points (as discussed above) of the calibration data of the entrance system.

$$A_{eff}\left(v_b, v_{therm}, \alpha, \beta, V_{WAVE}\right) = \sum_k \sum_l \sum_m A\left(k_{WAVE,k}, \alpha_l, \beta_m\right) \frac{f_{SW}\left(v_k, \alpha_l, \beta_m\right)}{n_i} v_k^2 \Delta v \Delta\alpha \cos\beta \Delta\beta \qquad \text{Eq. 6-8}$$

with the normalization

$$1 = \sum_k \sum_l \sum_m \frac{f_{SW}\left(v_k, v_b, \alpha_l, \beta_m, v_{therm}\right)}{n_i} v_k^2 \Delta v \Delta\alpha \cos\beta_m \Delta\beta$$

Using the parameters v_b, v_{therm}, β_b and α_b , we get for every measurement interval of five minutes the effective area of the entrance system for the element of interest. The active area derived from Eq. 6-8 is shown in Figure 6-2 for O^{6+} ions and a relatively cold solar wind of 10 km/s thermal velocity. Actually, plotting the effective area against the instrument constant, $(E/Q)/V_{WAVE}$, makes the interpretation of Figure 6-2 independent of the choice of the ion. The effect of the thermal velocity is to smooth the calibration data due to the convolution. Typical solar wind will be much hotter (roughly in the range from 20 km/s to 100 km/s), which will smear out the wiggles in the effective area even more. Note that there is no interpolation performed between the grid points of calibration data. From the calibration against CTOF measurements (see Chapter 7.4) we learned that the effective area given by Eq. 6-8 (and also the calibration data) for $(E/Q)/V_{WAVE} \geq 1.1$ is too small. This is particularly a problem for heavy ions entering at high velocities.

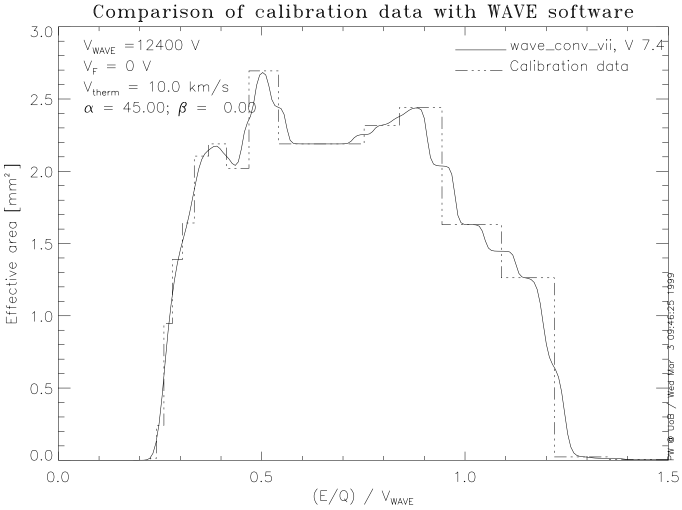

Figure 6-2: Effective area of the WAVE entrance system obtained from Eq. 6-8 versus the analyzer constant. The calibration data is given for comparison.

High transparency grids were used to terminate the electric fields in the three boxes with the repelling potentials, which cause the WAVE entrance system response to deviate from an ideal ion-optical element. Through the individual cells of the three grids there are field penetrations into the other boxes and the outside. During calibration of the WAVE entrance system it was found that these field penetrations cause an incoming pencil beam to diverge at the exit of the WAVE by

$$\Delta\alpha_{WAVE} = 2.0 \frac{V_{WAVE}}{E/Q} \left[\deg\ HWHM\right]$$

$$\Delta\beta_{WAVE} = 3.0 \frac{V_{WAVE}}{E/Q} \left[\deg\ HWHM\right] \qquad \text{Eq. 6-9}$$

Eq. 6-9 was established by calibration of WAVE. This beam divergence has to be considered in the further calculation of the total instrument function.

6.2 The Interface Between WAVE and V-MASS

For ions travelling from the WAVE exit to the V-MASS entrance (the carbon foil) two effects have to be considered. The ion trajectories will be bent either toward or away from the V-MASS entrance depending on whether the potential difference between WAVE exit and V-MASS entrance, V_F, is negative or positive, respectively. Furthermore, the ions are focused onto the carbon foil upon acceleration (negative V_F) or defocused upon deceleration (positive V_F). This affects the ion-optical transmission of this interface dramatically.

6.2.1 Ion-Optical Bending between WAVE and V-MASS

The exit angle of the ions after passing the WAVE entrance system is a function of the incoming angle α_b and the ion-optical settings of WAVE. From the WAVE calibration we get for the exit angle

$$\alpha_{exit} = -10.5 + 9.39 \cdot \left(\frac{E/Q}{V_{WAVE}} \right) + \alpha_b \cdot \left(1.197 - 0.0861 \frac{E/Q}{V_{WAVE}} \right) \qquad \text{Eq. 6-10}$$

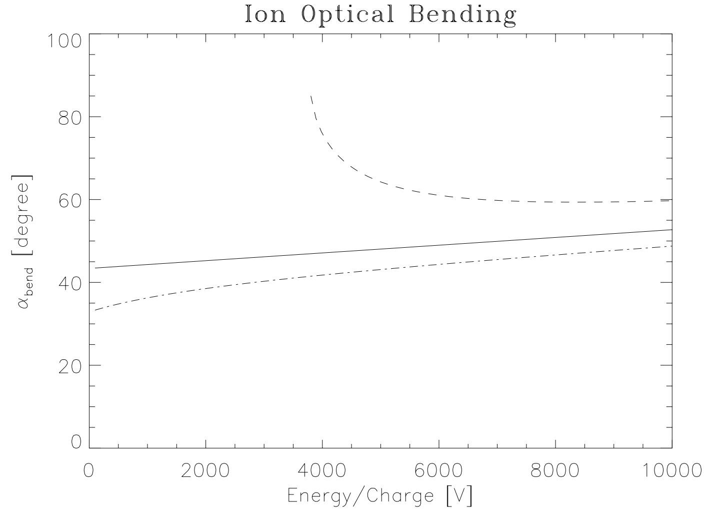

Figure 6-3: Ion-optical bending of the ion trajectories for positive (dashed line), zero (solid line), and negative (dash-pointed line) values of V_F (2500 V, 0 V, and –2500 V, respectively).

with α_{exit} measured in degrees, and E/Q and V_{WAVE} measured in volts. The interface between WAVE and V-MASS is complicated by the voltage difference, V_F, between the exit of WAVE, which is on ground potential, and the V-MASS entrance. The purpose of V_F, the floating voltage, is to adjust the energy of the ions before they enter the V-MASS so that they fall into the energy range which can be handled by V-MASS. Depending on the polarity of V_F, the ions are either accelerated or decelerated. Typical values for V_F are in the range between –3000 V and +3000 V. Not only is the effect of V_F to accelerate and decelerate the ions, but the ion trajectories are also bent toward or away from the entrance of V-MASS by this potential. From the calibration using the WAVE entrance system mounted in the V-MASS mock-up it was found that

$$\alpha_{bend} = \arctan\left(\sqrt{\frac{E/Q \sin(\alpha_{exit})^2 - V_F\, C_{bend}}{E/Q \cos(\alpha_{exit})^2 - V_F\,(1 - C_{bend})}} \right) \qquad \text{Eq. 6-11}$$

with $C_{bend} = 0.2947$, α_{exit} and α_{bend} measured in radians, and E/Q and V_F measured in volts. In the numerical calculation, Eq. 6-11 is applied only if V_F is not zero; otherwise $\alpha_{bend} = \alpha_{exit}$. In the limit of large E/Q values with respect to V_F the action of V_F on the ions is small, such that $\alpha_{bend} \approx \alpha_{exit}$. The bending of the ion trajectories is shown in Figure 6-3 for three different settings (decelerating, zero, and accelerating) of V_F. For zero potential difference or acceleration of the ions, the effect on the entrance angle in V-MASS is small. For the decelerating case, however, slower particles are deflected away from the V-MASS entrance and are lost for analysis if their energy is too low ($E/Q < V_F/2$).

Since the coordinate system of V-MASS is different from the WAVE coordinate system we have to use

$$\alpha_{in} = 90° - \alpha_{bend} \qquad \text{Eq. 6-12}$$

with the α's measured in degrees again. The angle β_b is not changed by the WAVE entrance system. Furthermore, it is assumed that β_b is not affected by V_F due to the symmetry of the ion optics with respect to β. Thus for the data analysis we use $\beta_{in} = \beta_b$.

6.2.2 Ion-Optical Transmission between WAVE and V-MASS

Not only is the angle with which the ions enter the V-MASS a function of the ion-optical interface between WAVE and V-MASS, but the ion-optical transmission is as well. Depending on the ion trajectories in the interface region and the angle the ions have at the location of the carbon foil, only a fraction of the ions actually hit the carbon foil. First of all, there is a dependence of the ion-optical transmission on α_b. The distribution of ions at the entrance of V-MASS overlaps with the entrance area only partially, depending on the angle with which the ions leave WAVE and arrive at the V-MASS entrance (see Eq. 6-11). This effect on the ion-optical transmission was measured during calibration of MTOF at the CASYMS calibration facility with a 2.5 keV $^4He^+$ beam and is given for the full range of α_b in Table 6-1.

Table 6-1: Relative ion-optical transmission between WAVE and V-MASS as derived from calibration of MTOF with a 2.5 keV $^4He^+$ ion beam in the CASYMS facility.

α_b [degrees]	correction
25	1.000000
30	0.990698
35	0.979308
40	0.965738
45	0.950091
50	0.933011
55	0.916545
60	0.906346
65	0.828403
70	0.660992

A strong effect on the ion-optical transmission between WAVE and V-MASS arises of course from a non-zero floating potential applied on the Vee with respect to the exit of the WAVE entrance system. This potential either focuses or defocuses the ions on their trajectory from the WAVE exit to the carbon foil of the V-MASS entrance. The effect of a non-zero floating potential on the ion-optical transmission was also measured with the MTOF mock-up in the CASYMS calibration facility. First we define a common factor for both cases (accelerating and decelerating potential):

$$C_{float} = a_5 + a_1\alpha_{exit} + a_2\alpha_{exit}^2 + a_4\frac{V_{WAVE}}{E/Q} \qquad \text{Eq. 6-13}$$

α_{exit} is measured in degrees, and E/Q and V_{WAVE} are measured in volts. C_{float} is a unit-less constant. The empirical constants used in Eq. 6-13 and further below are derived from calibration and are given in Table 6-2. For the accelerating situation ($V_F < 0$) we get

$$C_{corr} = C_{float}\left(\frac{V_F}{E/Q}\exp\left(-a_3\frac{V_F}{E/Q}\right) + a_6\cdot\left(1-\exp\left(-a_3\frac{V_F}{E/Q}\right)\right)\right) \qquad \text{Eq. 6-14}$$

Table 6-2: Values for the empirical constants used in Eq. 6-13 through Eq. 6-15 for the effect of the floating voltage on the ion-optical transmission between WAVE and V-MASS.

constant	value
a_1	0.66795497604
a_2	–0.01041849995
a_3	–0.07179500777
a_4	–0.03255499614
a_5	–11.62339862468
a_6	11.39569944350

with E/Q and V_F measured in volts. C_{corr} is also a unit-less constant. If $\frac{V_F}{E/Q} < C_{limit}$ with $C_{limit} = \frac{1 + a_3 a_6}{a_3}$ then C_{limit} is used instead of $\frac{V_F}{E/Q}$ in Eq. 6-14 for both exponents since the ion-optical transmission cannot exceed a certain maximum value no matter how low the ion energy is. For the decelerating situation ($V_F > 0$) we get a more complicated expression

$$C_{corr} = C_{float} \frac{V_F}{E/Q} \left(1 + a_3 a_6 \exp\left(1 - \frac{V_F}{\cos(\alpha_b)^2 E/Q} \right) \right) - \left(\frac{V_F}{\cos(\alpha_b)^2 E/Q} \right)^2 \exp\left(\left(2 + C_{float}\right) \left(1 - \frac{V_F}{\cos(\alpha_b)^2 E/Q} \right) \right) \qquad \text{Eq. 6-15}$$

Eq. 6-15 applies only if $\cos(\alpha_b)^2 > \frac{V_F}{E/Q}$; otherwise we have $C_{corr} = -1$ (which results in an actual effective area $\tilde{A}_{eff} = 0$, see below). Finally, for the effective area of the entrance system we get

$$\tilde{A}_{eff} = A_{eff} \cdot \left(1 + C_{corr}\right)$$

$\tilde{A}_{eff}$ is the effective area of the MTOF sensor seen from the entrance of the V-MASS, including the interface between WAVE and V-MASS. The effective area $\tilde{A}_{eff}$ is shown in Figure 6-4 as a function of V_F for O^{6+} ions entering at about 800 km/s for a WAVE setting of $V_{WAVE} = 12400\,V$. Acceleration of ions exiting the WAVE entrance system into the V-MASS spectrometer (negative values of V_F) results in a larger effective area due to focussing of the ion trajectories toward the C-foil. Similarly, deceleration of the ions (positive values of V_F) results in defocusing of the ion trajectories, but with a much stronger effect on the effective area $\tilde{A}_{eff}$.

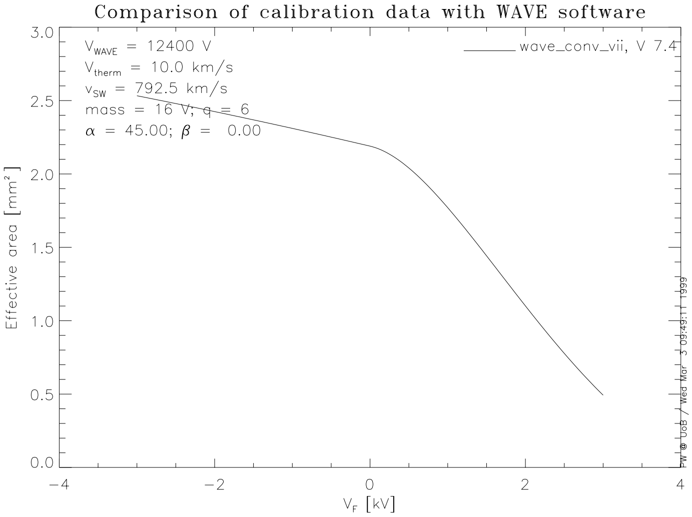

Figure 6-4: Effective area of the WAVE entrance system, including the interface to V-MASS versus V_F.

6.3 The V-MASS Instrument Function

The theoretical aspects of the functioning of the V-MASS TOF mass spectrometer have already been discussed in Chapter 5. In order to model the response of the V-MASS one needs to incorporate the actual realization of the instrument and to assess the ion-optical transmission for the relevant parameter space. In addition, the response of the carbon-foil (C-foil)—i.e., angular and energy scattering, the energy loss, the secondary electron production, and the charge state of the particle after the passage of the C-foil—have to be calculated and folded together to obtain the detection efficiency of the V-MASS. In this chapter we will calculate the scattering distribution after the C-foil and the ion-optical transmission of V-MASS in the three-dimensional parameter space (E, α, β). The convolution of these two distributions gives the total transmission of V-MASS, the final result of this chapter.

The instrument function has only been developed for the ion channel and not for the neutral channel (although that channel is considerably simpler), since only the ion channel offers such a richness of new data compared to previous instrumentation for solar wind. The neutral channel is basically a linear time-of-flight sensor with moderate, if any, post-acceleration potential, which results in a mass resolution less than the typical linear TOF instruments (SWICS-type sensors [93]). The neutral channel was not operational during the beginning of the mission because of a problem in the DPU software in assigning the proper telemetry quota to this data set. This DPU problem was fixed later, and the data from the neutral channel could be used for data analysis, possibly even for the determination of the α_{VM} angle[3].

6.3.1 Angular and Energy Scattering in the Carbon Foil

In the energy range of interest for V-MASS, particles passing through a carbon foil scatter in angle and energy considerably, two phenomena, which have to be included in the data evaluation in considerable detail. Since the angular scatter and energy scatter of particles passing a C-foil cannot be separated by V-MASS, these two phenomena will be studied here together.

Not considering an energy dependence of the angular scatter, the angular scatter distribution can be written as

$$f_\vartheta = \left(1 + \frac{\vartheta^2}{4\sigma^2}\right)^{-2} . \qquad \text{Eq. 6-16}$$

f_ϑ was found by fitting various functions to measured data [114]. For σ we use the expression given in the thesis papers by Oetliker and by Gonin [19; 114]

$$\sigma = a Z_1^b s^c \overline{E}^d \qquad \text{Eq. 6-17}$$

which gives σ in degrees and is an improved version of the function given in [115; 116]. Z_1 is the atomic number of the projectile and s is the thickness of the C-foil in [µg/cm^2]. The constants in Eq. 6-17 are $a = 13.642$, $b = 0.7455$, $c = 0.6748$, and $d = -0.9002$. $\overline{E}$ is the mean energy of a particle while passing through the C-foil, which is calculated from

$$\overline{E} = \frac{E_0 + E_f}{2} = E_0 - \frac{\Delta E}{2}$$

with E_0 the incident energy of the particle, E_f the mean final energy of the particle, and ΔE the mean energy loss in the C-foil, which is calculated using TRIM [117]. From Eq. 6-17 we see that the angular scatter depends only on the atomic number of the projectile but not on its mass. Hence it is the same for all the isotopes of an element, except for the energy loss ΔE, which is different for the isotopes and results in a small correction. In scatter theory the angular distribution is found to be a function of the atomic number as well but not of the mass of the projectile [118]. This theory was found to agree with experimental data very well [116]. Furthermore, the angular scatter distribution was found to be independent if the initial charge state of the ion [119]. This is important since with MTOF we do not measure the charge state of the

---

[3] F.M. Ipavich, private communication, 1998.

incoming ion. However, the angular scatter distribution plays an important role in the instrument function. The half width at half maximum (HWHM) of the distribution is related to σ (Eq. 6-17) by

$$\vartheta_{HWHM} = 2\sigma\sqrt{\sqrt{2}-1}\ . \qquad \text{Eq. 6-18}$$

Since there is also an angular spread of the ions when they leave WAVE, $\Delta\alpha_{WAVE}$, this contribution has to be added to

$$\tilde{\vartheta}_{HWHM} = \sqrt{\vartheta_{HWHM}^2 + \Delta\alpha_{WAVE}^2}$$

For particles entering the C-foil perpendicularly, the angular distribution at the exit of the C-foil will peak at the surface normal. If the entrance angle is less than perpendicular, the peak of the angular distribution at the exit will then be shifted from the initial direction toward the surface normal by a certain amount. For a 45° incident angle it was found by fitting scatter distributions to experimental data [19] that the bending of the trajectory in the C-foil toward the surface normal is

$$\Delta\alpha_{refract} = a\cdot\left(\frac{E_0}{m}\right)^b \qquad \text{Eq. 6-19}$$

with E_0 the incident energy of the particle in [keV], m the mass in [amu], $a = 2.1027$, and $b = 1.67$ for a C-foil of thickness 2.2 µg/cm^2. Neither in the thesis work of Gonin [19] nor in earlier work is a foil-thickness dependence included. Based on theoretical considerations we can generalize Eq. 6-19 for other foil thicknesses

$$\Delta\alpha_{refract} = a\cdot\left(\frac{E_0}{m}\right)^b\sqrt{\frac{s}{2.2}}$$

with s being the thickness of the C-foil in [µg/cm^2]. Fortunately, the C-foil used in MTOF is nominally 2.2 µg/cm^2, and from calibration it turns out that this value is most probably 2.1 µg/cm^2. Due to the action of V_F, the nominal entrance angle of 45° into V-MASS can be changed quite substantially, which has to be accounted for. In the absence of any further information on this subject, we linearly extrapolate for other angles in the following way:

$$\Delta\alpha_{\alpha,refract} = \Delta\alpha_{refract}\cdot\left(2-\frac{\alpha_{bend}}{45°}\right)$$

Because in the coordinate system of V-MASS we measure the angle with respect to the surface plane, we get

$$\alpha_{VM} = \alpha_{in} + \Delta\alpha_{\alpha,refract} \qquad \text{Eq. 6-20}$$

for the mean angle after the C-foil in the V-MASS unit.

After this introduction we need to look into the scattering distributions in more detail. Few experimental and theoretical data are available on this subject, but it is established that the average energy loss increases for larger scattering angles [116; 120]. Most of the following is based on TRIM simulations [117], which have been performed for all elements (and their isotopes) found in the solar wind for the entire energy range covered by V-MASS.

The average energy at a certain scattering angle, $E_{f,\alpha}$, can be described by a Gaussian distribution

$$E_{f,\alpha} = \left(E_0 - \Delta E_{45}\right)\exp\left(-\frac{1}{2}\frac{\left(\alpha-\alpha_{VM}\right)^2}{\sigma_E^2}\right) \qquad \text{Eq. 6-21}$$

with ΔE_{45} the average energy loss for a particle entering the C-foil at 45°, as calculated with TRIM for each element over the full energy range of V-MASS. The width of the distribution is given by

$$\sigma_E = \tilde{\vartheta}_{HWHM} \cdot \left(1.122\frac{E_0}{m} + 0.064\right)$$

with E_0 the incident energy in [keV], *m* the mass in [amu], and the numerical constants derived from fits to TRIM simulations. Again, also for the energy loss it was found that there is no dependence on the initial charge state of the ion for the range of charge states of interest for us [119]. Only when the initial charge state exceeds about 30 charges does the energy loss increase with charge state measurably upon transition through a 2 µg/cm^2 carbon foil [121]. Such high charge states are not observed for solar wind ions. Typically, the charge state of heavy ions is around +10; during transient events higher charged ions like Si^{12+} and Fe^{16+} are observed occasionally.

$E_{f,\alpha}$ describes the ridge of the scatter distribution in the parameter plane (E, α). Along this ridge there is energy scatter as a function of scattering angle and incident energy

$$\sigma_{E,\alpha} = 0.2062\, E_{f,\alpha} \cdot \left(\frac{m}{E_0}\right)^{1.0803} + 0.3 \cdot \left(1 - \exp\left(-\frac{1}{2}\frac{\left(\alpha - \alpha_{VM}\right)^2}{\sigma_\alpha^2}\right)\right) \qquad \text{Eq. 6-22}$$

with the numerical constants again derived from the TRIM simulations. The width of the distribution in Eq. 6-22 is given by

$$\sigma_\alpha = \frac{1}{\sqrt{2\ln 2}}\left(11.42 + 0.7865\,\tilde{\vartheta}_{HWHM} - 0.00801\,\tilde{\vartheta}_{HWHM}^2\right)$$

In addition to the scattering occurring in the carbon foil, we have to consider the variations in thickness of the C-foil, σ_{foil}, as well as the energy width of the ion beam entering the C-foil, σ_E, both of them modify Eq. 6-22 as follows:

$$\tilde{\sigma}_{E,\alpha} = \sqrt{\sigma_{E,\alpha}^2 + \sigma_{foil}^2 + \sigma_E^2}$$

The few experimental reports on scatter distributions along the energy axis show that these distributions are highly asymmetric [106; 116; 122-124]. For energies larger than the mean energy $E_{f,\alpha}$ the distribution can be described by a Gaussian profile; for energies less than the mean energy $E_{f,\alpha}$ the distribution is much broader and tailed toward low energies, and can be described by a squared Lorentzian profile. Thus we write

$$f_E = \begin{cases} \exp\left(-\frac{1}{2}\frac{\left(E - E_{f,\alpha}\right)^2}{\tilde{\sigma}_{E,\alpha}^2}\right) & E > E_{f,\alpha} \\ \left(1 + \frac{\left(E - E_{f,\alpha}\right)^2}{2 \cdot 1.29\,\tilde{\sigma}_{E,\alpha}^2}\right)^{-1} & E \le E_{f,\alpha} \end{cases} \qquad \text{Eq. 6-23}$$

The prefactor to the scatter width in the squared Lorentzian distribution has been derived by reproducing the measured energy distributions [106; 116; 122-124] with Eq. 6-23.

The angular dependence of the angular scatter is described by a squared Lorentzian distribution

$$f_\alpha = \left(1 + \frac{\left(\alpha - \alpha_{VM}\right)^2}{\sigma_{\vartheta,\alpha}^2}\right)^{-2} \qquad \text{Eq. 6-24}$$

The width of the distribution is given by

$$\sigma_{\vartheta,\alpha} = 1.163\frac{\tilde{\vartheta}_{HWHM}}{2\sqrt{\sqrt{2} - 1}} \qquad \text{Eq. 6-25}$$

The energy and angular distribution after the C-foil can be put together to obtain the total distribution of scattered particles in α-E space

$$f_{C-foil}(\alpha,E)=\frac{f_\alpha \circ f_E}{\iint f_\alpha \circ f_E \, d\alpha \, dE} \qquad \text{Eq. 6-26}$$

which is a function of exit energy and exit angle. In Figure 6-5 this function is shown for oxygen entering a C-foil of 2.1 µg/cm^2 thickness with 30 keV kinetic energy. The dashed-pointed line plotted over the contour lines gives the angle-dependent energy loss (as given by Eq. 6-21). The energy loss is a strong function of the exit angle, which is in good agreement with experimental data reported by Beauchemin *et al.* [120]. This angle-dependent energy loss results in a distribution, which fingers out to the sides for large scattering angles. The distribution peaks at a somewhat larger angle α than the nominal 45° of the incoming particles due to the refraction of particles in the C-foil (see Eq. 6-19). The distribution of scattered particles would extend to higher energies than the primary energy since we used a Gaussian distribution. This is corrected by a sharp cut-off in f_{C-foil} for energies beyond E_0. The error from this sharp cut-off is considered negligible.

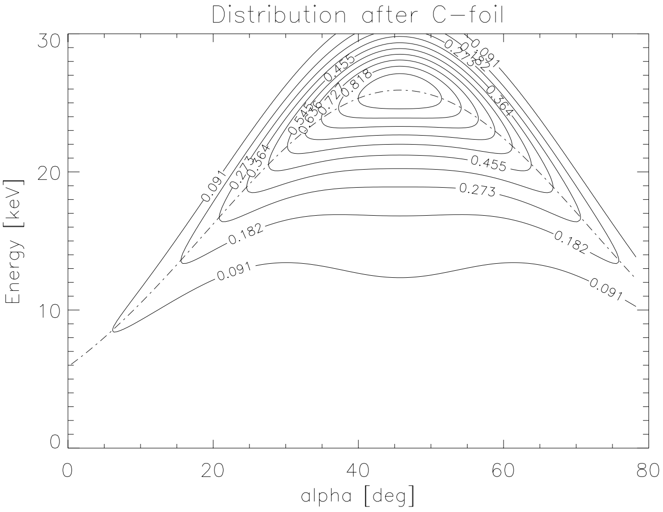

Figure 6-5: Angular and energy scattering distribution after a 2.1 µg/cm^2 C-foil for oxygen entering at an energy of 30 keV. Ten linearly spaced contours are given; the function is scaled to 1. The dashed-pointed line gives the angle-dependent mean energy from Eq. 6-21.

Unfortunately, we cannot directly compare f_{C-foil} with experimental data, since these data are not available. However, we can derive integrals over energy or angle from f_{C-foil}, or we can derive cuts through f_{C-foil}, and these can be compared to published experimental results.

One test, which can be applied to the total scatter distribution, is to integrate over all energies and thus reduce the total distribution to an angular distribution. This angular distribution should then reproduce the angular scattering data reported in [19]. In Figure 6-6 such a comparison is shown, again for 30 keV oxygen entering a C-foil of 2.1 µg/cm^2 thickness. The data in Figure 6-6 are obtained by integrating the data given in Figure 6-5 over energy, and are displayed as the solid curve. For comparison with experimental data [19], a squared Lorentzian (the found distribution function, Eq. 6-16) with the σ of the distribution calculated from Eq. 6-17 is shown by a

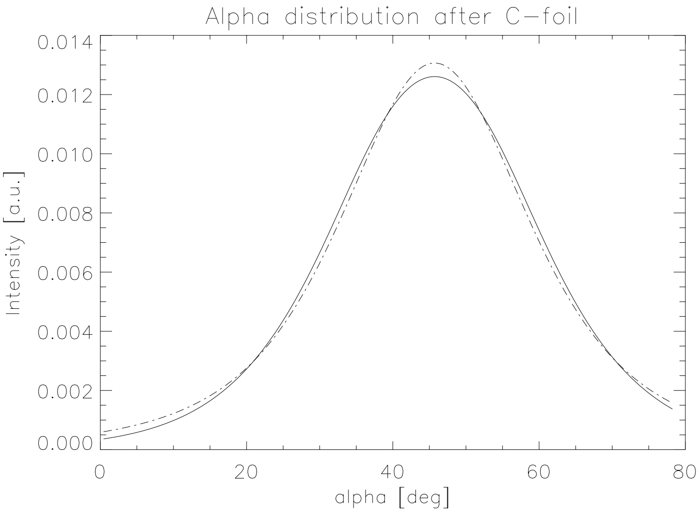

Figure 6-6: Comparison of the calculated angular distribution and a distribution derived from measured data for 30 keV oxygen entering a 2.1 µg/cm^2 C-foil. The solid line gives the integral over energy of the total distribution (from Eq. 6-26), the dashed-pointed line gives the experimental angular distribution (Eq. 6-16) with the σ derived from Eq. 6-17 [19].

dashed-pointed line. The two curves agree reasonably well. This comparison was also used to determine the pre-factor in Eq. 6-25. The small differences between the two angular distributions are not significant, since f_{C-foil} will be convoluted with the ion-optical acceptance of V-MASS (see Chapter 6.3.3). Moreover, the squared Lorentzian is also a simplification of different angular distributions observed in the experiment.

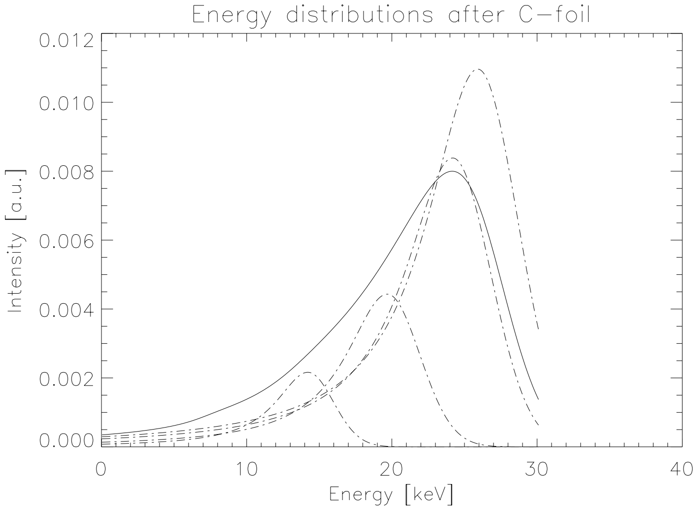

Figure 6-7: Cuts through the total distribution function as given in Figure 6-5 along the exit angles of 45°, 35°, 25°, and 15° (dashed-pointed lines, from left to right). In addition, the integral over the exit angle is shown (solid line), but is not to scale with the angular cuts.

Another test of the total distribution function is to integrate over angle and then investigate cuts through the total distribution function along a certain exit angle to compare with available experimental data. These investigations are shown in Figure 6-7, again for 30 keV oxygen entering a 2.1 µg/cm^2 C-foil at a 45° incident angle. One clearly sees that the average energy loss is increasing dramatically with scattering angle, which is in good agreement with energy distributions for different exit angles reported in [116]. The integral over exit angle of the total distribution function is also shown in Figure 6-7, which exhibits a considerable asymmetry along the energy axis. This is caused by the angle-dependent energy loss.

6.3.2 Charge Exchange in the Carbon Foil

When particles (ions, neutral atoms) pass through a carbon foil they undergo charge exchange processes with the medium, and their final charge—or rather the charge state distribution—is determined by the medium and the projectile's energy only. Early studies on this subject date back to the late 1960's and early 1970's [124-126], but these studies used particle energies at least one order of magnitude too high for our application. Recently, the charge exchange was studied experimentally in detail at the University of Bern [16; 17; 19; 114] to assist in the analysis of MTOF data. A charge transfer model was developed to explain and interpolate the experimental data for all elements occurring in the solar wind [18; 94], with the free parameters in this model fitted to the experimental data. The model and its parameterization have been implemented in the MTOF analysis software. However, it turned out during the analysis that the fits obtained with the charge transfer model were not accurate enough in the energy range

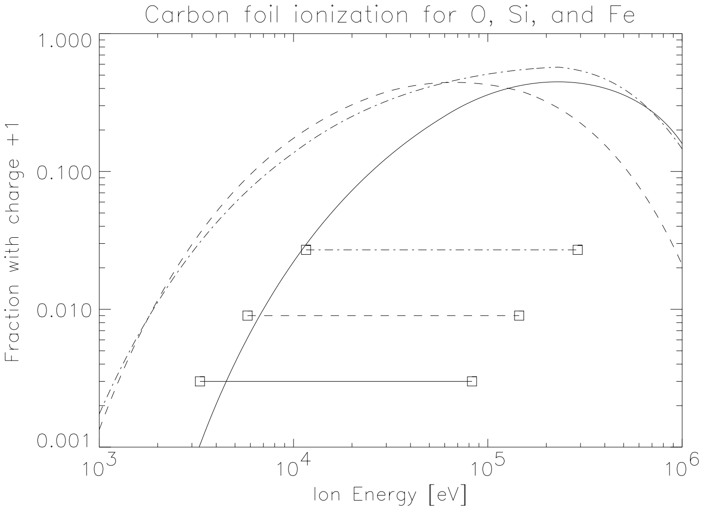

Figure 6-8: Ionization efficiencies for O (solid line), Si (dashed line), and Fe (dashed-pointed line) singly charged ions are shown for a C-foil of 2.1 µg/cm^2 thickness and an impact angle of 45°. Horizontal bars indicate a solar wind velocity range from 200 km/s to 1000 km/s for the three ions.

applicable for MTOF. Simple quadratic fits to the measured ionization data yielded better results in the end. The ionization efficiency is a function of the residual energy of the ion after it passes the C-foil E_{final}, as well as a function of species Z_1 and of the foil thickness *s* [18]

$$\eta_{ion} = f(E_{final}, Z_1, s).$$

η_{ion} is evaluated for the whole energy scatter distribution and convoluted with the ion optical transmission. The ionization efficiencies obtained from the implementation of the charge transfer model for O, Si, and Fe singly charged ions are shown in Figure 6-8 for a C-foil of 2.1 µg/cm^2 thickness and an impact angle of 45°. Also given in Figure 6-8 are the energy ranges for the three ions for a solar wind velocity range of 200 km/s to 1000 km/s. This energy range is shifted to the left or right depending on whether there is post-acceleration or deceleration by V_F. The ion-optical transmission of MTOF allows for ion energies up to 44 keV after the C-foil for the usual setting of V_{HYP} during flight (see Figure 6-11 below). The average charge equilibration length of a highly charged ion entering a C-foil was found to be around one carbon layer [119], even at energies higher than the ones used in MTOF. After that distance the particle has lost all the memory of its charge state before entering the C-foil. Thus we do not need to know the initial charge state of the ion for the calculation of the charge state distribution after the C-foil.

6.3.3 Secondary Electron Emission

The secondary electron production of the carbon foil surface upon passage of an ion is crucial for triggering the time-of-flight measurement. Secondary electrons are released from the carbon foil both at the entrance and the exit surface at the approximate place at which the particle trajectory intersects these surfaces. In the case of the MTOF sensor the secondary electrons emitted from the exit surface (back side) of the carbon foil are used for the timing of the TOF circuitry.

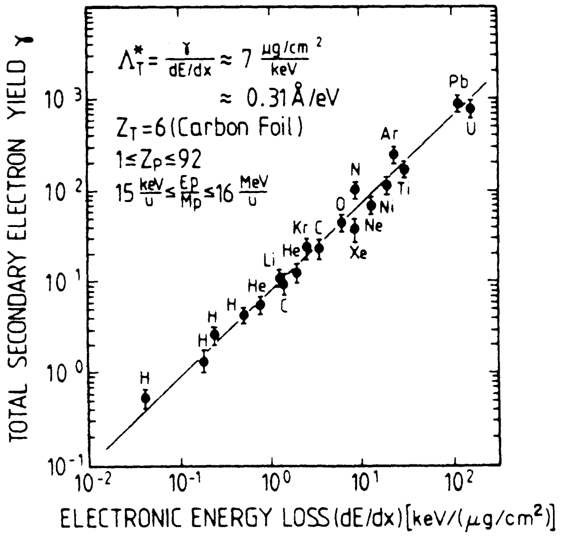

Figure 6-9: Total secondary electron yield from carbon foils as a function of the electronic energy loss *dE/dx* of the projectiles (from Rothard *et al.* [127]).

The theoretical understanding of the secondary electron emission has been reviewed recently by Schou [128]. Unfortunately, the theoretical understanding of secondary electron emission is not advanced enough to make reliable quantitative predictions on the yield of released electrons for the range of ions we are interested in. To first order, which is within a factor of two, the total secondary electron yield, γ (the average number of released electrons per incident ion), is proportional to the electronic stopping power of the particle in the solid [127]. Since this secondary electron emission is induced by an ion with appreciable kinetic energies it is called kinetic electron emission (KEE) in the literature. The proportionality between electronic energy loss and secondary electron emission is shown in Figure 6-9, and is valid for many elements and over a wide energy range. The mean value of the ratio of the secondary electron yield versus the electronic stopping power is

$$\Lambda = \frac{\gamma}{(dE/dx)_E} \approx 0.31 Å/eV. \qquad \text{Eq. 6-27}$$

The total secondary electron yield is the sum of the electrons released from the foil at the particle entrance, γ_{FRONT}, and at the particle exit, γ_{BACK}. The ratio of electrons released at the entrance to electrons released at the exit of the carbon foil is

$$R = \frac{\gamma_{BACK}}{\gamma_{FRONT}} = \begin{cases} R_0 + 0.759\log\left(E/m\right) & E/m \le 150\,keV/nuc \\ R_0 + 1.56 & E/m > 150\,keV/nuc \end{cases} \qquad \text{Eq. 6-28}$$

with $R_0 = -0.231$ for hydrogen, $R_0 = 0.069$ for helium, and $R_0 = 0.569$ for all heavier elements, and E/m measured in keV/nuc. Eq. 6-28 has been adapted from data reported by Meckbach *et al.* [129] and by Rothard *et al.* [127; 130]. R being larger than 1 means that the forward emission (at the exit surface) predominates. This is a little bit surprising, but indicates that the secondary electron emission is not just a surface phenomenon, but that some of the electronic excitation along the particle trajectory inside the solid follows the projectile to the exit surface to cause an increased secondary electron emission. At these energies, the favored forward emission is not caused by delta electrons or by wake field acceleration of electrons inside the solid. Thus we get for the secondary electron emission at each side of the carbon foil

$$\begin{aligned} \gamma_{FRONT} &= \Lambda \frac{1}{1+R}\left(\frac{dE}{dX}\right)_E \\ \gamma_{BACK} &= \Lambda \frac{R}{1+R}\left(\frac{dE}{dX}\right)_E \end{aligned} \qquad \text{Eq. 6-29}$$

The total secondary electron yield given by Eq. 6-27 is valid only for clean surfaces, that is when the removal of adsorbed atoms by sputtering greatly exceeds the rate of adsorption from the residual gas pressure. For "dirty" surfaces the secondary electron yield can even be an order of magnitude larger than for a clean surface [131; 132]. For carbon foils this effect is not that dramatic; the secondary electron yield drops by about 20% after the foil has been exposed to a fluence of $2\cdot10^{15}$ ions/cm^2 [133]. Most likely we will have the situation of a "dirty" C-foil, since the particle flux at the foil in the MTOF sensor is too small to achieve efficient cleaning by sputtering. This is of course desired, since we do not want to use up the C-foil during the mission.

Because Eq. 6-27 is only valid to the first order, we have to consider additional modifications to this formula to obtain the secondary electron emission with the required precision. There is a systematic deviation of the secondary electron yield from Eq. 6-27 depending on the element passing the foil and also on the target material. The latter is of no importance for us since we only use carbon foils. To account for the state of cleanliness of the surface of the carbon foil and the element dependence of the secondary electron emission we have to modify Eq. 6-29 by introducing an element-specific factor F_i [127; 134]

$$\begin{aligned} \gamma_{FRONT} &= \Lambda F_i \frac{1}{1+R}\left(\frac{dE}{dX}\right)_E \\ \gamma_{BACK} &= \Lambda F_i \frac{R}{1+R}\left(\frac{dE}{dX}\right)_E \end{aligned} \qquad \text{Eq. 6-30}$$

which has to be established during calibration of the sensor. There is also a dependence of the secondary electron yield on the foil thickness (particularly at the exit surface), with the Λ slowly increasing for thicker foils [135; 136].

In addition to kinetic electron emission there is also potential electron emission. When an ion approaches the surface, the potential energy released upon neutralization of the projectile can provide the energy required to free an electron from the solid [131]. For small projectile velocities the potential emission is given by

$$\gamma_{pot} = 0.032\cdot\left(0.78E_g - 2.0WF\right) \qquad \text{Eq. 6-31}$$

with E_g being the ground-state neutralization energy of the ion (the depth of the potential well of the ion) and *WF* the work function of the surface. For ion velocities larger than about 10^5 m/s the kinetic electron emission becomes more important than the potential emission. For singly charged ions the yield of secondary electrons is modest, but the yield is larger for higher ionization states of an ion since the ionization potential for these states is higher than for the first ionization. Since the secondary electron emission on the entrance side is not used in the MTOF sensor we will not go into more detail on this issue.

The energy loss of a particle with the energy *E* in matter is known relatively well from many experimental studies as well as from theoretical calculations (for example, see the review by Betz and Wien [137]), and can also be calculated with programs like TRIM [117] reasonably reliably. The total energy loss is given as follows:

$$\frac{dE}{dx} = \left.\frac{dE}{dx}\right|_N + \left.\frac{dE}{dx}\right|_E = f\left(E,...\right)$$

where the index *N* indicates the contribution by nuclear interaction of the projectile with the solid (nuclear stopping), and the index *E* indicates the energy loss by interaction of the projectile with the electron gas of the solid (electronic stopping). The function *f*(*E*, ..) is rather complex (see [137] and references therein), but mathematically speaking reasonably well behaved (for example, differentiable many times, bounded, ...). To assess the total energy loss during passage of a particle *ΔE* through the carbon foil of thickness *l* one needs to integrate

$$\Delta E = \int_0^l \left.\frac{dE}{dx}\right|_N + \left.\frac{dE}{dx}\right|_E dx = \int f\left(E(x),....\right)dx$$

which is complicated by the fact that the energy *E* is a function of x. A different way to solve this problem would be

$$\frac{dE}{dx} = f\left(E\right) \rightarrow \frac{dE}{f\left(E\right)} = dx$$

which can be integrated rather easily

$$g\left(\Delta E\right) = \int_E^{\Delta E} \frac{1}{f\left(E\right)} dE = \int_0^l dx = l$$

By inversion one obtains

$$g(\Delta E) = l \;\rightarrow\; \Delta E = \tilde{g}(l)$$

which yields an insurmountable transcendental equation for ΔE.

As a new approach to solving this mathematical problem we divide the carbon foil into small sections, as shown in Figure 6-10. The particle moves along the *x*-axis through *n* sections of length Δx, which add up to the total thickness of the carbon foil of *l*. For the energy at the entrance and exit of the carbon foil $E_{out} = E_n$ and $E_{in} = E_0$, one obtains in the simplest case ($n = 1$)

$$E_1 = E_0 - \frac{dE}{dx}\Delta x \qquad \text{Eq. 6-32}$$

The particle energies in the MTOF sensor are typically rather low (around a keV/nuc) so we have to consider higher-order terms for the approximation of the energy loss

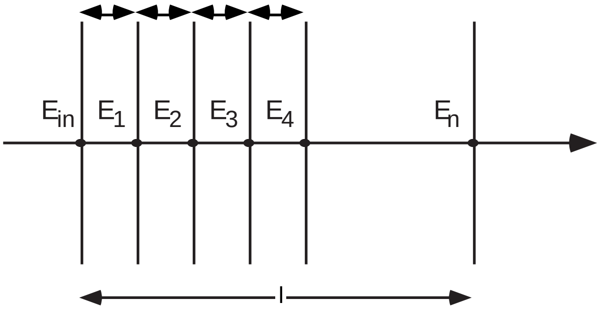

Figure 6-10: For solving the problem the carbon foil of length *l* is divided into *n* sections, each has a thickness of Δx. The particle moves along the *x*-axis, shown by the central arrow.

$$E_2 = E_0 - 2\frac{dE}{dx}\Delta x + \frac{d^2E}{dx^2}\Delta x^2 \qquad \text{Eq. 6-33}$$

$$E_3 = E_0 - 3\frac{dE}{dx}\Delta x + 3\frac{d^2E}{dx^2}\Delta x^2 - \frac{d^3E}{dx^3}\Delta x^3 \qquad \text{Eq. 6-34}$$

with $\Delta x = l/n$. For the application in MTOF the second-order approximation is considered sufficient and so far no indication is encountered during the data analysis which would demand higher-order terms. However, in order to continue an interesting mathematical thought one obtains after *n* steps

$$E_n = \sum_{k=0}^{n}(-1)^k \binom{n}{k}\left(\frac{l}{n}\right)^k \frac{d^kE}{dx^k} = \left(1 - \frac{l}{n}\frac{d}{dx}\right)^n E \qquad \text{Eq. 6-35}$$

Although the function dE/dx is mathematically speaking rather good-natured, the derivatives with increasing order become more and more involved, which limits the use of Eq. 6-35 for practical application. In the limit of $n \to \infty$ we get a formula which looks rather simple, but which might not be solved directly:

$$E_\infty = \lim_{n\to\infty}\left(1 - \frac{l}{n}\frac{d}{dx}\right)^n E = \exp\left(-l\frac{d}{dx}\right)E \qquad \text{Eq. 6-36}$$

To solve the above equation one has to go back one step and start from the expansion of the energy loss (Eq. 6-35)

$$\Delta E = E_n - E_0 = \sum_{k=1}^{n}(-1)^k \binom{n}{k}\left(\frac{l}{n}\right)^k \frac{d^k}{dx^k}E_0$$

by building the Fourier transform

$$\begin{aligned}\Im\left(E_n - E_0\right) &= \sum_{k=1}^{n}(-1)^k \binom{n}{k}\left(\frac{l}{n}\right)^k \Im\left(\frac{d^k}{dx^k}E_0\right)\\ &= \sum_{k=1}^{n}(-1)^k \binom{n}{k}\left(\frac{l}{n}\right)^k \left(i2\pi s\right)^{k-1}\Im\left(\frac{dE}{dx}\right)\end{aligned}$$

with the information of the physical system being contained in the function dE/dx. Now we proceed with

$$\begin{aligned}\Im\left(E_n - E_0\right) &= \frac{\Im\left(\frac{dE}{dx}\right)}{i2\pi s}\sum_{k=1}^{n}(-1)^k \binom{n}{k}\left(\frac{l}{n}\right)^k \left(i2\pi s\right)^k =\\ &= \frac{\Im\left(\frac{dE}{dx}\right)}{i2\pi s}\left(\sum_{k=0}^{n}(-1)^k \binom{n}{k}\left(\frac{l}{n}\right)^k \left(i2\pi s\right)^k - 1\right)\end{aligned}$$

which simplifies to

$$\Im\left(E_n - E_0\right) = \frac{\Im\left(\frac{dE}{dx}\right)}{i2\pi s}\left(\left(1 - i2\pi s\frac{l}{n}\right)^n - 1\right)$$

In the limit of $n \to \infty$ we get

$$\Im\left(E_\infty - E_0\right) = \lim_{n\to\infty}\left\{\frac{\Im\left(\frac{dE}{dx}\right)}{i2\pi s}\left(\left(1 - i2\pi s\frac{l}{n}\right)^n - 1\right)\right\} =$$

$$= \frac{\Im\left(\frac{dE}{dx}\right)}{i2\pi s}\left(\lim_{n\to\infty}\left(1 - i2\pi s\frac{l}{n}\right)^n - 1\right) =$$

$$= \frac{\Im\left(\frac{dE}{dx}\right)}{i2\pi s}\left(e^{-i2\pi sl} - 1\right)$$

Upon Fourier transformation back into real space we obtain

$$\Delta E = E_0 - E_\infty = -\Im^{-1}\left\{\Im\left(\frac{dE}{dx}\right)\cdot\frac{e^{-i2\pi sl} - 1}{i2\pi s}\right\} \qquad \text{Eq. 6-37}$$

Actually, Eq. 6-37 is just the convolution of the energy loss dE/dx with a medium extending from $x = 0$ to $x = l$, using the convolution law for Fourier transformations. The second term in Eq. 6-37 is the Fourier transform of a box of unit height in the interval from $x = 0$ to $x = l$ and zero elsewhere.

For the secondary electron emission at the side of the entrance of the ions (the front side) we get

$$\gamma_{FRONT} = \Lambda F_i \frac{1}{1+R}\cdot\left(\frac{dE}{dx}\right)_E + \gamma_{pot} \text{ at } E = E_0 \qquad \text{Eq. 6-38}$$

with R being the ratio of electrons emitted at the entrance and exit side of the foil and γ_{pot} the secondary electrons emitted due to potential emission.

So far we have calculated the total and electronic energy loss of a particle at the entrance and exit surface. However, there is energy scattering in the total energy loss upon passage of a particle through matter caused by the nuclear interactions between projectile and foil. Therefore we have to fold the energy scattering around the exit energy E_2 into our derivation of the secondary electron yield at the exit surface. We can approximate the energy scattering [106; 107] by a distribution, f_{SC}, with a half-width of

$$\Delta E_{scattter} = 2.55\sqrt{E\,s\,m} \quad [eV] \qquad \text{Eq. 6-39}$$

with E being the energy at the exit of the carbon foil ($E = E_2$), s the foil thickness in [µg/cm^2], and m the mass of the projectile in [amu]. We either use a Gaussian or a Lorentzian distribution for this convolution, depending on whether the actual energy is larger or smaller than E_2 (similar to Eq. 6-23). At the side where the ions exit (the back side) we get for the secondary electron yield

$$\gamma_{BACK} = \Lambda F_i \frac{R}{1+R}\frac{\int\left(dE/dx\right)_E f_{SC}\left(E, E_2, E_{scatter}\right)dE}{\int f_{SC}\left(E, E_2, \Delta E_{scatter}\right)dE} \qquad \text{Eq. 6-40}$$

The potential emission is not considered in Eq. 6-40 because at the low energies at which the potential emission could contribute noticeably to the total electron yield the particles exiting the C-foil are mostly neutral and therefore cannot pull out an electron from the surface (see Eq. 6-31).

The start efficiency is derived from the secondary electron emission at the back side of the C-foil as

$$\eta_{START} = 1 - e^{-p_{ele}\gamma_{back}} \qquad \text{Eq. 6-41}$$

with $p_{ele} = 0.667$, the detection efficiency of the start MCP assembly for single electrons in saturated mode. This value has been determined from calibration, and basically represents the fraction of open area of a MCP. It was found earlier for channel electron multipliers (same electron amplifying material) that the detection efficiency saturates once the electrons have energies in excess of 100 eV [138-140]. Since channel electron multipliers have an unobscured entrance the saturation value for their efficiency is around one.

6.3.4 The Stop Efficiency

Little is known about the stop efficiency—i.e., the efficiency of the ion MCP assembly to register an ion—from calibration. Either these data are not available or they are not yet analyzed. For this study we consider only geometrical effects for the stop efficiency and assume that the MCP is operated in saturated mode. The stop efficiency is obtained by convoluting the angular distribution of ions after the C-foil (Eq. 6-24) with the angular dependent efficiency of a MCP [141; 142]. This angular dependence is described here by a cosine function, which is a reasonable simplification of the actual behavior. Thus for the stop efficiency we get

$$\eta_{STOP} = p_{ion} \frac{\int \cos\left(90° - \alpha_{VM}\right) f_\alpha d\alpha}{\int f_\alpha d\alpha} \qquad \text{Eq. 6-42}$$

with $p_{ion} = 0.6$, the detection efficiency of the ion MCP assembly for ions in saturated mode considering a grid in front of the ion MCP with a transmission of 95%. Also, the detection efficiency for ions saturates once the ions have energies in excess of a few keV, as was found for MCPs [142; 143] as well as for channel electron multipliers [144]. Solar wind ions typically have energies of 1 keV/nuc (corresponding to a solar wind velocity of 440 km/s), which gives for carbon, the lightest of the ions of interest, already a typical energy of 12 keV. Eq. 6-42 typically gives a value of about 0.3 for the stop efficiency for most of the conditions encountered. Note that no species dependence is included in Eq. 6-42, since this information is not available from calibration. However, a significant species dependence is not expected given what is known from literature.

6.3.5 The V-MASS Ion-Optical Transmission

The ion-optical transmission of V-MASS was determined by a Monte-Carlo simulation. Ion trajectories were started at various locations on the C-foil, with various incoming angles α and β, and also with various initial energies of the ions inside the V-MASS unit. The values of these variables were given by the Monte-Carlo method. See Figure 5-2 for the definition of the geometry. The trajectories were calculated for each ion with their individual starting conditions. From these simulations we find that the ion-optical transmissions can be described by a Gaussian distribution of the form

$$T_{\alpha,E} = \exp\left(-\frac{1}{2}\left(\frac{U - 0.203}{0.06824}\right)^2\right) \qquad \text{Eq. 6-43}$$

with numerical constants fitted to the result of the Monte-Carlo simulation. The argument U in Eq. 6-43 is

$$U = \frac{1}{78.3° - \alpha_{VM}}\left(\frac{V_{HYP}}{30.0kV}\frac{1}{E}\right)^{0.3} \qquad \text{Eq. 6-44}$$

Equations 6-43 and 6-44 reproduce the energy and angle dependence of the V-MASS transmission. All the Monte-Carlo simulations have been performed for a hyperbola voltage (V_{HYP}) of 30 kV. The transmission for other hyperbola voltages is obtained by scaling to the 30 kV. A shallower starting angle of the ion trajectory (smaller α_{VM}) results in a smaller transmission. The higher the energy, the larger the defocusing effect of the hyperbola on the ion trajectory, and the lower the chance of hitting the detector. In addition to the ion-optical transmission function there are geometrical limitations for the ion transmission. In the direction toward the Vee we have to have

$$\begin{aligned} E_z &< \tilde{q}\, V_{HYP} \\ E_z &> 0.00167\, \tilde{q}\; V_{HYP} \end{aligned} \qquad \text{Eq. 6-45}$$

for successful ion detection. Otherwise, the ion hits the hyperbola if the energy is too high or the gusset of the Vee if the energy is too low. $\tilde{q}$ is the charge of the ion of interest after passing the C-foil. In the direction along the Vee we have to have

$$\begin{aligned} E_x &< 1.1\tilde{q}\, V_{HYP} \\ E_x &> 0.05\tilde{q}\, V_{HYP} \end{aligned} \qquad \text{Eq. 6-46}$$

for successful ion detection. Otherwise, the ion overshoots the ion MCP if the energy is too high, or undershoots the ion MCP if the energy is too low. The ion-optical transmission has to be folded together with the scattering distribution after passing the C-foil

$$T_{ion-opt} = \tilde{T}_{\alpha,E} \otimes f_{C-foil} \qquad \text{Eq. 6-47}$$

with $\tilde{T}_{\alpha,E}$ being $T_{\alpha,E}$ as long as conditions in Eq. 6-45 and Eq. 6-46 are met; otherwise $\tilde{T}_{\alpha,E}$ is set to zero.

Putting all elements of the V-MASS transmission together, i.e., the start efficiency, the stop efficiency, the ionization probability and the V-MASS ion-optical transmission, we get the total V-MASS transmission. This transmission is shown in Figure 6-11 for a hyperbola voltage of 20.7 kV, which is the level used most frequently during the mission. The limitations on the ion-optical transmission given by geometrical considerations (Eqs. 6-45 and 6-46) are indicated in Figure 6-11. The total V-MASS transmission is a strong function of α and E. Particles with the largest energies can be detected only for an angle after the C-foil of about 45°, which was the design goal of V-MASS. The total V-MASS transmission increases with larger (steeper) angles. The energy range covered by V-MASS decreases for angles deviating from about 45° as can be seen in Figure 6-11. At low energies the total transmission vanishes due to the vanishing start efficiency.

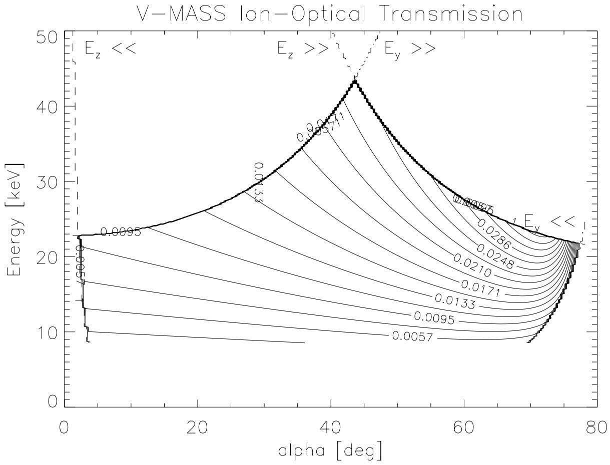

Figure 6-11: Total ion-optical transmission of V-MASS for a hyperbola voltage of 20.7 kV. Cut-offs due to geometrical limitations of the ion trajectories are given for energies perpendicular to the Vee by E_z >> from Eq. 6-45 (dashed lines) and for energies along the Vee direction by E_x >> from Eq. 6-46 (dashed-pointed line).

As stated by Eq. 6-47, the V-MASS ion-optical transmission has to be convoluted with the angular and energy scatter after the C-foil. These two functions are shown together in Figure 6-12, where the ion-optical transmission from Figure 6-11 is reproduced with the angular and energy scatter distribution for an oxygen ion entering the C-foil at 50 keV energy and 45° incident angle, and leaving the C-foil as a singly charged ion. In this example, the overlap between the ion-optical transmission and the scatter distribution is small, and the detection efficiency of V-MASS is thus small. An ion energy of 50 keV for oxygen would

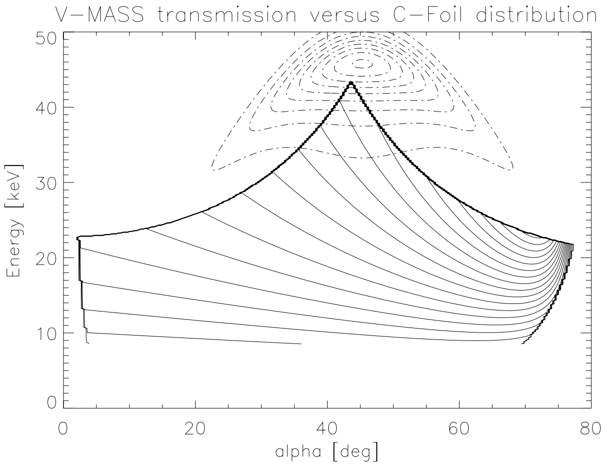

Figure 6-12: Ion-optical transmission of V-MASS (solid lines, same data as in Figure 6-11), and angular and energy scatter distribution after the C-foil for an oxygen ion entering the C-foil at 50 keV energy and 45° incident angle (dashed lines, ten contour levels).

correspond to a solar wind velocity, or rather oxygen ion velocity, of 780 km/s, which would be the fast solar wind. In case of post-acceleration by $V_F = -2500V$, this ion energy would correspond to an oxygen velocity of 650 km/s. If the entrance angle of the ions into V-MASS is different from the assumed 45°, the detection efficiency would be even smaller. Mainly this is caused by the ion-optical bending by V_F in the interface region between WAVE and V-MASS (see Eq. 6-12 and discussion before). The solar wind itself is assumed to deviate from its nominal direction ($\alpha = 45°$ in this coordinate system) typically only by a few degrees.

So far we have developed the V-MASS transmission function for the variables α and E, but the dependence on β is not covered yet. The Monte-Carlo simulations of the ion-optical transmission of V-MASS showed that the ion-optical acceptance in β can be treated independently from the other two variables, α and E. This will be done by folding two Gaussian distributions together—the distribution of ions inside the V-MASS (the angular distribution in β after passing the C-foil) and the ion-optical acceptance of V-MASS. The width of the Gaussian distribution of the ion inside the V-MASS after passing the C-foil has three independent contributions, which have to be considered

$$\sigma_\beta = \frac{1}{2\sqrt{\sqrt{2}-1}}\sqrt{\vartheta_{HWHM}^2 + \sigma_E^2 + \Delta\beta_{WAVE}^2}$$

with ϑ_{HWHM} being the angular scattering in the C-foil (see Eq. 6-18) we used already above, σ_E being the contribution due to the finite energy spread of the incoming ions (the ion temperature), and $\Delta\beta_{WAVE}$ being the broadening of an ion beam emerging from the WAVE (see Eq. 6-9). The transmission in β is then

$$T_\beta = \frac{1}{\sqrt{2\pi\sigma_\beta}}\exp\left(-\frac{1}{2}\frac{(\beta-\beta_{SW})^2}{\sigma_\beta^2}\right)\cdot\frac{1}{\sqrt{2\pi\beta_{V-MASS}}}\exp\left(-\frac{1}{2}\frac{\beta^2}{\beta_{V-MASS}^2}\right) \qquad \text{Eq. 6-48}$$

with $\beta_{V-MASS} = 3.0°$ being the Gaussian width of the ion-optical acceptance of V-MASS along the β coordinate. Thus we have the total transmission of V-MASS given by

$$T_{V-MASS} = T_{ion-opz}\cdot\eta_{START}\cdot\eta_{ion}\cdot\eta_{STOP}\cdot T_\beta \ . \qquad \text{Eq. 6-49}$$

Using the effective area (Chapter 6.1) and the total transmission for a species *i*, we can calculate the actual flux f_i of an element *i* from its count rate c_i by using

$$f_i = \frac{c_i}{\tilde{A}_{eff}\,T_{V-MASS}} \qquad \text{Eq. 6-50}$$

Eq. 6-50 is a complicated function of α, β, v_{SW}, V_F, V_{WAVE}, and of the element and its isotope, as has been discussed above. Since most of these parameters change with time, either as planned due to the stepping sequence of MTOF or stochastically in the solar wind, a lot of computations have to be performed to obtain an extended time series for a certain species.

6.4 Discussion of the Instrument Function

MTOF instrument function is a rather involved calculation and it is difficult to get a “feeling” for the MTOF sensor response for different solar wind conditions. In order to assist the understanding of the MTOF instrument function we want to present a few examples of the building blocks of the instrument function. The MTOF instrument function is a function of quite a number of parameters, both solar wind plasma parameters and sensor settings. Here we study only the most important one, the solar wind velocity. First, we take a look at the active area of the WAVE entrance system. Then we study the V-MASS section, investigating the total transmission for a few selected elements and the effect of the instrumental isotope fractionation.

6.4.1 Entrance System Transmission

The effective area of the WAVE entrance system, including the interface to the V-MASS spectrometer, is shown in Figure 6-13 for O^{6+} ions for two typical settings of V_{WAVE}. The data in Figure 6-13 are calculated for a Mach number of 20, which still can be considered as cold solar wind. Typically a Mach number of 10 is observed in the solar wind at 1 AU. With these two settings of the WAVE entrance system one can cover quite a large range of solar wind velocities. For O^{6+} ions this range extends from about 300 km/s to more than 1000 km/s. This solar wind range becomes smaller and shifts to lower solar wind velocities for heavier ions.

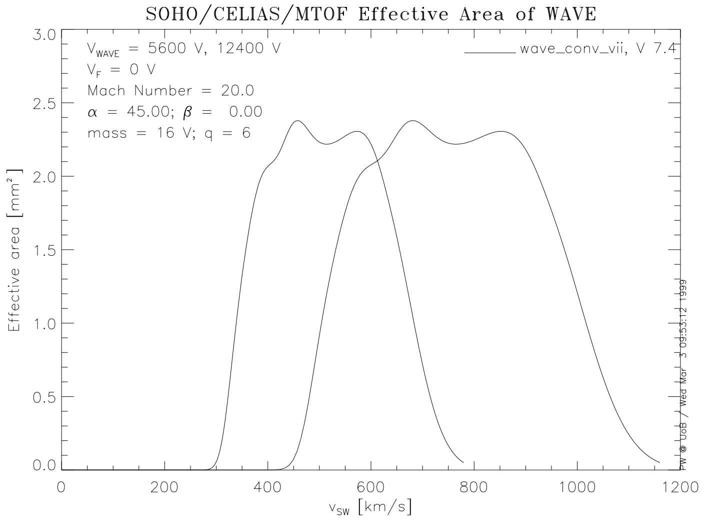

Figure 6-13: Effective area of the WAVE entrance system, including the interface to V-MASS for two typical settings of V_{WAVE} versus solar wind velocity (proton velocity).

6.4.2 The V-MASS Transmission

In Figure 6-14 we show the total transmission of the isochronous TOF mass spectrometer for oxygen, silicon, and iron, the three elements investigated in Chapter 2, for negative and zero values of the potential difference between the entrance system and V-MASS (V_F). To obtain the total sensor response these numbers have to be multiplied by the response of the entrance system, including the interface to the V-MASS, which is given as an active area, typically 2 mm^2 for a large solar wind velocity range (see Figure 6-13 above). As can be seen from Figure 6-14, the transmission of the TOF mass spectrometer varies over several orders of magnitude depending on the solar wind conditions and the sensor settings, which complicates the data analysis significantly. The maximum in the V-MASS transmission corresponds to at best 2000 counts for oxygen and about 200 counts for iron during a five-minute integration period for typical densities of heavy ions.

The stepping sequence of the MTOF sensor has been optimized to cover a broad range of solar wind conditions. Each step of the MTOF sensor cycle takes five minutes, thus the total sequence takes 30 minutes to finish. However, since each step has quite a large energy bandwidth, overlapping with the other steps considerably, a time resolution of five minutes can be obtained if the sensitivity of the MTOF sensor is high enough for the particular element considered. For typical solar wind conditions and for the more abundant elements in the solar wind, like oxygen, silicon, and iron, it is indeed possible to derive densities with such a high time resolution (see Chapters 2 and 3).

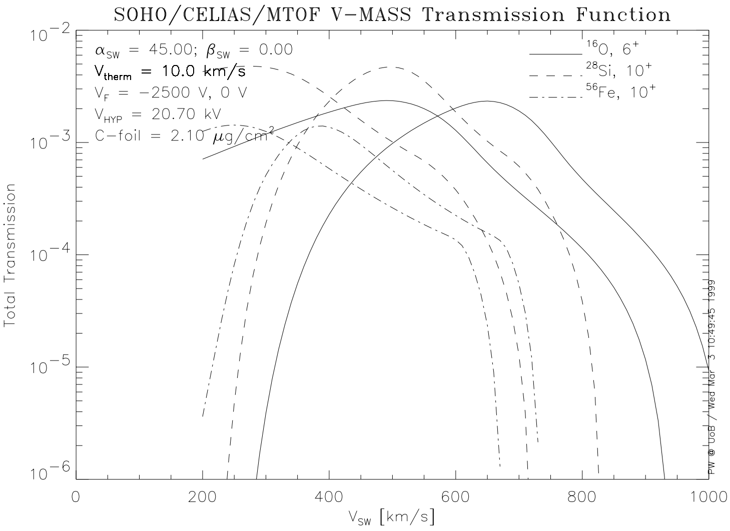

Figure 6-14: Total transmission of the isochronous TOF mass spectrometer is plotted for the three elements O, Si, and Fe investigated in Chapter 2, for two potential differences between the entrance system and the isochronous TOF mass spectrometer ($V_F = -2500V$ and $V_F = 0V$). The transmissions for $V_F = -2500V$ peak at lower solar wind velocities.

6.4.3 Isotopic Fractionation in V-MASS

The V-MASS instrument function is not exactly the same for the different isotopes of an element. There is the further complication that different isotopes of an element do not enter MTOF with the same kinetic energy, but they enter into the WAVE entrance system with the same velocity. In the following we illustrate this instrumental fractionation using the two iron isotopes ^{54}Fe and ^{56}Fe, for which in a preliminary analysis an isotopic abundance has been reported in Chapter 2.5.

The WAVE entrance system selects the incoming ions by E/Q; thus different ion energies of the different isotopes will result in a different active area. However, most of the isotope fractionation occurs in the V-MASS spectrometer. The angular scattering is only a function of the atomic number and the energy (see Eq. 6-17). Since the energy of the different isotopes is not the same, lighter isotopes will scatter more upon passage through the C-foil, and their V-MASS transmission will be reduced (particularly at lower solar wind velocities). The energy loss of an ion upon passage through the C-foil is a complicated function of the energy, the mass, and the atomic number of the projectile (among other parameters), which results in a higher energy loss for the lighter isotopes at the same velocity. At high solar wind velocities, particularly at the wing of the V-MASS transmission, this effect favors the lighter isotope. In Figure 6-15 we show the ratio of the total V-MASS transmission for ^{54}Fe and ^{56}Fe. At lower solar wind velocities the heavier isotope is at an advantage due to the lower angular scattering in the C-foil. At higher solar wind velocities the lighter isotope is at an advantage because of its larger

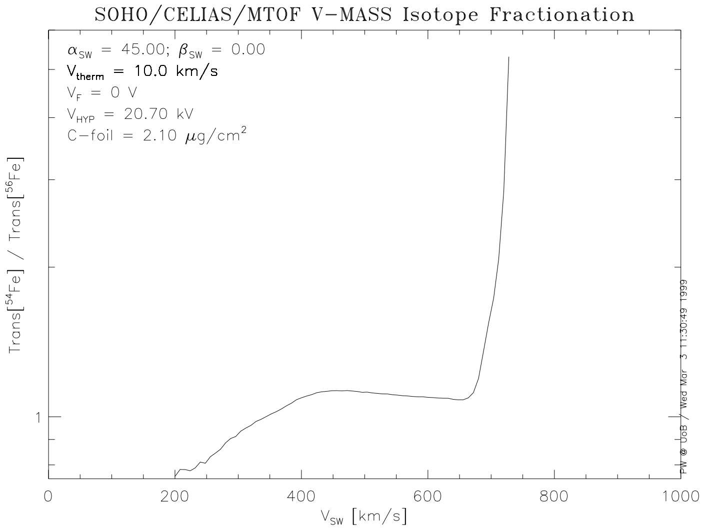

Figure 6-15: Ratio of the total V-MASS transmission functions for ^{54}Fe and ^{56}Fe illustrating the isotope fractionation in V-MASS.

energy loss, which means it is still inside the energy acceptance of V-MASS. Especially at higher solar wind velocities the instrument fractionation is large, and one cannot hope that all the possible instrument fractionation is properly handled by the instrument function. Thus one has to be careful when studying isotope ratios of iron at solar wind velocities in excess of 600 km/s.

7 Calibration

Calibration data for a sensor are important in understanding the response of the sensor to the entering plasma and in eventually making quantitative statements about the measurements. Unfortunately, the calibration data are limited both in extent and also as to the number of elements that were covered. The former limitation was a result of a very pressing schedule before the delivery of the MTOF sensor for integration on the SOHO spacecraft. The latter limitation resulted from restrictions of the CASYMS calibration facility to produce ions only from selected gases introduced into the ion source [110]. The Mefisto facility, which has an electron cyclotron resonance ion source that allows the production of ion beams for every element found in the solar wind with approximately the charge state in the solar wind, was not available at the time [145; 146].

Calibration was performed for components of the MTOF sensors as well as for the whole sensor. The calibration of the entrance system, WAVE, and its implementation in the instrument function has already been discussed in detail in Chapter 6.1 and will not be repeated here. In the following, calibration of the time-of-flight part of MTOF, the V-MASS, and an end-to-end calibration will be presented.

7.1 Calibration of the MTOF Flight Sensor

Calibration of the MTOF flight sensor took place at the CASYMS facility at the University of Bern, with and without the WAVE entrance system installed in the MTOF sensor. These calibrations have been reported on in detail in the thesis work by Hefti [147], and will not be reproduced here.

7.2 Calibration of the MTOF Flight-Spare Sensor

The MTOF spare sensor was calibrated in the CASYMS calibration facility [110] in March 1998. Calibration runs were made with and without the WAVE entrance system installed in the sensor. Also, the PM of the MTOF spare sensor was calibrated during that campaign. The ions H^+, He^+, O^+, and Ar^+ were used. H^+ and He^+ ions were used to check the response of the entrance system up to the carbon foil; O^+ and Ar^+ ions were used to investigate the V-MASS unit. The results for the oxygen calibration for the DCR/FSR[4] ratio are shown in Figure 7-1 together with the total transmission of the V-MASS unit (from Eq. 6-42), which has been scaled by a factor of 0.81 to match the calibration data. The total transmission of the V-MASS unit also contains the start efficiency of the V-MASS for oxygen, which amounts to 0.8 to 0.95 in the covered velocity range. The agreement between the calibration data of the MTOF spare

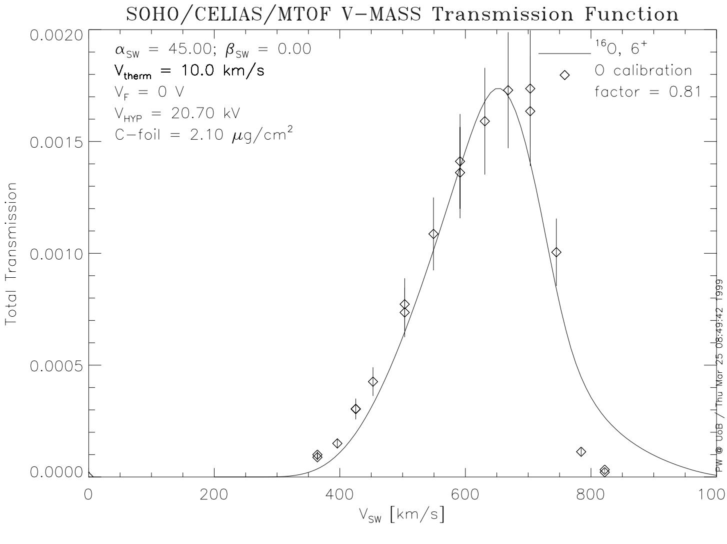

Figure 7-1: Total transmission through V-MASS for oxygen ions, together with calibration data (DCR/FSR) for the MTOF spare unit taken at the CASYMS calibration facility of the University of Bern. Error bars on the calibration data are assumed to be ±15%.

---

[4] Double Coincidence Rate (DCR) versus the First SEDA Rate (FSR), with SEDA standing for Secondary Electron Detection Assembly, which is the start detector.

and the theoretical transmission is reasonably good. Only at higher solar wind velocities, at the wings of the transmission curve, it appears that the theoretical function overestimates the measured transmission significantly. However, from the comparisons with CTOF data we learned that at higher solar wind velocities the instrument function seems to give too low a value. The MTOF spare unit is supposed to be identical to the MTOF flight unit and their performances should be the same, which is probably true for most of the parts, although the thickness of the carbon foil is always a point of concern.

7.3 Calibration of the ACE/SWIMS Flight Sensor

Since the ACE/SWIMS sensor is very similar to the CELIAS/MTOF sensor we can compare ACE/SWIMS calibration data with the MTOF instrument function. Actually, the ACE/SWIMS sensor is a modified MTOF sensor built from spare parts. The ACE/SWIMS calibration data were taken at the University of Gießen, Germany, using a 14 GHz ECR ion source facility [148; 149]. The comparison between the ACE/SWIMS DCR/FSR efficiency and the corresponding module of the MTOF instrument function (the V-MASS response, see Chapter 6) is given in Figure 7-2 for iron and in Figure 7-3 for oxygen. The plotted data are the entire available data set for oxygen and iron from this calibration for various instrument settings for the indicated energy range. For oxygen the V_{HYP} range is from 9 kV up to 21 kV and the V_F range is from –1500 V to +1500 V. For iron the V_{HYP} range is from 16.4 kV up to 24.3 kV and the V_F range is from –2500 V to +2000 V. The scattering of data points is in part due to the different instrument settings used for these measurements. Also, the stability of the ion beam was low since the beam intensity of the ECR ion source had to be reduced by several orders of magnitude not to exceed the count rates the ACE/SWIMS sensor can handle.

The agreement between the measured data for the ACE/SWIMS sensor and the MTOF instrument model function is reasonable, taking into account that the interface between the WAVE entrance system and the V-MASS unit has been improved for the ACE sensor. This causes a different V_F dependence and particularly shows up for higher energies (see Figure 7-2). Also, the start detector has been modified for the ACE/SWIMS sensor. The MTOF instrument model data had to be multiplied by a factor of about three for oxygen and seven for iron to match the measured data best. This probably reflects the improvements in the interface between the WAVE entrance system and the V-MASS unit, which were made with the goal of improving the transmission in this critical ion-optical area. For low energies the scattering of measured data points is even larger, which is caused by the low signal-to-noise ratio at these energies. A large signal background is always found at sensor temperatures above 0°C for this design and was a

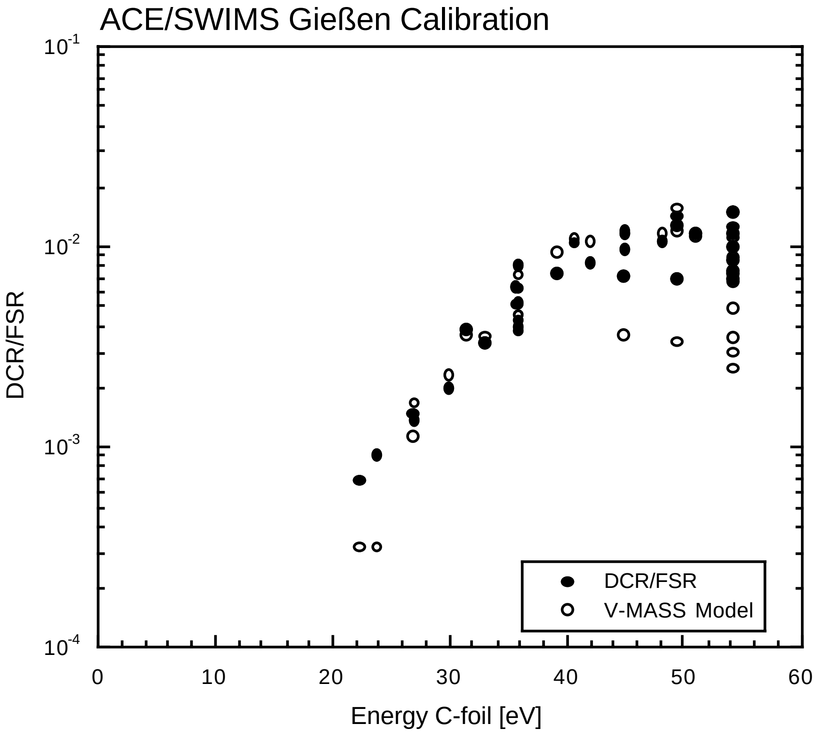

Figure 7-2: Comparison of ACE/SWIMS iron calibration data with the MTOF instrument function. Full symbols are the ACE/SWIMS DCR/FSR data. The open symbols give the result of the V-MASS module of the MTOF instrument function evaluated at the ACE/SWIMS instrument settings for each measurement, scaled by a factor of 6.7.

persistent problem during calibration. Total efficiency calibrations were not possible for oxygen and iron ions because of problems with the stability of the ion beam.

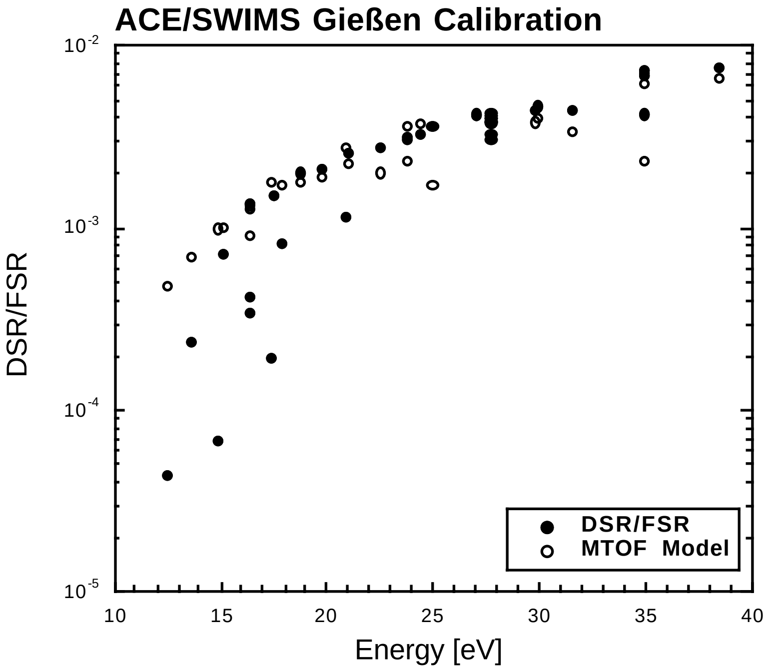

Figure 7-3: Comparison of ACE/SWIMS oxygen calibration data with the MTOF instrument function. Full symbols are the ACE/SWIMS DCR/FSR data. The open symbols give the result of the V-MASS module of the MTOF instrument function evaluated at the ACE/SWIMS instrument settings for each measurement, scaled by a factor of 3.

7.4 In-Flight Calibration of MTOF with CTOF Data

Since the amount of calibration data for the MTOF sensor is limited and absolute calibrations are not available, an in-flight calibration was necessary to determine the absolute efficiency for the measurements. We used the opportunity to compare the oxygen and iron densities we derived from MTOF data with data derived from the CTOF sensor in the thesis works of Aellig [150] and Hefti [147]. Moreover, since the MTOF sensor response is rather involved compared to SWICS-type sensors (see Chapter 6), these comparisons helped to improve many details in the MTOF instrument function.

CTOF data are available for the time period from DOY 150 to 229 of 1996. There are some CTOF data starting with DOY 92 of 1996, but the post-acceleration of CTOF was at a lower value then and the absolute efficiencies are not known well enough to serve for an intercalibration between the two sensors. After DOY 229, 1996, CTOF had a failure in the post-acceleration and deflector power supplies, which limited the performance of the sensor considerably. In spite of this, in the time period we studied we have about 20’000 individual measurements for which we can compare the MTOF and CTOF data.

For the oxygen densities this comparison is shown in Figure 7-4, where the ratios of the oxygen density measured with MTOF versus the oxygen density measured with CTOF are plotted for a total of about 20’000 measurements taken at five-minute intervals. This ratio should of course be one for each measurement. On average we find good agreement between the two sensors. However, there is a small modulation of this ratio with solar wind velocity. The scattering of individual measurements performed with five-minute time resolution is larger for the MTOF sensor since its overall transmission is significantly lower than the transmission of

CTOF. Typically, the efficiency of the TOF section of the CTOF sensor is 0.3 [150] compared to at best 0.01 for MTOF (see Figure 6-14), and the active area of CTOF is 16 mm^2 [150] compared to 2 mm^2 for MTOF (see Figure 6-13). This makes a factor of about 1000 more signal for CTOF than for MTOF.

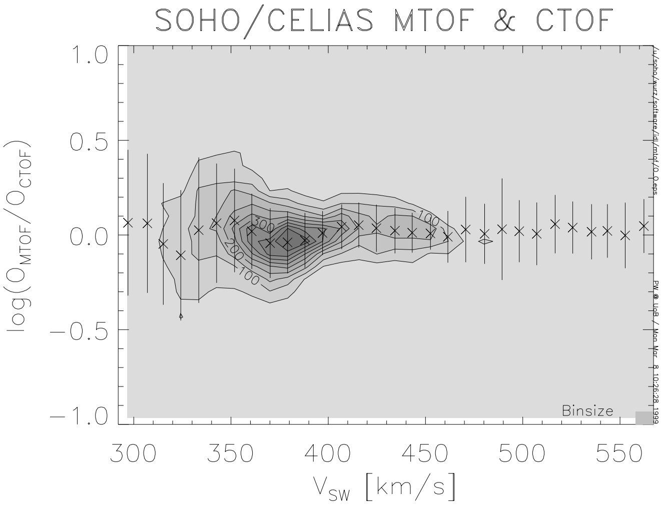

Figure 7-4: Logarithm of the ratio of the O densities measured with the CELIAS/MTOF sensor versus the O densities measured with the CELIAS/CTOF sensor for a time period from DOY 150 to DOY 229 of 1996, with a total of about 20’000 measurements at 5-minute intervals. The contour lines give the number of measurements for a particular bin. During that time period there was mostly slow solar wind, which explains the clustering of measurements between 350 and 400 km/s. The overlaid symbols are the mean for a particular velocity bin and the error bars are the standard deviation of log(O_{MTOF}/O_{CTOF}) for a single measurement.

For the iron densities the comparison between MTOF and CTOF is shown in Figure 7-5, also for a total of about 20’000 measurements taken at five-minute intervals. On average we find good agreement between the two sensors, better than the comparison for the oxygen density. The scattering of individual measurements performed with five-minute time resolution is again larger for the MTOF sensor since its overall transmission is significantly lower than the transmission of CTOF, particularly for high solar wind velocities. Furthermore, the range of solar wind velocities which can be investigated for iron is limited for high solar wind velocities because the transmission becomes very small (see Figure 6-14).

There is no systematic dependence of the instrument function on solar wind velocity (shown in Figure 7-4 and Figure 7-5) and other solar wind plasma parameters like thermal velocity, flow direction, measured freeze-in temperature, and others which are not shown here.

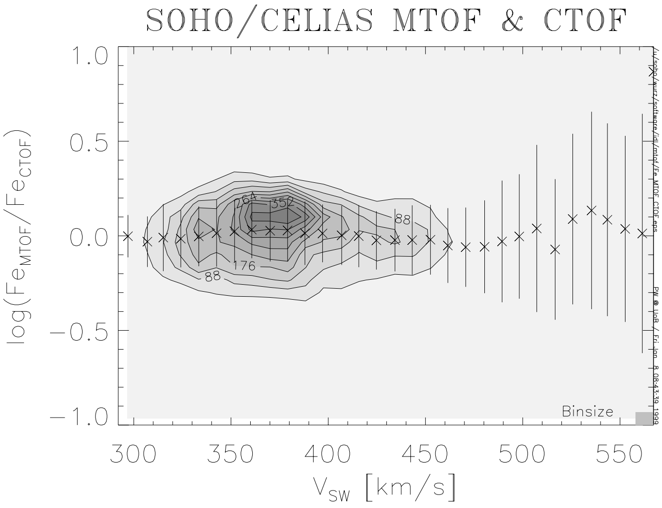

Figure 7-5: Logarithm of the ratio of the Fe densities measured with the CELIAS/MTOF sensor versus the Fe densities measured with the CELIAS/CTOF sensor for a time period from DOY 150 to DOY 229 of 1996, with a total of about 20’000 measurements at 5-minute intervals. The contour lines give the number of measurements for a particular bin. During that time period there was mostly slow solar wind, which explains the clustering of measurements between 350 and 400 km/s. The overlaid symbols are the mean for a particular velocity bin and the error bars are the standard deviation of log(Fe_{MTOF}/Fe_{CTOF}) for a single measurement.

These comparisons between MTOF and CTOF data have also been used to establish an absolute calibration of MTOF under the assumption that the oxygen and iron densities derived from the CTOF sensor are the true values. Since the instrument function of the CTOF sensor is simpler and reasonably well understood [147; 150] this assumption appears to be well justified. Moreover, this approach was necessary since there are no alternatives for an absolute calibration of MTOF. The result of the inter-calibration between MTOF and CTOF is that the total transmission of V-MASS has to be multiplied with a calibration constant to make the MTOF densities agree with the CTOF measurements. Thus the ion-optical acceptance of V-MASS (Eq. 6-42) becomes

$$\tilde{T}_{V-MASS} = T_{V-MASS} \cdot C_i \qquad \text{Eq. 7-1}$$

and the actual flux f_j from the count rate c_j becomes

$$f_j = \frac{c_j}{\tilde{A}_{eff}\, T_{V-MASS}\, C_i} \quad . \qquad \text{Eq. 7-2}$$

The calibration constant C_i is different for each element i. For oxygen and for iron the calibration constants are derived directly from the comparison with CTOF data and are 0.783 and 0.949, respectively. The calibration constant obtained for oxygen is almost the same as the factor between the MTOF instrument function and the calibration data of the MTOF spare reported in Chapter 7.2. Thus, future post-launch calibration campaigns using the MTOF spare sensor will help in the understanding of the MTOF flight sensor. With these calibration constants the data in Figure 7-4 and Figure 7-5 shift up or down depending on the value of the constant. For the other elements, the calibration constants have to be interpolated.

The need for these calibration constants arises from the fact that large parts of the MTOF instrument function are of theoretical nature and not measured for the components of MTOF. Only the entrance system has been well characterized by calibration at the University of Bern. The interface between WAVE and V-MASS is already less characterized by measurements and a possible source of problems. The total V-MASS transmission is based on a Monte-Carlo simulation of its ion-optical transmission; the C-foil response, which is based partly on simulation and partly on adaptations of literature results; the ionization efficiencies after the C-foil have been measured; and the secondary electron efficiency of the C-foil is based on literature results and simulations. In conclusion, the fact that the calibration factors are so close to one given the complexity of the instrument function is a pleasant surprise.

8 Data Analysis

In this chapter we present the details of the data extraction and explain how the application of the instrument function is performed. The software package for the MTOF data analysis consists of more than 50 modules with a total of more than 8000 lines of code. Most of the software is written in IDL; only the module to calculate the charge-state distribution for a given freeze-in temperature is written in FORTRAN. The latter module has been adapted from the original code provided by [23]. The structure of the software package and the data flow are shown in Figure 8-1. For the data analysis we need to read-in the V_F, V_{WAVE}, and V_{HYP} house-keeping data. These data are needed for the calculation of the effective area of the WAVE entrance system, for the final energy of the ions when they enter V-MASS, and for the V-MASS transmission. Furthermore, we need the solar wind plasma data derived from the Proton Monitor[5], the solar wind velocity, v_{SW}, the thermal velocity, v_{therm}, and the flow direction out-of the ecliptic plane, β. Using these data, we calculate the plasma parameters of the heavy ions in the solar wind—namely the energies and energy spreads, the freeze-in temperatures, and the charge-state distributions. In addition, there are further assumptions about heavy ions in the solar wind, which are detailed below.

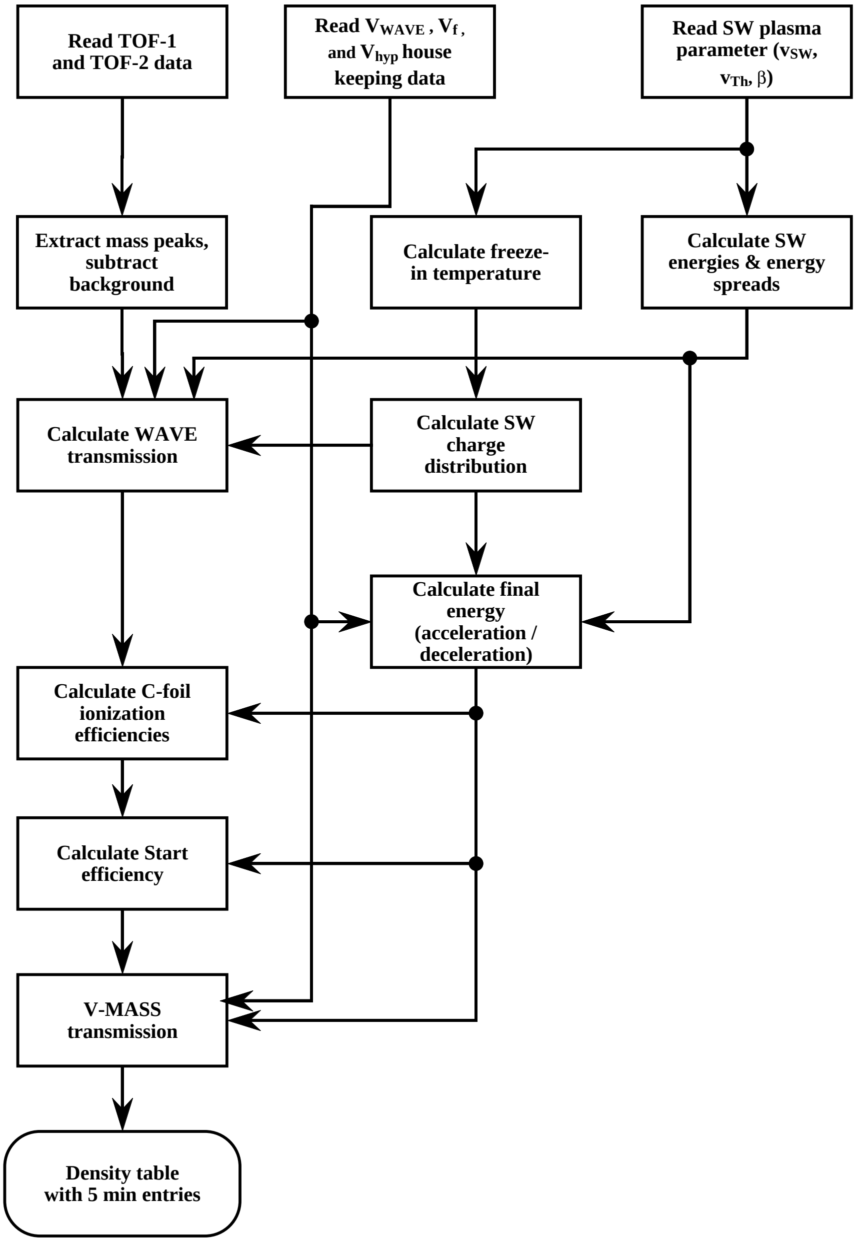

Figure 8-1: Top-level representation of the modules and the data flow for the MTOF data analysis used in this study.

We use the near and the far TOF spectra for the analysis (TOF-2 and TOF-1 spectra, respectively). Each of these TOF spectra are accumulated over five minutes by the CELIAS DPU and sent to ground. These spectra have 1024 TOF channels covering a mass range from hydrogen up to mass 70 for typical settings of the hyperbola voltage and the TOF measurement. See Figure 1-1 for a representative mass spectrum obtained from the TOF data. Some of the

---

[5] These data are calculated from PM measurements by Fred M. Ipavich and his colleagues at the University of Maryland, and are distributed among the CELIAS team members.

recorded data are also transmitted as Pulse Height Analysis (PHA) data, which contain the TOF of the registered ion with four times more time resolution, the amplitudes of the start and stop signals, and the stop location on the detector along the *y*-axis. Only a fraction of these data is transmitted to ground due to the large amount of this data type. The near and far TOF spectra have a big advantage over the PHA data in that they contain every ion, which has been recorded by MTOF. This is of particular importance when studying ions of low abundance. For a detailed description of the different data types of the CELIAS experiment the reader is referred to the Data Phase Manual [151].

The extraction of count rates from the recorded TOF spectra is either done by fitting a line profile and a background to the recorded TOF peak or by performing a minimum variance evaluation. If the TOF peak contains more than five counts peak fitting is used; otherwise the minimum variance method is applied. This decision is based on the sum of counts in the TOF interval where the TOF peak is supposed to be located. The peak fitting is done using a non-linear least square method and is detailed below. The minimum variance evaluation has been adapted from Bochsler [35]. The peak fitting method is usually superior to the minimum variance evaluation because it accounts for the changing peak width, the changing peak position, and the actual background. For the minimum variance evaluation we have to assume the nominal peak shape and position, and also a background, which has been determined before. The peak fitting, however, breaks down when the count rates get too low and the fit procedure does not converge. From evaluations of flight data and simulated data (with a low signal-to-noise ratio) it was determined that five counts is a suitable dividing line between the two methods.

The next step is to calculate all the components of the instrument function, the active area of the WAVE, the ionization efficiency, the start efficiency, and the V-MASS transmission. These components are put together (see Chapter 6) and applied to the raw counts of a mass peak to obtain particle fluxes of the elements. If necessary, an interference from a heavier doubly charged ion is accounted for (for example, at $m/q = 28$ we have contributions from $^{28}\mathrm{Si}^{+}$ and $^{56}\mathrm{Fe}^{++}$). In the final step the particle fluxes are converted to particle densities by dividing by the solar wind velocity.

8.1 Extraction of Raw Counts from the TOF Spectra

The raw counts contained in a mass line are extracted from the TOF spectra by fitting a Gaussian line profile and a quadratic background to the recorded data

$$y(x,\mathbf{a}) = a_1 \exp\left(-\frac{1}{2}\frac{(x-a_2)^2}{a_3^2} \right) + a_4 + a_5 x + a_6 x^2 \qquad \text{Eq. 8-1}$$

with $\mathbf{a} = (a_1, a_2, a_3, a_4, a_5, a_6)$. For short accumulation periods the TOF peak resembles a Gaussian pretty well. Only for longer accumulation periods does the peak become asymmetric, being wider at the side of higher TOFs. This is mainly caused by the bulk flow angle of the solar wind out-of the ecliptic plane ($\beta \neq 0$), as was discussed in Chapter 5.2. Although we are fitting a function with six parameters to the recorded TOF peak, we are only interested in the peak area, that is the total number of counts, for this mass line

$$C = a_1\, a_3 \sqrt{2\pi}\,.$$

Since Eq. 8-1 is a non-linear function in *x*, we will use a non-linear least square method for the fitting, as has been described by Bevington [152]. We define the measure of goodness of the fit χ^2 as

$$\chi^2 = \sum \left(\frac{1}{\sigma_i^2} \left\{ y_i - y(x_i) \right\}^2 \right) \qquad \text{Eq. 8-2}$$

where the σ_i are the uncertainties in the data points y_i. According to the method of least squares, the optimum values of the parameters a_j are obtained by minimizing χ^2 with respect to each of the parameters simultaneously. The gradient of χ^2 with respect to the parameters a_j, which will be zero at the minimum, has the components

$$\frac{\partial\chi^2}{\partial a_j} = -2\sum_{i=1}^{n}\frac{\left[y_i - y(x_i,\mathbf{a})\right]}{\sigma_i^2}\frac{\partial y(x_i,\mathbf{a})}{\partial a_j} \qquad \text{Eq. 8-3}$$

In the search for an optimal fit, all parameters a_j are incremented simultaneously, with the relative magnitudes adjusted so that the resultant direction of travel in parameter space is along the gradient of χ^2, that is the direction of maximum variation (gradient search method). Using the abbreviation

$$\beta_j = -\frac{1}{2}\frac{\partial\chi^2}{\partial a_j}$$

we compute the increments δa_j, added to the current approximation, to give the next approximation from

$$\delta a_l = \text{constant} \times \beta_l \ . \qquad \text{Eq. 8-4}$$

The constant in Eq 8-4 has to been chosen such that it does not exhaust the gradient of χ^2 by the step taken. The gradient search is ideally suited to approach the minimum from far away, but suffers markedly as the search approaches the minimum because the derivative becomes very small resulting in a small step size. The small step size causes an inefficient search once we are close to the minimum, and possibly we will never reach it this way.

As has been described by Bevington, we will smoothly vary between two methods, the inverse-Hessian method once we are close to the minimum of χ^2, and the gradient search for the initial approach to the minimum [152]. Taking an additional partial derivative of Eq. 8-1 gives

$$\frac{\partial^2\chi^2}{\partial a_j \partial a_l} = 2\sum_{i=1}^{n}\frac{1}{\sigma_i^2}\left[\frac{\partial y(x_i,\mathbf{a})}{\partial a_j}\frac{\partial y(x_i,\mathbf{a})}{\partial a_l} - \left[y_i - y(x_i,\mathbf{a})\right]\frac{\partial^2 y(x_i,\mathbf{a})}{\partial a_l \partial a_j}\right] \qquad \text{Eq. 8-5}$$

Using the abbreviation

$$\alpha_{jl} = \frac{1}{2}\frac{\partial^2\chi^2}{\partial a_j \partial a_l} \qquad \text{Eq. 8-6}$$

which is the Hessian matrix multiplied by one half, usually called the curvature matrix, we can get the increments δa_j by solving the following set of linear equations

$$\sum_{l=1}^{m}\alpha_{jl}\delta a_l = \beta_j \ . \qquad \text{Eq. 8-7}$$

The second derivative terms contained in Eq. 8-7 can have a destabilizing effect if the model fits badly or the data are contaminated by outlying points. Thus, instead of Eq. 8-6 we use

$$\alpha_{jl} = \sum_{i=1}^{n}\frac{1}{\sigma_i^2}\left[\frac{\partial y(x_i,\mathbf{a})}{\partial a_j}\frac{\partial y(x_i,\mathbf{a})}{\partial a_l}\right] .$$

Now we can derive the constant in Eq. 8-4 from the matrix α by

$$\delta a_l = \frac{1}{\lambda\alpha_{jl}}\beta_l \text{ or } \delta a_l \lambda \alpha_{jl} = \beta_l \qquad \text{Eq. 8-8}$$

The Eq. 8-7 and Eq. 8-8 can be combined by defining a new matrix α' with the following prescription

$$\begin{aligned} \alpha'_{jj} &\equiv \alpha_{jj}(1+\lambda) \\ \alpha'_{jl} &\equiv \alpha_{jl} \quad (j \neq l) \end{aligned} \qquad \text{Eq. 8-9}$$

If λ is very small, Eqs. 8-9 are similar to the solution of Eq. 8-7 (the Hessian method). If λ is very large, the diagonal terms of the curvature matrix dominate and the matrix equation becomes identical to Eq. 8-8 (the gradient method). A typical starting point is λ=0.001. Depending on the slope of the derivative, λ will be decreased or increased. For each iteration it may be necessary to recompute the parameter increments δa_j several times to optimize λ. As the solution approaches the minimum, λ will be reduced in order to smoothly switch to the Hessian method.

This algorithm typically performs about five iterations to fit a larger ion peak of 100 counts and more, for example, the iron mass line, and about 15 iterations for a less abundant ion, for example, for the calcium mass line. It is important to have initial values for a_j reasonably close to the best-fit value, otherwise the routine fails to make a good fit. Finding a set of good start values is rather easy in our case. From the total counts at the expected peak position we derive an estimate for a_1. We derive a_2 from the expected time of flight (rather, the channel number) for a particular ion for a given hyperbola voltage. From the mass resolution of MTOF we calculate a_3. We also have an estimate of the background a_4. The parameters a_5 and a_6 are set to zero initially. Since this fitting routine runs completely autonomously, we have introduced limits, which each parameter a_j can assume in order to make sure the fits are reasonable:

$$a_{j,\min} \leq a_j \leq a_{j,\max} \qquad \text{Eq. 8-10}$$

We know the range of channel numbers the center of a mass line can assume for a particular element, we also know the range of possible mass resolutions for a mass line, and furthermore we don’t allow the peak to have a negative amplitude.

Each spectrum accumulated over a five-minute interval is evaluated individually. Since the peak positions, the mass resolution, and the background level vary from spectrum to spectrum, time resolution and sensitivity would be degraded if the raw data were first accumulated over larger time intervals and the peak extraction performed afterwards on such an accumulated spectrum. The near and far spectra are fitted separately, since they have different peak positions for each element and different background levels. Once the raw counts for a mass peak have been extracted from the near and far spectra, these are added together and the instrument function is applied to derive the particle flux for the element. Although each fit takes only a few iterations, doing that for several masses and all five-minute spectra consumes quite some computer time. About a third of the time necessary to derive calibrated data is used for the peak extraction.

8.2 Further Assumptions

In addition to the calculation of the MTOF instrument function for the actual solar wind plasma parameters and MTOF sensor settings, we need to introduce some knowledge of the solar wind for the analysis of MTOF data, because not all necessary solar wind plasma parameters are measured by MTOF/PM, nor are not available from CTOF data. To derive the charge distributions of the heavy ions we use the freeze-in temperature, which we derive from the solar wind velocity. For the velocity of the heavy ions we calculate an element- and velocity-dependent difference compared to the proton velocity.

8.2.1 The Freeze-in Temperatures of the Elements

Another input parameter needed for the determination of the MTOF sensor response is the charge state distribution of the solar wind ions for every element and for every accumulation interval. In particular, for the response of the entrance system we need to know the parameter

E/Q for the incoming ions. Also, for the post-acceleration and the deceleration due to V_F, the charge distribution is an important variable to know. The MTOF sensor determines only the mass of the incoming ion. The charge information of the incoming ions is lost because the ions undergo efficient charge exchange processes inside the sensor when they pass the carbon foil of the isochronous TOF mass spectrometer. For the evaluation of the MTOF instrument function, however, we need to know the charge distribution of each element.

Originally it was planned to obtain the charge distribution for a few ions from the measurements made by the CTOF sensor with the same time resolution. From these measurements we intended to infer the charge state distribution for the other elements. Unfortunately, there was a failure in the high voltage power supplies of CTOF at the end of August 1996, which reduced the CTOF performance to such a level that charge state distributions are impossible to measure. Therefore, we had to find some other source for this crucial information. During the years 1996 and 1997 there was also no other mission from which these data could be obtained, so we had to derive this information by other means.

The charge state distributions used for the elements in the MTOF data evaluation are derived from the freeze-in temperature. The freeze-in temperature is the electron temperature in the corona at the place where a certain charge state ratio of an element ceases to adjust to the changing conditions. This freeze-in temperature is different for each element since it also depends on atomic properties [3; 32]. There are some recent reports on the correlation between the solar wind velocity and the freeze-in temperatures of ions [20-22], where a linear relationship between the solar wind velocity and the freeze-in temperature was found. Also, a linear relationship between the carbon and the oxygen freeze-in temperatures has been reported, with the oxygen temperature being about 22% higher [153]. Thus, we can derive the so-called freeze-in temperature $T_{f,i}$ for the element *i* from the measured solar wind velocity by using the following relation:

$$T_f(i) = T_0(i) - T_S(i) v_{SW} \qquad \text{Eq. 8-11}$$

with v_{SW} the solar wind velocity (the proton velocity), and the parameters T_0 and T_S extracted from literature or derived by interpolation between known parameters. The parameters T_0 and T_S are given in Table 8-1.

In the papers by Geiss *et al.* [32] and von Steiger [3] there is a graph giving the freeze-in temperatures of carbon and oxygen, together with the solar wind velocity for a certain time period (Figure 3 in these references). From these data we extracted the relationship between the freeze-in temperature and the solar wind velocity for these two elements. For helium the same parameters are used as for carbon. This is uncritical, since helium is always doubly charged at temperatures around 1 MK. The adopted parameters for oxygen incorporate the work mentioned before [3; 32] and a recent report of measurements by Hefti *et al.* [21; 147]. The parameters for nitrogen are interpolated so that the curve (Eq. 8-11) lies between the carbon and oxygen curves. For neon we adopt the same parameters as for oxygen. The parameters for silicon were derived from two measurements. For the slow solar wind around 400 km/s there is the measurement of the freeze-in temperature of 1.7 MK by Galvin *et al.* [154]; for the fast solar wind at 700 km/s there is the measurement of 1.4 MK by Geiss *et al.* [32]. For the elements sodium, magnesium, aluminum, and sulfur the same parameters are used as for silicon, since no other information is available. The parameters for calcium are derived using the reported freeze-in temperature of 1.53 MK at v_{SW} < 380 km/s from Kern *et al.* [73] and assuming a freeze-in temperature of 1.1 MK at v_{SW} = 700 km/s (similar to the iron freeze-in temperature at that proton velocity). For argon the same parameters as for calcium are adopted. The parameters for iron are taken directly from the reported measurements by Aellig [150].

From the freeze-in temperature we obtained charge state distributions for each element by assuming an ionization equilibrium in the corona and by applying ionization and recombination rates for electronic collisions from Arnaud and co-workers [23; 24]. It is known that a single freeze-in temperature usually cannot describe the observed charge state distributions of iron all that well [150; 153], but the obtained charge state distribution is good enough for the analysis of MTOF data.

Table 8-1: Parameters used for the algorithm to derive the freeze-in temperatures of the elements from the solar wind proton velocity.

Element	T_0 [K]	T_S [K s/m]	Reference / Comments
Helium	$2.0118\ 10^6$	1.4773	Carbon for helium
Carbon	$2.0118\ 10^6$	1.4773	Geiss *et al.* [32] and von Steiger [3]
Nitrogen	$2.0100\ 10^6$	1.9959	This work [1)]
Oxygen	$2.0280\ 10^6$	1.1013	Geiss *et al.* [32] and Hefti *et al.* [21; 147]
Neon	$2.0280\ 10^6$	1.1013	Oxygen for neon
Sodium	$2.1920\ 10^6$	1.1320	Silicon for sodium
Magnesium	$2.1920\ 10^6$	1.1320	Silicon for magnesium
Aluminum	$2.1920\ 10^6$	1.1320	Silicon for aluminum
Silicon	$2.1920\ 10^6$	1.1320	Galvin *et al.* [154] and Geiss *et al.* [32]
Sulfur	$2.1920\ 10^6$	1.1320	Silicon for sulfur
Argon	$1.9000\ 10^6$	1.1428	Calcium for argon
Calcium	$1.9000\ 10^6$	1.1428	This work [2)]
Iron	$1.2300\ 10^6$	0.3240	Aellig [150]

[1)] Parameters are interpolated so that the curve (Eq. 8-11) lies between the carbon and the oxygen curve.

[2)] Parameters for calcium are derived using the reported freeze-in temperature of 1.53 MK at $v_{SW} <$ 380 km/s from Kern *et al.* [73] and assuming a freeze-in temperature of 1.1 MK at $v_{SW} \approx 700$ km/s (similar to iron at that velocity).

This simple method of deriving the charge state distributions for the heavy ions in the solar wind worked well for the time periods investigated in this work. A detailed analysis of the various sources of error in the determination of the MTOF instrument function showed that the error introduced by a change in the charge-state distribution within a physical reasonable range is very small compared to the uncertainties encountered in other areas[6]. However, one has to remember that the correlation between the solar wind velocity and the freeze-in temperature is a statistical observation and therefore is only true for most of the solar wind flow (i.e., shows up unambiguously only when evaluating longer data sets). Sometimes there are significant deviations from this average behavior, as has been reported recently by Hefti *et al.* [22]. Thus, for the investigation of short, perhaps unusual, time intervals or events one has to verify, at least for some elements, that the freeze-in temperatures derived from this algorithm (better the charge distributions) are in agreement with measured charge state distributions. This is particularly true for transient events, like CMEs, which show a wide range of charge distributions [58], which in general differ from regular solar wind charge distributions, and thus differ from the predictions given by the algorithm.

8.2.2 The Velocity of Heavy Ions in the Solar Wind

It has been known since the early 1970's that in the solar wind the alpha particles propagate at a different velocity than the protons. Despite the greater mass of the alpha particles they usually move faster than the protons. For details see the review by Neugebauer *et al.* [155] or, for example, the earlier experimental work by Marsch *et al.* [113]. The difference in the alpha particle velocity compared to the proton velocity depends also on the distance from the Sun. When moving the observation point from the near Earth to the Sun, the difference in these velocities usually increases [113]. Going away from the Sun the difference becomes smaller until it disappears totally beyond about 2 AU [155]. There is also a correlation between the Alfvén velocity and the velocity difference, which points at a possible mechanism for the preferential acceleration of heavy particles involving wave-particle interaction [156]. A difference velocity was also observed for the heavy ions. For silicon [35] and for iron [157] it was found that these ions move more slowly than the alpha particles at 1 AU. Recently, the difference velocities between Si and O, and between Fe and O, and between O and protons have been deri-

---

[6] Private communication, John Paquette, University of Maryland, 1999.

Table 8-2: Offset and slope for the determination of the velocity of the heavy ions with respect to the proton velocity for a measurement position at 1 AU. Entries for which no reference is given are interpolated.

Element	Mass [amu]	Offset v_0 [m/s]	Slope k_s	Reference
Helium	4	$-81.0\ 10^3$	1.25	This work [1)]
Carbon	12	$-57.5\ 10^3$	1.17	
Nitrogen	14	$-51.5\ 10^3$	1.15	
Oxygen	16	$-46.0\ 10^3$	1.13	Hefti *et al.* [22; 147]
Neon	20	$-39.0\ 10^3$	1.10	
Sodium	23	$-33.0\ 10^3$	1.075	
Magnesium	24	$-31.0\ 10^3$	1.07	
Aluminum	27	$-26.0\ 10^3$	1.045	
Silicon	28	$-24.0\ 10^3$	1.04	Hefti *et al.* [22; 147]
Sulfur	32	$-22.5\ 10^3$	1.035	
Argon	36	$-21.0\ 10^3$	1.03	
Calcium	40	$-19.0\ 10^3$	1.02	
Iron	56	$-15.0\ 10^3$	1.01	Hefti *et al.* [22; 147]

[1)] Analysis of ICI/ISEE3 data published by Zurbuchen [158].

ved from CELIAS/CTOF measurements by Hefti *et al.* [22]. When the measurements were made in enough detail a linear relationship between the two species was found for which a comparison of their velocities has been made [22; 35; 113; 155; 157]. The published data have been converted to give the heavy ion velocity as a function of the proton velocity, the only ion in the solar wind for which we have continuous measurements available. For the data analysis the heavy ion velocity is calculated from

$$v_i = v_0(i) + k_S(i) v_{SW} \qquad \text{Eq. 8-12}$$

with the values for the offset v_0 and for the slope k_s for the different elements listed in Table 8-2. For oxygen, silicon, and iron the values reported by Hefti *et al.* [22] have been converted to give the relationship to protons for oxygen, silicon, and iron ions. The ISEE/ICI data presented in the thesis work of Zurbuchen [158] have been used to derive offset and slope for the alpha particles at 1 AU. Using these four elements, the offset and slope values for the other elements, for which we have no measurements, have been derived by interpolation. Since we have helium at the low mass side and iron at the high mass side, and two values in between, the mass range we are interested in is covered well. This interpolation assumes that the mass dependence of these values is a monotonic function of the mass. So far there is no report in the literature that this monotonic behavior should not be the case. These data are also shown in Figure 8-2. There is a correlation between the slope and the offset; a larger slope goes together with a large offset. However, at a proton velocity of about 350 km/s all the heavy ions and the protons have approximately the same velocity. Below about 350 km/s the heavy ions are slower than the protons, above that velocity the heavy ions are faster than the protons.

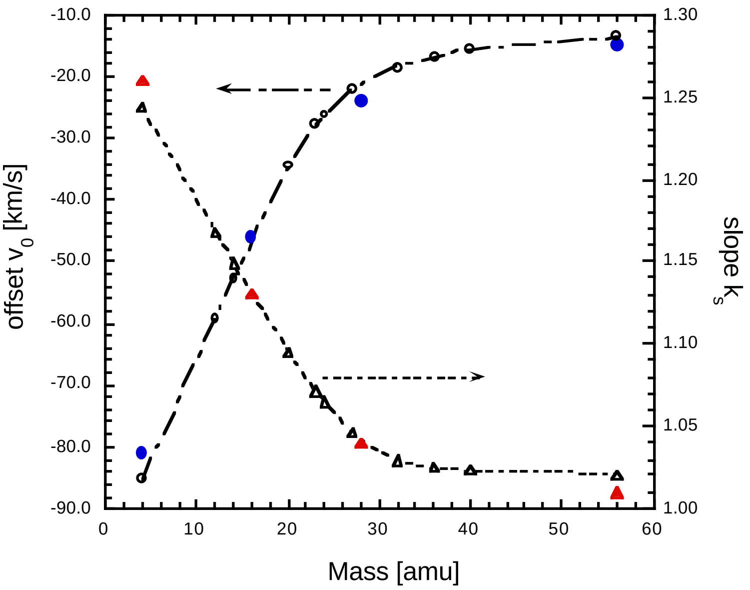

Figure 8-2: Offset and slope for the determination of the velocity of the heavy ions with respect to the proton velocity for a measurement position at 1 AU. Full symbols denote measured data; open symbols denote the interpolations for the remaining elements.

9 Acknowledgements

I am deeply indebted to Professor Peter Bochsler for his continuous support throughout the time I have been at the Physics Institute of the University of Bern, and in particular for the many stimulating discussions I have had in the course of this work.

Robert Sheldon was very helpful during the initial phase in developing the instrument function for MTOF. Reinald Kallenbach provided valuable calibration data for the MTOF entrance system. I also would like to thank Fred M. Ipavich, from the University of Maryland, USA, for his diligent effort in checking the instrument function I developed and for identifying errors in the coding of the instrument function, and also for the fruitful collaboration in the analysis and scientific interpretation of MTOF data. The help of Marty Lee, from the University of New Hampshire, USA, on theoretical matters is also gratefully acknowledged. I further thank Jeannie Wurz and Stefan Scherer for carefully proof-reading the manuscript.

Furthermore, I had many stimulating discussions on this topic with Matthias Aellig, Simon Hefti, Olivier Kern, Rosmarie Neukomm, Reto Schletti, and Robert Wimmer-Schweingruber, all at the University of Bern, which are gratefully acknowledged. Finally, it is a great pleasure for me to acknowledge all my colleagues on the CELIAS team, with whom I had the opportunity to work during the hardware phase and later during the data phase.

This work was supported by the Swiss National Science Foundation.

10 References

[1] E. Anders and N. Grevesse (1989). “Abundances of elements: Meteoritic and solar.” *Geochim. Cosmochim. Acta* **53**: 197–214.

[2] N. Grevesse and A.J. Sauval (1998). “Standard solar composition.” *Space Sci. Rev.* **85**: 161–174.

[3] R. von Steiger (1995). *Solar wind composition and charge states*. Solar Wind Eight, Dana Point, CA, USA, Eds. D. Winterhalter, J.T. Gosling, S.R. Habbal, W.S. Kurth and M. Neugebauer, AIP Press, 193–198.

[4] H.H. Breneman and E.C. Stone (1985). “Solar coronal and photospheric abundances from solar energetic particle measurements.” *Astrophys. Jou.* **299**: L57–L61.

[5] J. Geiss (1982). “Processes affecting the abundance in the solar wind.” *Space Sci. Rev.* **33**: 201–217.

[6] D. Hovestadt, M. Hilchenbach, A. Bürgi, B. Klecker, P. Laeverenz, M. Scholer, H. Grünwaldt, W.I. Axford, S. Livi, E. Marsch, B. Wilken, P. Winterhoff, F.M. Ipavich, P. Bedini, M.A. Coplan, A.B. Galvin, G. Gloeckler, P. Bochsler, H. Balsiger, J. Fischer, J. Geiss, R. Kallenbach, P. Wurz, K.-U. Reiche, F. Gliem, D.L. Judge, K.H. Hsieh, E. Möbius, M.A. Lee, G.G. Managadze, M.I. Verigin, and M. Neugebauer (1995). “CELIAS: The Charge, Element, and Isotope Analysis System for SOHO.” *Solar Physics* **162**: 441–481.

[7] B. Fleck, V. Domingo, and A.I. Poland (1995). *The SOHO Mission*. Dordrecht, The Netherlands, Kluwer Academic Publishers.

[8] J.T. Gosling, G. Borrini, J.R. Asbridge, S.J. Bame, W.C. Feldman, and R.F. Hansen (1981). “Coronal streamers in the solar wind at 1 AU.” *J. Geophys. Res.* **86**: 5438–5448.

[9] J.T. Nolte, A.S. Krieger, A.F. Timothy, R.E. Gold, E.C. Roelof, G. Vaiana, A.J. Lazarus, J.D. Sullivan, and P.S. Mcintosh (1976). “Coronal holes as source of solar wind.” *Solar Physics* **46**: 303–322.

[10] J. Geiss and P. Bochsler (1986). Solar wind composition and what we expect to learn from out-of-ecliptic measurements. In *The Sun and the Heliosphere in Three Dimensions*, Ed. R.G. Marsden, D. Reidel Publishing Company: 173–186.

[11] J.-C. Hénoux (1998). “FIP fractionation: Theory.” *Space Sci. Rev.* **85**: 215–226.

[12] E. Marsch, R. von Steiger, and P. Bochsler (1995). “Element fractionation by diffusion in the solar chromosphere.” *Astron. Astrophys.* **301**: 261–276.

[13] H. Peter (1996). “Velocity dependent fractionation in the solar chromosphere.” *Astron. Astrophys.* **312**: L37–L40.

[14] P. Wurz, M.R. Aellig, F.M. Ipavich, S. Hefti, P. Bochsler, A.B. Galvin, H. Grünwaldt, M. Hilchenbach, F. Gliem, and D. Hovestadt (1999). “The iron, silicon, and oxygen abundance in the solar wind measured with SOHO/CELIAS/MTOF.” *Phys. Chem. Earth*: in press.

[15] F.M. Ipavich, A.B. Galvin, S.E. Lasley, J.A. Paquette, S. Hefti, K.-U. Reiche, M.A. Coplan, G. Gloeckler, P. Bochsler, D. Hovestadt, H. Grünwaldt, M. Hilchenbach, F. Gliem, W.I. Axford, H. Balsiger, A. Bürgi, J. Geiss, K.C. Hsieh, R. Kallenbach, B. Klecker, M.A. Lee, G.G. Managadze, E. Marsch, E. Möbius, M. Neugebauer, M. Scholer, M.I. Verigin, B. Wilken, and P. Wurz (1998). “The solar wind proton monitor on the SOHO spacecraft.” *J. Geophys. Res.* **103**(A8): 17205–17214.

[16] A. Bürgi, M. Oetliker, P. Bochsler, J. Geiss, and M.A. Coplan (1990). “Charge exchange of low-energy ions in thin carbon foils.” *J. Appl. Phys.* **68**(6): 2547–2554.

[17] A. Bürgi, M. Gonin, M. Oetliker, P. Bochsler, J. Geiss, T. Lamy, A. Brenac, H.J. Andrä, P. Roncin, H. Laurent, and M.A. Copland (1993). “Charge exchange of low energy ions in thin carbon foils. II. Results for ions of B, C, F, Ne, Na, Si, S, Cl, Ar, K, and Fe.” *J. Appl. Phys.* **73**(9): 4130–4139.

[18] M. Gonin, R. Kallenbach, P. Bochsler, and A. Bürgi (1995). “Charge exchange of low energy particles passing through thin carbon foils: Dependence on foil thickness and charge state yields of Mg, Ca, Ti, Cr, and Ni.” *Nucl. Instr. Meth.* **B 101**: 313–320.

[19] M. Gonin (1995). *Ein semiempirisches Modell des Ladungsaustausches von niederenergetischen Ionen beim Durchgang durch dünne Folien, zur Eichung von isochronen Flugzeit-Massenspektrometern*, PhD Thesis, University of Bern.

[20] M.R. Aellig, S. Hefti, H. Grünwaldt, P. Bochsler, P. Wurz, F.M. Ipavich, and D. Hovestadt (1998). “The Fe/O elemental abundance in the solar wind.” *J. Geophys. Res.*: in press.

[21] P. Bochsler (1997). “Particles in the solar wind.” *ESA* **SP-404**: 113–122.

[22] S. Hefti, H. Grünwaldt, F.M. Ipavich, P. Bochsler, D. Hovestadt, M.R. Aellig, M. Hilchenbach, R. Kallenbach, A.B. Galvin, J. Geiss, F. Gliem, G. Gloeckler, B. Klecker, E. Marsch, E. Möbius, M. Neugebauer, and P. Wurz (1998). “Kinetic properties of solar wind minor ions and protons measured with SOHO/CELIAS.” *J. Geophys. Res.* **103**(A12): 29697–29704.

[23] M. Arnaud and R. Rothenflug (1985). “An updated evaluation of recombination and ionization rates.” *Astron. Astrophys. Suppl. Ser.* **60**: 425–457.

[24] M. Arnaud and J. Raymond (1992). “Iron ionization and recombination rates and ionization equilibrium.” *Astrophys. Jou.* **398**: 394–406.

[25] M. Neugebauer (1981). Observations of solar wind helium. In *Fundamentals of Cosmic Physics,* Gordon and Breach Science Publishers, Inc. **7:** 131–199.

[26] J. Geiss, G. Gloeckler, and R. von Steiger (1995). “Origin of the solar wind from compositional data.” *Space Sci. Rev.* **72**: 49–60.

[27] J. Schmid, P. Bochsler, and J. Geiss (1988). “Abundance of iron ions in the solar wind.” *Astrophys. Jou.* **329**: 956–966.

[28] P. Bochsler, J. Geiss, and R. Joos (1986). “Abundances of carbon, oxygen, and neon in the solar wind during the period from August 1978 to June 1982.” *Solar Physics* **102**: 177–201.

[29] M.R. Aellig, H. Holweger, P. Bochsler, P. Wurz, H. Grünwaldt, S. Hefti, F.M. Ipavich, and B. Klecker (1998). *The Fe/O elemental abundance ratio in the solar wind*. Solar Wind 9, Nantucket, MA, USA, submitted.

[30] F.M. Ipavich, A.B. Galvin, J. Geiss, K.W. Ogilvie, and F. Gliem (1991). *Solar wind iron and oxygen charge states and relative abundances measured by SWICS on Ulysses*. Solar Wind Seven, Eds. E. Marsch and R. Schwenn, Pergamon Press, 369–373.

[31] G. Gloeckler, F.M. Ipavich, D.C. Hamilton, B. Wilken, W. Stüdemann, G. Kremser, and D. Hovestadt (1989). “Heavy ion abundances in coronal hole solar wind flows (abstract).” *Eos Trans. AGU* **70**: 424.

[32] J. Geiss, G. Gloeckler, R. von Steiger, H. Balsiger, L.A. Fisk, A.B. Galvin, F.M. Ipavich, S. Livi, J.F. McKenzie, K.W. Ogilvie, and B. Wilken (1995). “The southern high-speed stream: Results from the SWICS instrument on Ulysses.” *Science* **268**: 1033–1036.

[33] F.M. Ipavich, A.B. Galvin, G. Gloeckler, D. Hovestadt, S.J. Bame, B. Klecker, M. Scholer, L.A. Fisk, and C.Y. Fan (1986). “Solar wind Fe and CNO measurements in high-speed flows.” *J. Geophys. Res.* **91**(A4): 4133–4141.

[34] P. Hannaford, R.M. Lowe, N. Grevesse, and A. Noels (1992). “Lifetimes in FeII and the solar abundance of iron.” *Astron. Astrophys.* **259**: 301–306.

[35] P. Bochsler (1989). “Velocity and abundance of silicon ions in the solar wind.” *J. Geophys. Res.* **94**(A3): 2365–2373.

[36] A.B. Galvin, G. Gloeckler, F.M. Ipavich, C.M. Shafer, J. Geiss, and K. Ogilvie (1993). “Solar wind composition measurements by the Ulysses SWICS experiment during transient solar wind flows.” *Adv. Space Res.* **13**(6): 75–78.

[37] J.C. Raymond, J.L. Kohl, G. Noci, E. Antonucci, G. Tondello, M.C.E. Huber, L.D. Gardner, P. Nicolosi, S. Fineschi, M. Romoli, D. Sparado, O.H.W. Siegmund, C. Benna, A. Ciaravella, S. Cranmer, S. Giordano, M. Karvoska, R. Martin, J. Michels, A. Modigliani, G. Naletto, A. Panasyuk, C. Pernechele, G. Poletto, P.L. Smith, R.M. Suleiman, and L. Strachnan (1997). “Composition of coronal streamers from the SOHO ultraviolet coronagraph spectrometer.” *Solar Physics* **175**: 645–665.

[38] J.C. Raymond, R. Suleiman, J.L. Kohl, and G. Noci (1998). “Elemental abundances in coronal structures.” *Space Sci. Rev.* **85**: 283–289.

[39] P. Wurz, F.M. Ipavich, A.B. Galvin, P. Bochsler, M.R. Aellig, R. Kallenbach, D. Hovestadt, H. Grünwaldt, M. Hilchenbach, W.I. Axford, H. Balsiger, A. Bürgi, M.A. Coplan, J. Geiss, F. Gliem, G. Gloeckler, S. Hefti, H.C. Hsieh, B. Klecker,

M.A. Lee, G.G. Managadze, E. Marsch, E. Möbius, M. Neugebauer, K.-U. Reiche, M. Scholer, M.I. Verigin, and B. Wilken (1998). "Elemental composition of the January 6, 1997, CME." *Geophys. Res. Lett.* **25**(14): 2557–2560.

[40] M. Oetliker, D. Hovestadt, B. Klecker, M.R. Collier, G. Gloeckler, D.C. Hamilton, F.M. Ipavich, P. Bochsler, and G.G. Managadze (1997). "The isotopic composition of iron in the solar wind: First measurements with the MASS sensor on the WIND spacecraft." *Astrophys. Jou.* **474**: L69–L72.

[41] F.M. Ipavich, P. Bochsler, R. Kallenbach, P. Wurz, H. Grünwaldt, M. Hilchenbach, and D. Hovestadt (1998). "Iron isotopes in the solar wind: Measurements from SOHO/CELIAS/MTOF." *Eos Trans. AGU* **79**(17): S274.

[42] G. Audi and A.H. Wapsta (1995). "The 1995 update to the atomic mass evaluation." *Nuclear Physics* **A595**(4): 409–480.

[43] R.F. Wimmer-Schweingruber, P. Bochsler, G. Gloeckler, F.M. Ipavich, J. Geiss, R. Kallenbach, L.A. Fisk, S. Hefti, and T. Zurbuchen (1999). "On the bulk isotopic composition of magnesium and silicon during the May 1998 CME: ACE/SWIMS." *Geophys. Res. Lett.* **26**(2): 165–168.

[44] J. Geiss, F. Bühler, H. Cerutti, P. Eberhardt, and C. Filleux (1972). "Solar wind composition experiment." *Apollo 16 Prelim. Sci. Rep.* **NASA-SP-315**: 14.1–14.10.

[45] R. Kallenbach, F.M. Ipavich, P. Bochsler, S. Hefti, D. Hovestadt, H. Grünwaldt, M. Hilchenbach, W.I. Axford, H. Balsiger, A. Bürgi, M.A. Coplan, A.B. Galvin, J. Geiss, F. Gliem, G. Gloeckler, K.C. Hsieh, B. Klecker, M.A. Lee, S. Livi, G.G. Managadze, E. Marsch, E. Möbius, M. Neugebauer, K.U. Reiche, M. Scholer, M.I. Verigin, B. Wilken, and P. Wurz (1997). "Isotopic composition of solar wind neon measured by CELIAS/MTOF onboard SOHO." *J. Geophys. Res.* **102**(A12): 26895–26904.

[46] R.F. Wimmer-Schweingruber, P. Bochsler, and P. Wurz (1999). *Isotopes in the solar wind: New results from ACE, SOHO, and WIND.* Solar Wind 9, Nantucket, MA, USA, submitted.

[47] P. Wurz, F.M. Ipavich, A.B. Galvin, P. Bochsler, M.R. Aellig, R. Kallenbach, D. Hovestadt, H. Grünwaldt, M. Hilchenbach, W.I. Axford, H. Balsiger, A. Bürgi, M.A. Coplan, J. Geiss, F. Gliem, G. Gloeckler, S. Hefti, H.C. Hsieh, B. Klecker, M.A. Lee, S. Livi, G.G. Managadze, E. Marsch, E. Möbius, M. Neugebauer, K.-U. Reiche, M. Scholer, M.I. Verigin, and B. Wilken (1997). "Elemental composition before, during, and after the January 6, 1997, CME event measured by CELIAS/SOHO." *ESA* **SP-415**: 395–400.

[48] N.J. Fox, M. Peredo, and B.J. Thompson (1998). "Cradle to grave tracking of the January 6–11, 1997 Sun-Earth connection event." *Geophys. Res. Lett.* **25**(14): 2461–2464.

[49] J.T. Gosling (1997). Coronal mass ejections: An overview. In *Coronal Mass Ejections,* Eds. N. Crooker, J.A. Joselyn and J. Feynman, American Geophysical Union. *Geophysical Monograph* **99:** 9–16.

[50] L. Burlaga, R. Fritzenreiter, R. Lepping, K. Ogilvie, A. Szabo, A. Lazarus, J. Steinberg, G. Gloeckler, R. Howard, D. Michels, C. Farrugia, R.P. Lin, and D.E. Larson (1998). "A magnetic cloud containing prominence material: January 1997." *J. Geophys. Res.* **103**: 277–286.

[51] J.T. Gosling (1990). Coronal mass ejections and magnetic flux ropes in interplanetary space. In *Physics of Magnetic Flux Ropes*, Eds. C.T. Russel, E.R. Priest and L.C. Lee, AGU Geophys. Monograph. **58:** 343–364.

[52] L.F. Burlaga (1974). "Interplanetary stream interfaces." *J. Geophys. Res.* **86**: 3717–3725.

[53] R. von Steiger, R.F. Wimmer-Schweingruber, J. Geiss, and G. Gloeckler (1995). "Abundance variations in the solar wind." *Adv. Space Res.* **15**(7): 3–12.

[54] U. Feldman (1992). "Elemental abundances in the upper solar atmosphere." *Physica Scripta* **46**: 202–220.

[55] J.P. Meyer (1993). Element fractionation at work in the solar atmosphere. In *Origin and Evolution of the Elements*, Eds. N. Prantzos, E. Vangioni-Flam and M. Cassè, Oxford, Cambridge Univ. Press: 26–62.

[56] D.V. Reames (1992). "Energetic particle observations and the abundance of elements in the solar corona." *ESA* **SP-348**: 315–323.

[57] C.M. Shafer, G. Gloeckler, A.B. Galvin, F.M. Ipavich, J. Geiss, R. von Steiger, and K. Ogilvie (1993). “Sulfur abundances in the solar wind measured by SWICS on ULYSSES.” *Adv. Space Res.* **13**(6): 79–82.

[58] A.B. Galvin (1997). Minor ion composition in CME-related solar wind. In *Coronal Mass Ejections*, Eds. N. Crooker, J.A. Joselyn and J. Feynman, American Geophysical Union. *Geophysical Monograph* **99**.

[59] A.J. Hundhausen (1997). A summary of SMM observations from 1980 and 1984–1989. In *The many Faces of the Sun*, Eds. K. Strong, J. Saba and B. Haisch, New York, Springer Verlag: in press.

[60] J.-P. Meyer (1985). “The baseline composition of solar energetic particles.” *Astrophys. Jou. Suppl. Ser.* **57**: 151–171.

[61] D.F. Webb, E.W. Cliver, N. Gopalswamy, H.S. Hudson, and O.C. St.Cyr (1998). “The solar origin of the January 1997 coronal mass ejection, magnetic cloud and geomagnetic storm.” *Geophys. Res. Lett.* **25**(14): 2469–2472.

[62] H.S. Hudson, J.R. Lemen, O.C. St.Cyr, A.C. Sterling, and D.F. Webb (1998). “X-ray coronal changes during hale CMEs.” *Geophys. Res. Lett.* **25**(14): 2481–2484.

[63] H.V. Cane, I.G. Richardson, and O.C. St.Cyr (1998). “The interplanetary events of January–May, 1997 as inferred from energetic particle data, and their relationship with solar events.” *Geophys. Res. Lett.* **25**(14): 2517–2520.

[64] J. Torsti, A. Anttila, L. Kocharov, P. Mäkelä, E. Riihonen, T. Sahla, M. Teittine, E. Valtonen, T. Laitinen, and R. Vainio (1998). “Energetic (~1 to 50 MeV) protons associated with Earth-directed coronal mass ejections.” *Geophys. Res. Lett.* **25**(14): 2525–2528.

[65] Z. Mikic and J.A. Linker (1997). The initiation of coronal mass ejections by magnetic shear. In *Coronal Mass Ejections*, Eds. N. Crooker, J.A. Joselyn and J. Feynman, American Geophysical Union. *Geophysical Monograph* **99:** 57–64.

[66] J. Chen (1997). Coronal Mass ejections: Causes and Consequences a theoretical view. In *Coronal Mass Ejections*, Eds. N. Crooker, J.A. Joselyn and J. Feynman, American Geophysical Union. *Geophysical Monograph* **99:** 65–81.

[67] F.F. Chen (1984). *Introduction to Plasma Physics and Controlled Fusion*. New York, Plenum Press.

[68] R.J. Bray, L.E. Cram, C.J. Durrant, and C.J. Loughhead (1991). *Plasma loops in the solar corona*. Cambridge, Cambridge University Press.

[69] J.L. Kohl, E. Antonucci, G. Tondello, M.C.E. Huber, S.R. Cranmer, L. Strachnan, A.V. Panasyuk, L.D. Gardner, M. Romoli, S. Fineschi, D. Dobrzycka, J.C. Raymond, P. Nicolosi, O.H.W. Siegmund, D. Spadaro, C. Benna, A. Ciaravella, S. Giordano, S.R. Habbal, M. Karovska, X. Li, R. Martin, J.G. Michels, A. Modigliani, G. Naletto, R.H. O'Neal, C. Pernechele, G. Poletto, P.L. Smith, and R.M. Suleiman (1998). “UVCS/SOHO empirical determinations of anisotropic velocity distributions in the solar corona.” *Astrophys. Jou.* **501**: L127–L131.

[70] S.R. Cranmer, G.B. Field, and J.L. Kohl (1999). *The impact of ion-cyclotron wave dissipation on heating and accelerating the fast solar wind*. Solar Wind 9, Nantucket, MA, USA, in press.

[71] J.D. Jackson (1983). *Klassische Elektrodynamik*, Walter de Gruyter, Berlin, New York.

[72] M.R. Aellig, P. Bochsler, H. Grünwaldt, S. Hefti, P. Wurz, M. Hilchenbach, D. Hovestadt, F.M. Ipavich, and F. Gliem (1999). “The influence of surprathermal electrons on the derivation of coronal electron temperatures from solar wind minor ion charge states.” *Phys. Chem. Earth*: in press.

[73] O. Kern, R.F. Wimmer-Schweingruber, P. Bochsler, G. Gloeckler, and D.C. Hamilton (1997). “Determination of calcium and silicon charge states and elemental abundances in the solar wind with the MASS instrument on WIND.” *ESA* **SP-415**: 345–348.

[74] J.P. Meyer (1993). “Elemental abundances in active regions, flares and interplanetary medium.” *Adv. Space Res.* **13**(9): 377–390.

[75] J.E. Ross and J.H. Aller (1976). “The chemical composition of the sun.” *Science* **191**: 1223–1229.

[76] D.L. Lambert and R.E. Luck (1978). “The abundance of the elements in the solar photospheres - IX: Na to Ca.” *Mon. Not. R. astr. Soc.* **183**: 79–100.

[77] N. Grevesse and E. Anders (1991). *Solar element abundances*. Solar Interior and Atmosphere, Tucson, Eds. A.N. Cox, W.C. Livingston and M.S. Matthews, Univ. of Arizona Press, 1227–1234.

[78] N.J. Veck and J.H. Parkinson (1981). “Solar abundances from X-ray flare observations.” *Mon. Not. R. astr. Soc.* **197**: 41–55.

[79] J.R. Lemen, J. Sylwester, and R.D. Bentley (1986). “Determination of the calcium elemental abundance for 43 flares from SMM-XRP solar X-ray spectra.” *Adv. Space Res.* **6**: 245–248.

[80] K.J.H. Phillips and U. Feldman (1991). “The iron-to-calcium abundance ratio in the $20x10^6$ K plasma of medium and large solar flares.” *Astrophys. Jou.* **379**: 401–405.

[81] A.C. Sterling, G.A. Doschek, and U. Feldman (1993). “On the absolute abundance of calcium in solar flares.” *Astrophys. Jou.* **404**: 394–402.

[82] A. Fludra, J.L. Culhane, R.D. Bentley, G.A. Doschek, E. Hiei, K.J.H. Phillips, A. Sterling, and T. Watanabe (1993). “Determination of coronal abundances of sulfur, calcium, and iron using the YOHKOH Bragg crystal spectrometer.” *Adv. Space Res.* **13**(9): 395–398.

[83] D.V. Reames (1994). “Coronal element abundances derived from solar energetic particles.” *Adv. Space Res.* **14**(4): 177–180.

[84] D.V. Reames (1998). “Solar energetic particle: Sampling coronal abundances.” *Space Sci. Rev.* **85**: 327–340.

[85] S.J. Bame, J.R. Asbridge, W.C. Feldman, M.D. Montgomery, and P.D. Kearney (1975). “Solar wind heavy ion abundances.” *Solar Physics* **43**: 463–473.

[86] U. Feldman, K.G. Widing, and P.A. Lund (1990). “On the anomalous abundances of the $2x10^4$–$2x10^5$ K solar atmosphere above a sunspot.” *Astrophys. Jou.* **364**: L21–L23.

[87] J.-P. Meyer (1985). “Solar-stellar outer atmospheres and energetic particles, and galactic cosmic rays.” *Astrophys. Jou. Suppl. Ser.* **57**: 173–204.

[88] D.A. Falconer, J.M. Davila, and R.J. Thomas (1997). “Relative elemental abundances of the quiet solar corona as determined by SERTS.” *Astrophys. Jou.* **482**: 1050–1064.

[89] G. Gloeckler and K.C. Hsieh (1979). “Time-of-Flight technique for particle identification at energies from 2 – 400 keV/nucleon.” *Nucl. Instr. Meth.* **165**: 537–544.

[90] G. Gloeckler, F.M. Ipavich, W. Studemann, B. Wilken, D.C. Hamilton, G. Kremser, D. Hovestadt, F. Gliem, R.A. Lundgren, W. Rieck, E.O. Tums, J.C. Cain, L.S. Masung, W. Weiss, and P. Winterhof (1985). “The charge-energy-mass spectrometer for 0.3–300 keV/e ions on the AMPTE CCE.” *IEEE Trans. Geosci. Rem. Sens.* **GE-23**(3): 234–240.

[91] E. Möbius, G. Gloeckler, D. Hovestadt, F.M. Ipavich, B. Klecker, M. Scholer, H. Arbinger, H. Höfner, E. Künneth, P. Laeverenz, A. Luhn, E.O. Tums, and H. Waldleben (1985). “The time-of-flight spectrometer SULEICA for ions of the energy range 5–270 keV/charge on AMPTE IRM.” *IEEE Trans. Geosci. Remote Sens.* **GE-23**(3): 274–279.

[92] D. Hovestadt, J. Geiss, G. Gloeckler, E. Möbius, P. Bochsler, F. Gliem, F.M. Ipavich, B. Wilken, W.I. Axford, H. Balsiger, A. Bürgi, M. Coplan, H. Dinse, A.B. Galvin, K.I. Gringauz, H. Grünwaldt, K.C. Hsieh, B. Klecker, M.A. Lee, G.G. Managadze, E. Marsch, M. Neugebauer, W. Rieck, M. Scholer, and W. Stüdemann (1989). *ESA* **SP-1104**: 69–74.

[93] G. Gloeckler, J. Geiss, H. Balsiger, P. Bedini, J.C. Cain, J. Fischer, L.A. Fisk, A.B. Galvin, F. Gliem, D.C. Hamilton, J.V. Hollweg, F.M. Ipavich, R. Joos, S. Livi, R. Lundgren, J.F. McKenzie, U. Mall, K.W. Ogilvie, F. Ottens, W. Rieck, E.O. Tums, R. von Steiger, W. Weiss, and B. Wilken (1992). “The solar wind ion composition spectrometer.” *Astron. Astrophys. Suppl. Ser.* **92**: 267–289.

[94] M. Gonin, R. Kallenbach, and P. Bochsler (1994). “Charge exchange of atoms with high first ionization potential in carbon foils at $E \leq 35$ keV/u.” *Nucl. Instr. Meth.* **B 94**: 15–21.

[95] Y. Yoshida (1986). “Time-of-flight mass spectrometer.” *US Patent* **4,625,112**.

[96] D.J. McComas, J.E. Nordholt, S.J. Bame, B.L. Barraclough, and J.T. Gosling (1990). “Linear electric field mass analysis: A technique for three-dimensional high mass resolution space plasma composition measurements.” *Proc. Natl. Acad. Sci. USA* **87**: 5925–5929.

[97] D.J. McComas and J.E. Nordholt (1990). “New approach to 3-D, high sensitivity, high mass resolution space plasma composition measurements.” *Rev. Sci. Instr.* **61**(10): 3095–3097.

[98] D.C. Hamilton, G. Gloeckler, F.M. Ipavich, R.A. Lundgren, R.B. Sheldon, and D. Hovestadt (1990). “New high resolution electrostatic ion mass analyzer using time of flight.” *Rev. Sci. Instr.* **61**(10): 3104–3106.

[99] G. Gloeckler, H. Balsiger, A. Bürgi, P. Bochsler, L.A. Fisk, A.B. Galvin, J. Geiss, F. Gliem, D.C. Hamilton, T.E. Holzer, D. Hovestadt, F.M. Ipavich, E. Kirsch, R.A. Lundgren, K.W. Ogilvie, R.B. Sheldon, and B. Wilken (1995). The solar wind and suprathermal ion composition investigation on the WIND spacecraft. In *The Global Geospace Mission*, Ed. C.T. Russel, Kluwer Academic Publisher: 79–124.

[100] G. Gloeckler, J. Cain, F.M. Ipavich, E.O. Tums, P. Bedini, L.A. Fisk, T.H. Zurbuchen, P. Bochsler, J. Fischer, R. Wimmer-Schweingruber, J. Geiss, and R. Kallenbach (1998). “Investigation of the composition of solar and interstellar matter using solar wind and pickup ion measurements with SWICS and SWIMS on the ACE spacecraft.” *Space Sci. Rev.*: in press.

[101] E. Möbius, P. Bochsler, A.G. Ghielmetti, and D.C. Hamilton (1990). “High mass resolution isochronous time-of-flight spectrograph for three-dimensional space plasma measurements.” *Rev. Sci. Instr.* **61**(11): 3609–3612.

[102] L. Gubler, P. Wurz, P. Bochsler, and E. Möbius (1995). “High resolution isochronous mass spectrometer for space plasma applications.” *Int. J. Mass Spectr.* **148**: 77–96.

[103] P. Wurz, L. Gubler, P. Bochsler, and E. Möbius (1998). “Isochronous mass spectrometer for space plasma applications.” *AGU Monograph* **102**: 229–235.

[104] J.P. Carrico (1976). Time-of-Flight Spectrometers. In *Quadrupole Mass Spectrometry*, Ed. P.H. Dawson, Amsterdam, Elsevier Scientific Publishing Company: 225–240.

[105] A. Bürgi (1991). “Ion composition measurements.” *Adv. Space Res.* **11**: 391–400.

[106] P. Beiersdorfer, A.L. Roquemore, and R. Kaita (1987). “Characteristics of compact solid-target charge exchange analyzers for energetic ion diagnostics on tokamaks.” *Rev. Sci. Instr.* **58**(11): 2092–2098.

[107] P.M. Echenique, R.M. Niemienen, J.C. Ashley, and R.H. Ritchie (1986). “Nonlinear stopping power of an electron gas for slow ions.” *Phys. Rev. A* **33**(2): 897–504.

[108] A.A.E. van Blokland, T.W.M. Grimbergen, and H.W. van der Ven (1992). “A mass-selective neutral particle analyzer with background rejection.” *Rev. Sci. Instr.* **63**(3): 1978–1987.

[109] A.G. Ghielmetti, H. Balsiger, R. Bänninger, P. Eberhardt, J. Geiss, and D.T. Young (1983). “Calibration system for satellite and rocket-borne ion mass spectrometers in the energy range from 5eV/charge to 100keV/charge.” *Rev. Sci. Instr.* **54**(4): 425–436.

[110] M. Steinacher, F. Jost, and U. Schwab (1995). “A modern and fully automated calibration system for space ion mass spectrometers.” *Rev. Sci. Instr.* **66**(8): 4180–4187.

[111] R. von Steiger, J. Geiss, G. Gloeckler, and A.B. Galvin (1995). “Kinetic properties of heavy ions in the solar wind from SWICS/ULYSSES.” *Space Science Rev.* **72**: 71–76.

[112] E. Marsch, K.H. Mühlhauser, R. Schwenn, H. Rosenbauer, W. Pilipp, and F.M. Neubauer (1982). “Solar wind protons: Three-dimensional velocity distributions and derived plasma parameters measured between 0.3 and 1 AU.” *J. Geophys. Res.* **87**(A1): 52–72.

[113] E. Marsch, K.-H. Mühlhauser, H. Rosenbauer, R. Schwenn, and F.M. Neubauer (1982). “Solar wind helium ions: Observations of the HELIOS solar probes between 0.3 and 1 AU.” *J. Geophys. Res.* **87**(A1): 35–51.

[114] M. Oetliker (1989). *Charge state distribution, scattering, and residual energy of ions after passing through thin carbon foils*, Master's Thesis, University of Bern, Switzerland.

[115] W. Bernstein, A.J. Cole, and R.L. Wax (1970). “Penetration of 1–20keV ions through thin carbon foils.” *Nucl. Instr. Meth.* **90**: 325–328.

[116] G. Högberg, H. Nordén, and H.G. Berry (1970). “Angular distribution of ions scattered in thin carbon foils.” *Nucl. Instr. Meth.* **90**: 283–288.

[117] J.F. Ziegler, J.P. Biersack, and U. Littmark (1992). *The stopping and range of ions in solids*, Pergamon Press.

[118] L. Meyer (1971). “Plural and multiple scattering of low-energy heavy particles in solids.” *Phys. Stat. Sol. B* **44**: 253–268.

[119] R. Herrmann, C.L. Cocke, J. Ullrich, S. Hagmann, M. Stoeckli, and H. Schmidt-Boecking (1994). “Charge state equilibration length of a highly charged ion inside a Carbon foil.” *Phys. Rev.* **A50**: 1435–1444.

[120] G. Beauchemin and R. Drouin, Eds. (1975). *Collisional and radiative processes*. Beam-Foil Spectroscopy. New York and London, Plenum Press.

[121] T. Schenkel, M.A. Briere, A.V. Barnes, A.V. Hamza, K. Bethge, H. Schmidth-Böcking, and D.H. Schneider (1997). "Charge state dependent energy loss of slow heavy ions in solids." *Phys. Rev. Lett.* **79**(11): 2030–2033.

[122] P. Hvelplund and B. Fastrup (1968). "Stopping cross section in carbon of 0.2–1.5MeV atoms with 21≤Z1≤39." *Phys. Rev.* **165**: 408–414.

[123] S. Mikheev, Y. Ryzhov, I. Shkarban, and V. Yurasova (1993). "Inelastic losses of low-energy ions transmitted through thin films." *Nucl. Instr. Meth.* **B78**: 86–90.

[124] P. Hvelplund, E. Lægsgård, J.Ø. Olsen, and E.H. Pedersen (1970). "Equilibrium charge distributions of ion beams in carbon." *Nucl. Instr. Meth.* **90**: 315–320.

[125] P.L. Smith and W. Whaling (1969). "Equilibrium charge distributions of C, N, Ar, and Fe in Carbon." *Phys. Rev.* **188**: 36–40.

[126] S.H. Overbury, P.F. Dittner, S. Datz, and R.S. Thoe (1979). "Energy loss, angular distributions and charge fractions of low energy hydrogen transmitted through thin carbon foils." *Rad. Eff.* **41**: 219–227.

[127] H. Rothard, K. Kroneberger, A. Clouvas, E. Veje, P. Lorenzen, N. Keller, J. Kemmler, W. Meckbach, and K.-O. Groeneveld (1990). "Secondary-electron yields from thin foils: A possible probe for the electronic stopping power of heavy ions." *Phys. Rev. A* **41**(5): 2521–2535.

[128] J. Schou (1988). "Secondary electron emission from solids by electron and proton bombardment." *Scanning Microscopy* **2**(2): 607–632.

[129] W. Meckbach, G. Braunstein, and N. Arista (1975). "Secondary-electron emission in the backward and forward directions from thin carbon foils traversed by 25–250 keV proton beams." *J. Phys. B: Atom. Molec. Phys.* **8**(14): L344–L349.

[130] H. Rothard, J. Schou, and K.-O. Groenveld (1992). "Projectile- and charge-state-dependent electron yields from ion penetration of solids as a probe of preequilibrium stopping power." *Phys. Rev. A* **43**(3): 1701–1710.

[131] R.A. Baragiola, E.V. Alonso, J. Ferron, and A. Oliva-Florio (1979). "Ion-induced electron emission from clean metals." *Surf. Sci.* **90**: 240–255.

[132] J. Cazeaux (1993). Some physical descriptions of the charging effects in insulators under irradiation. In *Ionization of Solids by Heavy Particles*, Ed. R.A. Baragiola, New York, Plenum Press: 325–350.

[133] H. Rothard, M. Jung, B. Gervais, J.P. Grandin, A. Billebaud, and R. Wünsch (1996). "Fluence dependent electron emission as a measure of surface modification induced by swift heavy ions." *Nucl. Instr. Meth.* **B 107**: 108–112.

[134] A. Clouvas, C. Potiriadis, H. Rothard, D. Hofmann, R. Wünsch, K.O. Groeneveld, A. Katsanos, and A.C. Xenoulis (1997). "Role of projectile electrons in secondary electron emission from solid surfcaces under fast-ion bombardment." *Phys. Rev. B* **55**(18): 12086–12098.

[135] H. Rothard, C. Caraby, A. Cassimi, B. Gervais, J.-P. Grandin, P. Jardin, M. Jung, A. Billebaud, M. Chevallier, K.-O. Groeneveld, and R. Maier (1995). "Target-thickness-dependent electron emission from carbon foils bombardment with swift highly charged heavy ions." *Phys. Rev. A* **51**(4): 3066–3078.

[136] M. Jung, H. Rothard, B. Gervais, J.-P. Grandin, A. Clouvas, and R. Wünsch (1996). "Transport of electrons induced by highly charged Ni (74 MeV/u) and Cu (9.6 MeV/u) ions in carbon: A study of target-thickness-dependent electron yields." *Phys. Rev. A* **54**(5): 4153–4161.

[137] G. Betz and K. Wien (1994). "Energy and angular distributions of sputtered particles." *Int. J. Mass Spectr.* **140**: 1–110.

[138] F. Bordoni (1971). "Channel electron multiplier efficiency for 10–1000eV electrons." *Nucl. Instr. Meth.* **97**: 405–408.

[139] J.G. Timothy and R.L. Bybee (1978). "Performance characteristics of high-conductivity channel electron multipliers." *Rev. Sci. Instr.* **49**: 1192–1196.

[140] J.Ø. Olsen (1979). "Measurement of channel electron multiplier efficiency using a photoemission electron source." *J. Phys. E: Sci. Instrum.* **12**: 1106–1108.

[141] G.W. Fraser (1983). "The electron detection efficiency of microchannel plates." *Nucl. Instr. Meth.* **206**: 445–449.

[142] R.S. Gao, P.S. Gibner, J.H. Newman, K.A. Smith, and R.F. Stebbings (1984). "Absolute and angular efficiencies of a microchannel-plate position-sensitive detector." *Rev. Sci. Instr.* **55**: 1756–1759.

[143] J. Oberheide, P. Wilhelms, and M. Zimmer (1997). "New results on the absolute ion detection efficiencies of a microchannel plate." *Meas. Sci. Technol.* **8**: 351–354.

[144] C.N. Burrous, A.J. Lieber, and V. Zaviantseff (1967). "Detection efficiency of a continuous channel electron multiplier for positive ions." *Rev. Sci. Instr.* **38**: 1477–1481.

[145] A. Marti (1997). *Entwicklung und Aufbau einer Elektron-Zyklotron-Resonanz Ionenquelle*, PhD Thesis, University of Bern, Switzerland.

[146] P. Wurz, A. Marti, and P. Bochsler (1998). "New test facility for solar wind instrumentation." *Helv. Phys. Acta* **71,** *Separada* **1**: 23–24.

[147] S. Hefti (1997). *Solar wind freeze-in temperatures and fluxes measured with SOHO/CELIAS/CTOF and calibration of the CELIAS sensors*, PhD Thesis, University of Bern, Switzerland.

[148] M. Schlapp (1995). *Entwicklung einer 14 GHz und einer "vollpermanenten" 10 GHz Elektron-Zyklotron-Resonanz (EZR) Ionenquelle zur Erzeugung hochgeladener Ionen*, PhD Thesis, Universität Gießen, Germany.

[149] R. Trassl, P. Hathiramani, F. Broetz, J.B. Greenwood, R.W. McCullough, M. Schlapp, and E. Salzborn (1997). "Characterization and recent modification of a compact 10 GHz Electron Cyclotron Resonance (ECR) ion source for atomic physics experiments." *Physica Scripta* **T73**: 380–381.

[150] M.R. Aellig (1998). *Freeze-in temperatures and relative abundances of iron ions in the solar wind measured with SOHO/CELIAS/CTOF*, PhD Thesis, University of Bern, Switzerland.

[151] P. Wurz, Ed. (1997). *The Dataphase Manual for the Charge, Element, and Isotope Analysis System (CELIAS) on the Solar and Heliospheric Observatory (SOHO) Mission*, University of Bern, Switzerland.

[152] P.R. Bevington (1969). *Data Reduction and Error Analysis for the Physical Sciences*. New York, McGraw-Hill.

[153] R. von Steiger (1994). *Composition of the Solar Wind*, Habilitation, University of Bern.

[154] A.B. Galvin, F.M. Ipavich, G. Gloeckler, R. von Steiger, and B. Wilken (1991). *Silicon and oxygen charge state distributions and relative abundances in the solar wind measured by SWICS on ULYSSES*. Solar Wind Seven, Eds. E. Marsch and R. Schwenn, Pergamon Press, 337–340.

[155] M. Neugebauer, B.E. Goldstein, S.J. Bame, and W.C. Feldman (1994). "Ulysses near-ecliptic observations of differential flow between protons and alphas in the solar wind." *J. Geophys. Res.* **99**(A2): 2505–2511.

[156] P.A. Eisenberg and J.V. Hollweg (1983). "On the preferential acceleration and heating of solar wind heavy ions." *J. Geophys. Res.* **88**(A5): 3923–3935.

[157] J. Schmid, P. Bochsler, and J. Geiss (1987). "Velocity of iron ions in the solar wind." *J. Geophys. Res.* **92**(A9): 9901–9906.

[158] T. Zurbuchen (1996). *Turbulence in the interplanetary medium and its implications on the dynamics of minor ions*, PhD Thesis, University of Bern, Switzerland.